FINAL TECHNICAL REPORT

CONTRACT N° : FIKW-CT-2000-00049

PROJECT N° : FIS5-1999-00199

ACRONYM : PYROREP

TITLE : Pyrometallurgical Processing Research Programme "PYROREP"

PROJECT CO-ORDINATOR : H. Boussier

PARTNERS :

AEA-T	Atomic Energy Authority – Technology
BNFL	British Nuclear Fuel Limited
CEA	Commissariat à l'Énergie Atomique
CIEMAT	Centro de Investigaciones Energéticas, Medioambientales y Tecnologicas
CRIEPI	Central Institute of Electric Power Industry
ENEA	Ente per le Nuove Tecnologie, l'Energia e l'Ambiente
ITU	Institute for Transuranium Elements – Joint Research Centre
NRI	Ustav Jaderneho Vyzkumu Rez (Nuclear Research Institute)
UVA	Universidad Valladolid

REPORTING PERIOD : FROM September 2000 TO August 2003

PROJECT START DATE : September 2000 DURATION : 36 months

Date of issue of this report : October 2003

Project funded by the European Community under the ' 5th Framework' Programme (1998-2002)

Contract FIKW-CT-2000-00049

(September 2000–August 2003)

PYROREP

Pyrometallurgical Processing
Research Programme

Final Report

October 2003

Project co-funded by the European Community
under the 5th Framework Programme

PYROREP

Programme Co-ordinator

H. Boussier
CEA

Work Package Co-ordinators

WP1	WP2	WP3
J.P. Glatz – R. Malmbeck ITU	J. Lacquement CEA	G. Marucci ENEA

Pyrometallurgical Processing Research Programme

Participants

AEA-T
- S. Beetham
- J. Jenkins
- H. Sims

BNFL
- R. Lewin
- R. Thied
- K. Franklin
- D. Hebditch
- M. Hetherington
- H. Madrick

CEA
- H. Boussier
- O. Conocar
- C. Hamel
- A. Laplace
- H. Rabiller
- J. Lacquement
- T. Advocat

CIEMAT
- P. Diaz Arocas
- C. Caravaca
- G. Cordoba

CRIEPI
- T. Inoue
- K. Kinoshita
- T. Koyama

ENEA
- G. Marucci
- E. Baicchi
- G. De Angelis
- R. Nannicini
- L. Pilloni
- G. Cosoli

ITU
- R. Malmbeck
- J. Serp
- J.P. Glatz

NRI
- J. Uhlíř
- P. Souček
- R. Zvejšková

POLiMi
- C. Mazzocchia

UPS
- P. Taxil
- P. Chamelot

UVA
- Y. Castrillejo
- R. Bermejo
- E. Barrado

Document structure

Part 1 – Executive Summary

Part 2 – Detailed Final Report

Part 1 – Executive Summary

Executive Summary

1 Objectives

The operation of nuclear fission reactors gives rise to long-lived radionuclides, which may be considered a potential risk born by future generations that must be minimized. To achieve this goal, these radionuclides can be transmuted by neutron irradiation in fast burner reactors or in dedicated reactors such as accelerator-driven systems (ADS). The spent fuel and/or targets from these reactors could be processed by pyrochemical methods.

An other possibility would be to immobilize the separated radionuclides in specific high durability matrixes before geological disposal.

PYROREP is a R & D program aiming to:

- Determine the practicalities of separating uranium, plutonium and minor actinides from FP using pyrochemistry in a molten chloride or fluoride system.
- Obtain basic data to allow conceptual design and assessment of reprocessing processes suitable for fuels and targets
- Consolidate and revive European expertise in pyroprocessing

2 Main results

2.1 Fluoride media

Two separation concepts were investigated in fluoride media: selective electrodeposition and reducing extraction; in both cases the objective was to separate the actinides collectively from the fission products.

➢ Selective electrolytic extraction of the actinides

The objective of these studies is to determine whether it is possible to separate the actinides from the fission products by selectively reducing the former on a cathode, while the fission products remain in the molten salt. The CEA and NRI worked on similar concepts in different salt media:

- The CEA study was limited to the basic mechanisms of cathodic reduction of UF_4, and NdF_3 in LiF-NaF and LiF-CaF_2.
- NRI conducted similar fundamental research on the reduction of NdF_3, UF_4 and ThF_4 in a fluoride salt mixture of LiF, NaF and KF known as FLiNaK, and in LiF-CaF_2. NRI also performed more technological studies for selection of suitable materials for the electrodes and for the electrolyser unit, and the development of a reference electrode.

The cyclic voltammogram clearly shows that U/Nd separation is possible, and measurements of thorium in FLiNaK indicate that U/Th separation should also be possible; however, the results of these studies are inconclusive with regard to the possibility of Th/Nd or Th/Gd separation in FLiNaK.

In order to allow measurements in FLiNaK salt, NRI fabricated a reference electrode from the design developed in the 1970s at ORNL, the constant electrode potential is provided by the redox couple Ni/Ni^{2+}. Corrosion studies were also carried out to select suitable construction materials for equipment used in molten LiF-NaF and LiF-NaF-KF salt media. Several high-nickel materials (pure nickel, Hastelloy C-276, MoNiCr and Inconel 718) were submitted to corrosion tests at 530°C in 99.998% argon atmosphere under steady-state conditions.

Other electrolysis cell component materials were tested.

- Reductive extraction of the actinides by aluminium in LiF/AlF_3

The CEA also worked on group separation of the actinides from fission products by reductive salt/metal extraction. Reductive extraction of CeF_3, PuF_3 and AmF_3 by aluminium can be described by the following equation:

$$MF_3(l) + Al(l) \leftrightarrow AlF_3 + M(l)$$

The partitioning of actinides (Pu, Am) and lanthanides (Ce, Sm) was studied in a LiF-AlF_3/Al-Cu system (78–22 mol%). The Pu, Am, Ce and Sm distribution coefficients were measured at 830°C for different initial AlF_3 concentrations.

The results obtained with plutonium, americium cerium and samarium in the (LiF-AlF_3)/(Al-Cu) medium show revealed the potential of this system for separating the actinides from the lanthanides. More exactly, with a salt composition corresponding to basic eutectic (LiF-AlF_3, 85–15 mol%), up to 99% of the plutonium and americium could be recovered in a single stage, with cerium and samarium separation factors exceeding 250. The experiments show that the distribution coefficients of these elements vary inversely with the AlF_3 concentration.

2.2 Chloride media

Systematic electrochemical studies of rare earth elements and uranium carried out at CIEMAT-UVA and of the actinides (Am, Pu) at ITU, have been undertaken to provide basic thermochemical and kinetic data to assess electrochemical separation paths in molten chloride media. In these studies a combination of transient electrochemical techniques such as cyclic voltammetry (CV) chronopotentiometry, and chronoamperometry have been used to investigate valency, mechanisms of reduction of the elements but also to investigate transport and deposition parameters such as diffusion coefficients and nucleation and crystal growth. In addition, relevant thermodynamic properties, e.g. standard potentials and activity coefficients have been calculated.

Stable oxidation states of the investigated elements were found to be (III) and (0) for Y, La, Ce, Pr, U and Pu. In the case of Nd and Am, oxidation state (II) and for U oxidation state (IV) also exist. Standard potentials of the different M(III)/M(0) couples were determined by emf measurements or for Nd and Am by transient techniques (CV) as the presence of Nd(II) and Am(II) prevents potentiometric determination. From the variation of the standard potential with temperature some basic thermodynamic data were calculated ($\Delta G_{M(III)}$, $\Delta H_{M(III)}$ and $\Delta S_{M(III)}$ of formation) and compared to reference state

data to obtain the activity coefficient ($\gamma_{M(III)}$). In addition diffusion coefficients were calculated and shown to possess temperature dependence according to the Arrhenius law.

Electrodeposition and separation experiments of actinides and lanthanides have been carried out onto solid (W, Mo, Ni and Al) and liquid (Cd and Bi) cathodes. It has been shown that the choice of cathode material onto which the actinides are deposited during electrolysis is essential. Two characteristics must be taken into account. On one hand, the metallic deposit must be stable enough to prevent undesired side-reactions. For example, in the case of deposition on solid cathodes the deposited metallic Am reacts with the dissolved Am (III) to form Am (II) according to:

$$2\ Am(III) + Am(0) \leftrightarrow 3\ Am(II)$$

On the other hand, enough difference in reduction potentials between MA and Ln is needed to allow a selective electrochemical reduction of actinides. From the obtained potentials and the activity coefficients higher separation factors (actinides from lanthanides) should be obtained in the LiCl-KCl / Bi system compared with the LiCl-KCl / Cd system. The selective recovery of actinides on a Bi cathode, however, proved difficult due to the small difference in reduction potentials between actinides and lanthanides.

It was shown that actinides (Pu and Am) form stable surface alloys with solid Al and that the difference in reduction potential onto Al is sufficient to allow also a separation of MA from Ln. Such a separation was successfully demonstrated in which Pu and Am was separated from Nd by electrolysis.

In a joint CRIEPI-ITU collaboration an experimental setup has been built to demonstrate pyroprocessing of irradiated fuel. Molten salt reprocessing of spent metal alloy fuel is the main reprocessing activity in the fuel cycle developed by CRIEPI. The setup has been equipped with an electrorefiner and installations for molten salt / molten metal extraction and recently also for chlorination experiments. Electrorefining of unirradiated alloy fuel (71 wt% U, 19 wt% Pu, 10 wt% Zr) already fabricated in ITU for transmutation experiments, has been carried out to obtain basic knowledge of 1) anodic dissolution behaviour of the alloy, 2) recovery of U onto a solid cathode and 3) recovery and separation of actinides into a liquid cadmium cathode.

In order to investigate electrorefining of fuel materials, electrorefiners installed in glove boxes have been commissioned at ENEA (Pyrel facility) and at BNFL. In BNFL a number of rate controlling parameters on electrorefining of An in molten LiCl-KCl eutectic have been assessed, such as the effect of concentration, mass transport, electrode surface, electrode potential and temperature. There appeared to be two main controlling parameters; the concentration of the electrochemically active species in the salt and the rate at which metals enter the liquid Cd cathode. Surface effects at the liquid Cd electrode surface were found to be complex. It was found that disturbing the electrode surface by using a pounder was important to avoid solid U metal forming at the liquid metal cathode surface at a greater rate than it could migrate into the bulk metal Cd. The Pyrel facility was built and cold tests were completed during the final year of the contract.

This experimental device would be available for a future EC pyrochemistry programme.

In the CRIEPI-ITU collaboration, several runs of electrorefining of unirradiated UPuZr alloy with addition of $LnCl_3$ salts or with unirradiated UPuMALn alloy have been carried out using liquid Cd cathodes. Separation factors were calculated from measurement of the concentration of the elements in the salt and the Cd phases. Typical separation factors of U, Np, Am, Cm and Ce against Pu were about 2.04, 0.949, 0.597, 0.534 and 0.0393,

respectively. These experiments showed that An can be effectively collected on a liquid Cd cathode and that a separation of An from RE elements should be possible.

The conversion of oxide fuel to halide form might be a necessary step in order to prepare oxide fuel for electrorefining processes in molten chloride salts. An extensive study has been undertaken at CIEMAT and UVA to determine the stability of the compounds formed and reaction rates during chlorination using different chlorinating mixtures. Using basic data, such as solubility products, equilibrium potentials of redox couples, thermochemical data and activity coefficients, potential acidity diagrams (E-pO^{2-}) could be constructed for the different elements. By comparing such a diagram with the E-pO^{2} of different chlorination mixtures it was possible to predict the appropriate chlorinating mixture for RE oxides and uranium oxide.

In chlorination experiments with Ln oxychlorides (CeOCl, LaOCl, PrOCl, NdOCl) and RE oxides (CeO_2, La_2O_3, Pr_6O_{11}, Nd_2O_3, Y_2O_3) using HCl as chlorinating gas, the end product was RE(III) chloride and efficiencies close to 100% could be obtained. It was shown that different chlorination kinetics were obtained for different chlorinating mixtures, the slowest being Cl_2. The reaction rates were also dependent on sample and surface size and on the RE oxide element, in the case of HCl(g) the order is:

$$v(CeO_2) \cong v(La_2O_3) \cong v(Y_2O_3) > v(Nd_2O_3) > v(Pr_6O_{11})$$

Experiments using UO_2 and simfuel have also been carried out to investigate the chlorination of oxide fuel materials. Efficiencies higher than 90% were obtained using HCl and Cl_2+C with faster kinetics obtained for carbochlorination. The influence of particle size on direct chlorination of UO_2 is a critical parameter. Lowest particle size fraction or the highest surface area provided the highest efficiencies and dissolution rates. The dissolution behaviour of simfuel has been found similar to that of UO_2.

The average surface area of irradiated fuel, compared to unirradiated fuel material, is larger due to the irradiation effect on the fuel structure. Dissolution rates and efficiencies are therefore expected to be higher. This indicates that direct chlorination of irradiated pellets should be possible with promising yields.

2.3 General studies

Electrochemical cell models have been developed by ENEA to describe the electrochemical behaviour of a solid-anode solid-cathode electrorefiner in steady-state and in unsteady time-dependent conditions. Two model have been developed: the first describes constant current working condition and the second the constant cathode-potential working mode.

The models do not take stirring effects into account, so they describe only a diffusive process. The developed models correctly describe the phenomenology of the diffusive electrorefining processes. It is possible to model the behaviour of different ionic species as a function of time in different fused salt and liquid anodes. It is possible to study geometrical effects such as the device dimensions or the shape and dimensions of the electrodes. With the same technique it is possible to consider electrorefining processes with liquid cathodes. Future development could take the stirring effect into account and these codes will be validated using data coming from Pyrel device constructed by ENEA.

System studies for a global assessment of performance and waste generation have been carried out on three different processes based on separation principle studied under this contract: reductive salt/metal extraction (CEA), electrowinning/electrolysis (ENEA), and Molten Salt Reactor Transmutation (NRI).

None of the elementary separation steps studied will be able to recover 99.9% of the actinides with less than 5% of the total FP negative reactivity in one step. Additional steps will be necessary to achieve this objective.

Separating the actinides from the fission products through reductive extraction by aluminium in a LiF/AlF_3 medium is very promising. The LiF/AlF_3 salt composition range ([15 mol% < AlF_3 < 35 mol%]) meets the performance objectives: 99.9% of the actinides are extracted with less than 5% of the initial negative reactivity of the FP in less than three theoretical extraction stages, although this efficacy is possible only if upstream steps are implemented to eliminate some volatile alkaline FP and the noble metal FP.

Further work is necessary on the downstream process steps (aluminium stripping and recovery of actinide oxides), which have not been optimised in this conceptual system study. Special consideration will have to be given to waste management.

The analysis of electrolytic processes shows that in the case of metallic fuel electrowinning on solid and liquid cathodes can recover most of the An without entraining excessive amounts of Ln, but the recovery of the remaining An to reach 99.9% will require the implementation of two selective reductive salt/metal extraction steps using Cd+Li and Cd+U couples.

In the case of oxide fuel processing, an upstream reduction step with Li is implemented to transform the oxides to metal. This step will contribute to eliminating a significant fraction of Ln that will improve performance during the following electrolytic separation.

For these processes implementing chloride salts, the spent salt management will have to be carefully studied either to develop a suitable containment matrix or to imagine a process capable of eliminating the chloride by transforming the chloride salt stream to oxides that could be vitrified.

A conceptual global processing scheme has been proposed for a MSTR based scenario. This flowsheet implements many of the dry process principles used in fluoride media including fluoride volatility, noble gas removal, reductive salt/metal extraction, and electroseparation.

3 Conclusion and recommendations

Within the scope of the PYROREP contract, substantial progress was made by the project working teams. Many basic data values concerning the behaviour of fission products and actinides (U, Pu and Am) in molten salts and metals were measured for first time or confirmed in both fluoride and chloride media. It would be logical to continue this work notably by acquiring basic data first on curium and subsequently, if technically feasible, on the transcurium nuclides. These elements are not found in substantial quantities in spent fuel today, but the their presence will tend to increase appreciably as the actinides become subject to multiple recycling in MOX fuel or in double-component or double-strata burner systems.

The main R&D focus of the PYROREP contract was on the separation step, which represents the core of the future pyrochemical separation process(es). In fluoride media, the investigation of reductive salt/metal extraction yielded very promising results for both An recovery and FP decontamination yields. For electrolytic processes in chloride media it has been shown that, from the strict standpoint of actinide/lanthanide separation, an aluminium cathode would provide better results than a cadmium cathode, although the

latter could be used if it is not indispensable to recover and separate the actinides from the lanthanides with very high efficiency. Conversely, recovering the separated actinides from an aluminium cathode appears to be more difficult than for a liquid cadmium cathode which can easily be evaporated. Development work should be carried out on the use of an aluminium cathode to take advantage of these potentially interesting results.

The data acquired to date are sufficient to begin designing and quantifying preliminary schemes for reprocessing processes. From the standpoint of a fuel cycle policy based on Partitioning and Transmutation (P&T), effective implementation will require not only a very high actinide recovery factor (typically 99.9%) but also sufficient FP decontamination to recycle less than 5% of the initial negative reactivity of the FP with the actinides. This criterion should also be confirmed and/or qualified by taking into account not only the neutronic criterion but also the FP content recycled in the burner system and the risk of creating a holdup loop for some FP in the cycle. The system studies clearly show that the required performance cannot be obtained by a single separation stage. In each case at least two and perhaps three separation stages based on different separation principles must be implemented (electrorefining plus reductive salt/metal extraction in one case, or volatilization of some FP in a reducing medium followed by digestion of noble metals by a metal phase and reductive extraction in the second case). It is still necessary to demonstrate experimentally by combining all these process steps that the announced performance can be achieved.

An/FP separation, which constitutes the core of the process, will probably be applied to a variety of different fuels (oxide, metal, nitride, carbide, or molten fluoride) and should therefore logically be the primary focus of attention. However, An/FP separation must be preceded and followed by equally important steps designed to dissolve the elements in the molten salt upstream, and to recover the finished products downstream. These steps depend to a greater extent on the nature and type of the fuel, and must be investigated in greater detail in the future as the fuel specifications are defined.

Pyrochemical processes generate metal and salt waste flows of a substantially different nature than the waste currently produced by aqueous processes. A major effort will be necessary in the future to optimize the management routes for this waste—particularly for chlorinated salt waste, which is incompatible with the glass matrices used today—either by dechlorination or by developing dedicated containment matrices such as sodalites.

Unlike enhanced aqueous reprocessing processes that can be implemented with technology comparable to that used in today's reprocessing plants, the deployment of pyrochemical processes would require considerable technological R&D that must be undertaken as soon as the fuel specification for the future systems is sufficiently defined. Today the effort could focus on developing the continuous salt/metal contactors that will be necessary regardless of the type of fuel and the separation technique finally adopted.

It is also clear that pyrochemistry R&D efforts should be better coordinated in each European country to make the best use of the available human and material resources. The PYROREP contract has made an initial contribution toward this objective by pooling the research teams and creating a community of researchers who—even if their strategic objectives differ—have acquired together and now share a common wealth of knowledge in this area. From this standpoint it will be essential in the future to facilitate and encourage contacts and exchanges between teams of researchers. Independently of the very large quantity of scientific results obtained during the three-year work program, an important additional benefit of this contract has been for different research groups to interact and exchange their experience. The project has been a vehicle for interaction

among the persons involved and has led to increased knowledge and skills in handling molten salts and radioactive materials.

We hope that this fruitful collaboration will continue and be further developed under the next EUROPART 6th framework programme.

Part 2 –
Detailed Final Report

Contents

Section 1: Objectives

1 Overview

The operation of nuclear fission reactors gives rise to long-lived radionuclides, which may be considered a potential risk borne by future generations that must be minimized. To achieve this goal, these radionuclides can be transmuted by neutron irradiation in fast burner reactors or in dedicated reactors such as accelerator-driven systems (ADS). The spent fuel and/or targets from these reactors could be processed by pyrochemical methods.

PYROREP is a R & D program with the following objectives:

- Assess the feasibility of separating uranium, plutonium and minor actinides from FP using pyrochemistry in a molten chloride or fluoride system.
- Obtain basic data to allow conceptual design and assessment of reprocessing processes suitable for fuels and targets
- Consolidate and revive European expertise in pyroprocessing.

The objective of all the separation methods is to separate the fission products (FP) from the transuranic nuclides (TRU) with a suitable yield (99%–99.9%) to ensure sufficient decontamination of the FP. Three main methods are generally proposed for this purpose in molten salts:

- Selective TRU precipitation as used, for example, in so-called RIARR process.
- Electrolytic methods. Two main principles can be implemented. The first, electrowinning, is applied directly to metal fuel: the TRU elements are dissolved in the molten salt at the anode and can be electrolytically reduced and deposited to the cathode. The second, electrolysis, requires prior dissolution of the elements in the salt in halide form; then, as in electrowinning, the TRU are selectively reduced and deposited to the cathode.
- Salt/metal reductive extraction. The fuel elements are previously dissolved in a molten salt and the salt is contacted with a metallic phase that selectively reduces the TRU, which are transferred into the metallic phase while the FP remain in the salt.

Under this contract, we focused on the last two separation principles (electrolytic methods and salt/metal reductive extraction) as well as on some of the related subsidiary steps.

Separation is only an elementary step on the way toward a reprocessing process. To devise such a process, separation will have to be completed with subsidiary steps upstream to convert the spent fuel or targets into a suitable form, and downstream to recover the TRU in a form suitable for recycling and to manage the process waste.

Although technological issues are obviously of prime importance in developing pyrochemical processes due to the use of high temperatures, corrosive reagents and highly radioactive elements, these considerations were clearly outside the scope of this contract dedicated to more fundamental chemical issues.

2 Report framework

Eleven organisations from four European countries together with the Karlsruhe Joint Research Centre and the CRIEPI in Japan were involved in this programme. This report is a collective work performed by a large number of authors (see below for the participating countries, organisations and authors).

The study has been divided into three parts:

- Part 1 – Studies of separation methods implemented in molten fluoride media.
- Part 2 – Studies of separation methods implemented in molten chloride media.
- Part 3 – General studies regarding both fluoride and chloride media.

3 Partnership

Eleven organizations or laboratories participated in this study as direct contractors (DC), subcontractors (SC) or partners of a direct contractor (P). This Final Report is the result of 17 individual contributions of working teams. The organizations are listed in alphabetical order:

AEA-T	Atomic Energy Authority – Technology (SC)
BNFL	British Nuclear Fuel Limited (DC)
CEA	Commissariat à l'Énergie Atomique (DC)
CIEMAT	Centro de Investigaciones Energéticas, Medioambientales y Tecnologicas (DC)
CRIEPI	Central Institute of Electric Power Industry (DC)
ENEA	Ente per le Nuove Tecnologie, l'Energia e l'Ambiente (DC)
ITU	Institute for Transuranium Elements – Joint Research Centre (DC)
NRI	Ustav Jaderneho Vyzkumu Rez (Nuclear Research Institute) (DC)
UVA	Universidad Valladolid (SC)

Universities have also been associated with the project through bilateral cooperation agreements.

POLiMi	Univ. Politecnico di Milano (as ENEA partner)
UPS	Université Paul Sabatier, Toulouse (as CEA partner)

Overall co-ordination of the research programme was ensured by the CEA (H. Boussier). Each work package had a separate co-ordinator:

WP1:	ITU
WP2:	CEA
WP3:	ENEA

The contributing authors and other persons whose help or technical assistance in compiling the results must be acknowledged are named on page v of this Final Report.

Section 2:
Scientific and technical description of the results

1 Fluoride media

1.1 Separation by salt/metal extraction

1.1.1 Introduction

This work was undertaken to investigate the separation of the actinides from the lanthanides by reductive extraction in a molten fluoride/liquid metal medium. Previously published work in this area concerns the LiF-BeF_2/Li-Bi [1,2] or LiF-CaF_2/Mg-Zn [3] systems. However, based on thermodynamic considerations concerning actinide and lanthanide activity coefficients in liquid metals as well as tests concerning U/La separation, aluminium was identified as both a solvent and more promising reducing agent for our objective [4].

This study therefore addresses the distribution of actinides (Pu, Am) and lanthanides (Ce, Sm), in the LiF-AlF_3/Al-Cu system (78-22 mol%). In this system, Cu is used only to increase the weight of the metal phase and facilitate settling.

1.1.2 Experimental work

1.1.2.1 Reactants

Al, Cu, LiF, AlF_3, CeF_3 and SmF_3 were supplied by Sigma-Aldrich with better than 99.99% purity. The fluorides were packaged by the supplier in ampoules under argon atmosphere with an initial water content of less than 100 ppm. AmF_3 was synthesized by precipitating Am(III) in a nitric acid medium using a 2M hydrofluoric acid solution. The precipitate was washed in 0.1M hydrofluoric acid, in water, and in acetone, then dried in flowing air at room temperature. Pu was in a nitric acid solution as Pu(IV), requiring prior reduction to Pu(III). This was achieved using ascorbic acid as a reducing agent and hydrazinium nitrate to control the nitrous acid concentration and prevent the oxidation of Pu(III) to Pu(IV). Thermogravimetric analysis of the PuF_3 precipitate showed that it included 4.1% water and that drying for 4 hours at 250°C under argon atmosphere was sufficient to obtain the anhydrous product. The X-ray diffraction spectra of the PuF_3 powder before and after drying were similar to the spectrum of anhydrous PuF_3 synthesized by fluorination of PuO_2, indicating that water trapped during crystallization was not incorporated into the lattice. These observations corroborate previous studies by [5]. For lack of suitable instrumentation, a comparable study was not performed with AmF_3. Nevertheless, considering the very similar crystalline and thermodynamic properties of PuF_3 and AmF_3 it can reasonably be assumed that the conditions necessary for dehydrating them will be also be similar. Al-Cu alloy (78-22 mol%) was prepared by dissolving a suitable quantity of copper in liquid aluminium at 800°C. This operation was performed under argon scavenging in a stainless steel reactor using a boron nitride crucible. The argon used to scavenge the reactor was supplied by Air Liquid with very high purity: N60 grade, $H_2O < 0.6$ ppm and $O_2 < 0.1$ ppm.

1.1.2.2 Equipment

The experiments were carried out using the device (high-temperature liquid-liquid contactor: HTLLC) shown in **Figure 1**. Two similar devices were used: one for the tests with Ce and Sm and another—in a glove box—for the tests involving Pu and Am. The HTLLC uses two crucibles: the metal is melted in the upper crucible, then poured through a stoppered orifice into the lower crucible. This system has two advantages: it accurately determines the starting time for kinetic studies and limits the quantity of metallic oxides in the extraction crucible. Since all the liquid metal is not poured, the Al and Cu oxides in the film that forms at the surface of the molten metal are not transferred into the lower crucible. The lower crucible is the extraction vessel in which the two phases are contacted and stirred.

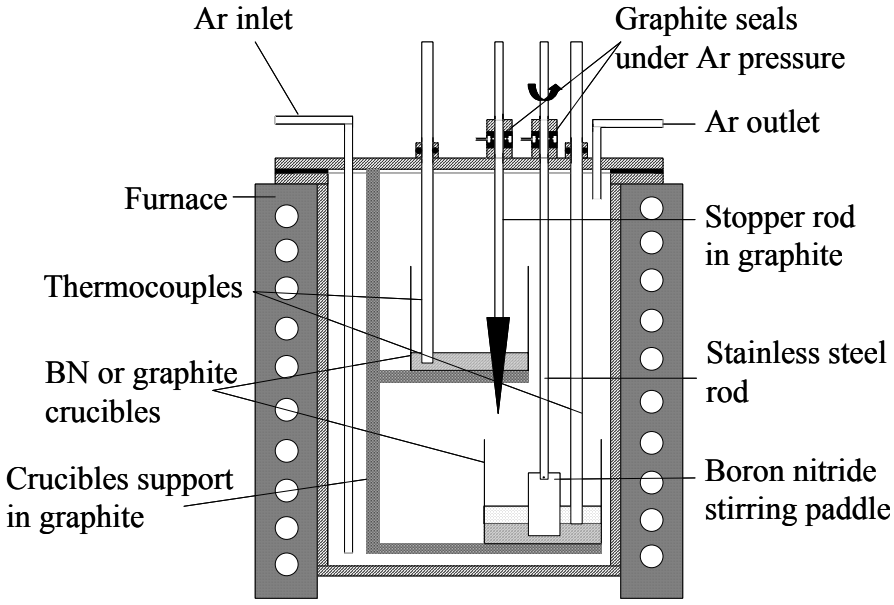

Figure 1. Schematic cross section through the high-temperature liquid-liquid contactor (HTLLC)

1.1.2.3 Protocol

The salt mixture, 15 to 20 g of powder containing the solvent (LiF-AlF_3) and solutes (CeF_3, PuF_3, SmF_3 or AmF_3), was thoroughly blended and placed in the extraction crucible. The LiF/AlF_3 ratio and the solute concentration varied during each test. About 45 g of solid Al-Cu alloy (78-22 mol%) was then added to the extraction crucible. The reactor was then scavenged with argon and the temperature increased to 250°C for 12 hours to dehydrate the salt. The temperature was then increased to 830°C to melt the two phases. While the melt was stirred at about 60 rpm, 15 to 25 g of alloy were poured by raising the stopper. The two phases were maintained in contact for 3 hours, which was amply sufficient to reach equilibrium. Salt and liquid metal samples were then taken for analysis using quartz tubes and a syringe. The salt samples were dissolved at 90–100°C in a mixture of HNO_3 (3M) and $Al(NO_3)_3$ (1M). The metal samples were dissolved in a mixture of HNO_3 (4M) and HF (0.7M). The Ce and Sm concentrations in solution were determined by ICP-AES. Pu and Am were analyzed counting and α spectrometry.

1.1.3 Results and discussion

1.1.3.1 Thermodynamic expression of distribution coefficients

Reductive extraction of CeF_3, PuF_3 and AmF_3 by aluminium can be described by the following equation:

$$MF_3(l) + Al(l) \leftrightarrow AlF_3 + M(l)$$

The thermodynamic constant K^{o}_{M} of this reaction can be calculated from the free enthalpy of formation of the pure species involved (**Table I**). The reference state in this study is the pure compound in the liquid state, except for AlF_3, which sublimates, and for which the reference state is the pure solid.

Table I. Free enthalpy of formation at 830°C of Sm, Ce, Pu and Al fluorides

Compound	ΔG°_{f} (kJ·mole^{-1})	Ref
SmF_3(l)	-1380.6	[6]
SmF_2(l)	-984.4	[7]
CeF_3(l)	-1394.9	[8]
PuF_3(l)	-1283.5	[9]
AlF_3	-1222.9	[6]
Sm(l)	1.7	[6]

K^{o}_{M} can also be expressed in terms of the equilibrium activities of the species in solution: $K^{o}_{M} = \frac{a_{AlF_3} \cdot a_{M}}{a_{MF_3} \cdot a_{Al}}$. This can be rewritten with the distribution coefficient D_M, the ratio of the molar fractions x of M in the metal and in the salt at equilibrium, and the activity coefficients $\gamma = a/x$:

$$D_M = K^{o}_{M} \frac{a_{Al}}{x_{AlF_3} \cdot \gamma_{AlF_3}} \frac{\gamma_{MF_3}}{\gamma_{M}} \quad \textbf{(1)}$$

The activity coefficient terms reflect deviations from ideality in both phases. They may be expressed with respect to the variation of the free energy ΔG^{exc} of dissolution of the pure liquid (except for solid AlF_3) using the relation $\Delta G^{exc} = RT \ln\gamma$.

In the case of Sm extraction, allowance must be made for its oxidation state II, which is stable in fluoride media. Its transfer into the metal can thus be considered in two steps: reduction of Sm(III) to Sm(II) in the salt, and the actual transfer into the metal:

$$3SmF_3(l) + Al(l) = 3SmF_2(l) + AlF_3 \qquad K^{o}_{1}$$

$$1.5SmF_2(l) + Al(l) = 1.5Sm(l) + AlF_3 \qquad K^{o}_{2}$$

At 830°C, K°_{Ce}=7.2 × 10^{-9}, K°_{1}=41.7 and K°_{2}=7.38 × 10^{-13}; the Sm(III)-Sm(II) reduction reaction is thus the predominant reaction, confirming the two-stage transfer mechanism. The Sm distribution coefficient can be expressed as follows:

$$D_{Sm} = K^{\circ 2/3}_{2} \frac{\gamma_{SmF_2}}{\gamma_{Sm}} \left(\frac{a_{Al}}{\gamma_{AlF_3} \cdot x_{AlF_3}} \right)^{2/3} \quad \textbf{(2)}$$

1.1.3.2 Effect of salt composition

1.1.3.2.1 Variation of distribution coefficients with x_{AlF_3}

Any variation in the AlF_3 composition will influence the distribution coefficients directly by modifying x_{AlF_3} in equations (**1**) and (**2**), but also indirectly by modifying γ_{AlF_3}, γ_{MF_3} and γ_{SmF_2}. In a binary mixture such as LiF-AlF_3, the notion of fluoroacidity accounts for the major variation of the activity coefficients [10,11]. It is characterized by the activity of the F^- ions in solution, which depends on the LiF/AlF_3 ratio. LiF is highly dissociated in the melt and can be considered as a fluorobase (F^- donor). Conversely, AlF_3 is known to be a strong F^- acceptor, forming AlF_{3+x}^{x-} anions (where x = 1, 2 or 3), making it a fluoroacid.

The Pu, Am, Ce and Sm distribution coefficients were measured at 830°C for different initial AlF_3 concentrations. As the quantities of the element to be extracted were very small compared with Al, the AlF_3 concentration at equilibrium was virtually the same as the initial value. The initial CeF_3, PuF_3, AmF_3 and SmF_3 concentrations (mol%) in the salt were the following: 3.7×10^{-1}, 9.4×10^{-2}, 1.5×10^{-2} and 5.5×10^{-1}, respectively. The Ce and Sm distribution coefficients were determined with about 10% uncertainty. The results for Pu and Am were of lower precision, mainly because of their very low equilibrium concentrations in the salt. The results (**Figure 2**) show that the distribution coefficients of these elements vary inversely with the AlF_3 concentration.

to the AlF_3 concentration. For Sm and Ce, this can be described by the linear relations $\log D_{Sm} = -7.02x_{AlF_3} + 0.17$ and $\log D_{Ce} = -4.76x_{AlF_3} + 0.21$. For Pu and Am it is difficult to quantify this variation reliably because of the measurement uncertainty.

Selective extraction of Pu and Am was effective over the full composition range investigated. For example, with a 15 mol% AlF_3 composition—corresponding to a binary LiF-AlF_3 eutectic at 710°C—and for a metal/salt molar ratio of about 1:1, over 99% of the Pu and Am can be extracted in a single stage with separation factors of about 250 for $S_{(Pu+Am)/}$ and about 500 for $S_{(Pu+Am)/Sm}$.

1.1.3.2.2 CeF_3 and SmF_2 activity coefficient variation versus fluoroacidity pF

Equations (**1**) and (**2**) allow us to write:

$$\log \gamma_{CeF_3} = -\log K_{Ce}^{o} + \log D_{Ce} + \log a_{AlF_3} - \log a_{Al} + \log \gamma_{Ce}$$

$$\log \gamma_{SmF_2} = -\frac{2}{3} K_2^{o} + \log D_{Sm} + \frac{2}{3} \log a_{AlF_3} - \frac{2}{3} \log a_{Al} + \log \gamma_{Sm}$$

The standard thermodynamic constants K_{Ce}^{o} and K_2^{o} are indicated in **Table I**; D_{Sm} and D_{Ce} correspond to the experimental values (**Figure 2**).

The activity coefficients of Ce and Sm in pure Al are available in the literature [11,12]: at 830°C, using the pure liquid as the reference, $\gamma_{Ce/Al} = 10^{-6.03}$ and $\gamma_{Sm/Al} = 10^{-6.46}$. The values in Al-Cu alloy (78-22 mol%) used here can be obtained by experimentally determining their distribution coefficients in pure Al and applying the relations based on equations (**1**) and (**2**):

$$\gamma_{Ce/(Al\text{-}Cu)} = \frac{D_{Ce/Al}}{D_{Ce/(Al-Cu)}} \cdot \gamma_{Ce/Al} \cdot a_{Al/(Al\text{-}Cu)} \text{ and } \gamma_{Sm/(Al\text{-}Cu)} = \frac{D_{Sm/Al}}{D_{Sm/(Al-Cu)}} \cdot \gamma_{Sm/Al} \cdot a_{Al/(Al\text{-}Cu)}^{2/3}.$$

In LiF-AlF_3 (85-15 mol%), $D_{Ce/Al} = 0.50$, $D_{Ce/(Al\text{-}Cu)} = 0.37$, $D_{Sm/Al} = 0.135$, $D_{Sm/(Al\text{-}Cu)} = 0.156$ and $_{Al/(Al\text{-}Cu)} \sim 0.78$; hence $\gamma_{Ce/(Al\text{-}Cu)} = 10^{-6.01}$ and $\gamma_{Sm/(Al\text{-}Cu)} = 10^{-6.47}$. In our operating

conditions, adding 22 mol% Cu to the Al thus does not significantly modify the Ce and Sm activity coefficients.

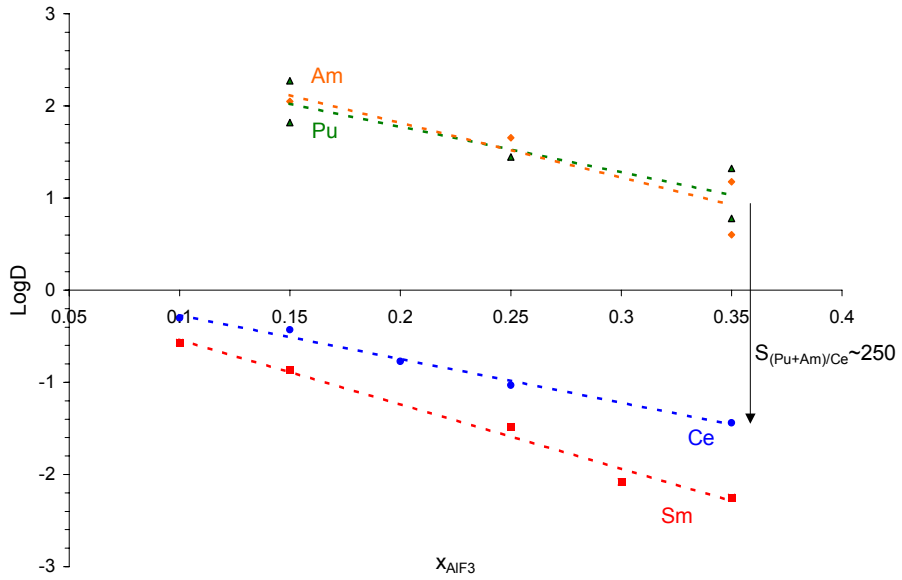

Figure 2. Pu, Am Ce and Sm partitioning in the LiF-AlF_3/Al-Cu system: effect of the salt composition.

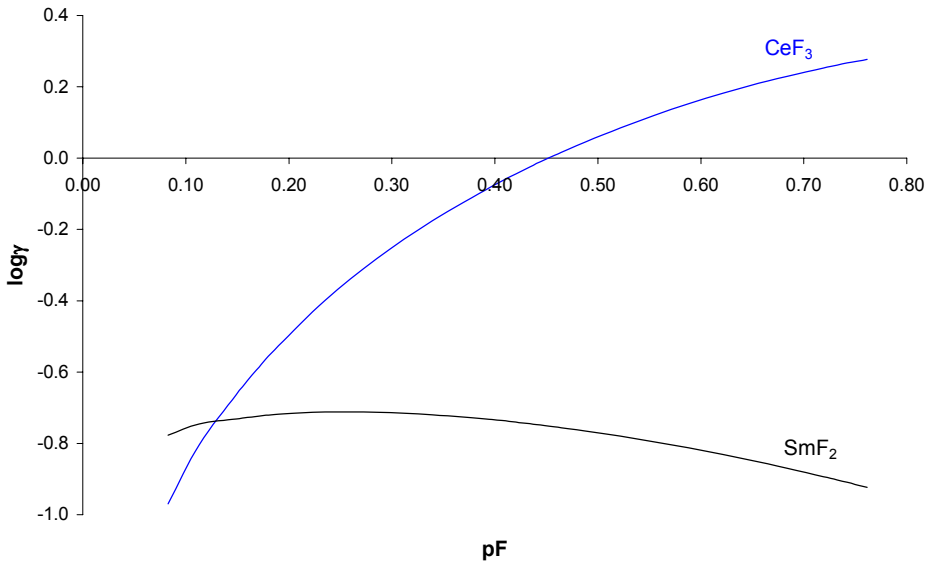

Figure 3. CeF_3 and SmF_2 activity coefficients versus the fluoroacidity of the medium at 830°C.

The relations between x_{AlF_3}, pF = $-\log a_{LiF}$ and a_{AlF_3} were determined electrochemically by Dewing [10]; the variation of the activity coefficients for CeF_3 and SmF_2 can thus be determined according to the fluorobasicity of the medium. As shown in **Figure 3**, CeF_3 and SmF_2 are solvated in very different ways in fluoride media. The activity coefficients for CeF_3 increase with the acidity of the medium, which is characteristic of an acidic compound. CeF_3 can thus be expected to be solvated in the form of CeF_{3+x}^{-x} complexes in fluoride media, like AlF_3. Conversely, the activity coefficient of SmF_2 diminishes only

very slightly when the acidity increases, making it a neutral or very slightly basic compound. It can thus be expected to be present as Sm^{2+}, SmF^{+} or SmF_2 in fluoride media. This difference in solvation behaviour could extend to Eu(II) and other trivalent actinides and lanthanides which have comparable ionic radii for a given oxidation state. The general tendency can be stated as follows: the separation of a divalent element from a trivalent element is enhanced in an acidic medium, in which the latter is much less stabilized than the former.

1.1.3.3 Effect of initial solute concentration

The preceding results were obtained for low solute concentrations (<0.1 mole·kg^{-1}). In this case, the activity coefficients in each phase and the distribution coefficients can be considered constant. This should no longer be true for higher concentrations of elements to be extracted, and the influence of the concentration on the distribution coefficients must be elucidated.

The Ce and Pu distribution coefficients in the LiF-AlF_3 (85-15 mol%)/Al-Cu (78-22 mol%) system were measured for various initial concentrations of both solutes in the salt (**Table II**). Experiments 1 to 8 were carried out on *in situ* samples of both phases at equilibrium. The salt mass varied from 15 to 20 g (15 to 25 g for the metal). To obtain a high Pu concentration, only 4 g of metal were used for test 9. The small quantity involved was not compatible with *in situ* metal sampling at equilibrium; the Pu concentration in the metal was determined after mechanically separating the metal and salt at room temperature.

Table II. Effect of concentration on the distribution coefficients of Ce and Pu in the LiF-AlF_3 (85-15 mol%)/Al-Cu (78-22 mol%) system at 830°C

Experiment	MF_3 Initial loading	Equilibrium		*D* (molar)
		$[M]_{salt}$ mg·g^{-1}	$[M]_{metal}$ mg·g^{-1}	
1	CeF_3 0.4 mol%	10.19	3.86	0.37 ±5%
2	CeF_3 1.5 mol%	60.54	13.55	0.21 ±5%
3	CeF_3 5.3 mol%	133.4	28.1	0.18 ±5%
4	PuF_3 0.1 mol%	0.023	4.22	187 ±12%
5	PuF_3 0.5 mol%	0.066	22.3	337 ±20%
6	PuF_3 0.9 mol%	0.070	39.2	583 ±25%
7	PuF_3 1.9 mol%	0.141	72.2	544 ±17%
8	PuF_3 2.6 mol%	0.35	93.3	285 ±38%
9	PuF_3 1.5 wt%	0.79	290 (1)	477 ±6%

(1) Value obtained after cooling to room temperature (complete dissolution of the metal phase)

In the case of Ce, the distribution coefficient diminished slightly as its concentration increased.

Considering the measurement uncertainties for Pu, it was difficult to correlate the distribution coefficients with the concentration. Nevertheless, the distribution coefficients were high even with high initial Pu loading in the salt (2.6 mol% = 18.8 wt%).

In test 8, the Pu concentration in solution in the liquid metal at equilibrium was below the expected value of 138 $mg \cdot g^{-1}$, suggesting that the Pu solubility limit was reached and that an intermetallic compound had precipitated.

1.1.4 Conclusion

An experimental device and protocol were developed to study the distribution of actinides and lanthanides in molten fluoride/liquid metal media.

The results obtained with plutonium, americium, cerium, and samarium in the (LiF-AlF_3)/(Al-Cu) medium revealed the potential of the system for separating the actinides from the lanthanides. More exactly, with a salt composition corresponding to the basic eutectic (LiF-AlF_3, 85-15 mol%), up to 99% of the Pu and Am could be recovered in a single stage, with cerium and samarium separation factors exceeding 250.

The effect of the AlF_3 concentration in the salt was investigated. The distribution coefficients logically diminish as the initial AlF_3 concentration rises (AlF_3 is a reduction reaction product). A thermodynamic model of extraction versus fluoroacidity was developed on the basis of the experimental results for cerium and samarium. The model clearly reveals the difference in solvation between divalent and trivalent lanthanides in fluoride media.

The influence of the solute concentration on the distribution coefficients was also evaluated: high initial concentrations of the elements to be extracted (about 20 wt% in the salt), were not detrimental to the extraction performance.

1.2 Electrolytic separation study

1.2.1 CEA contribution

1.2.1.1 Introduction

The objective of this study was to evaluate the electrolytic separation of actinides and lanthanides in a molten fluoride medium; the work presented here was carried out under a doctoral research programme in collaboration with the Chemical Engineering Laboratory of Paul Sabatier University in Toulouse, France.

The study first addressed the feasibility of electrolytic extraction of uranium from a U-Nd mixture. Three subject areas were investigated:

- Electrochemical system with 2 solutes

  Study of the reduction mechanisms of neodymium(III) fluoride and of uranium(IV) fluoride

- Electrolytic deposition of U

  Prior reduction of the medium to uranium(III), since uranium metal reacts with U(IV) according to the disproportionation reaction: $U + 3UF_4 \leftrightarrow 4UF_3$. This reduction step is the key to obtaining massive U deposits with satisfactory yields and allows a comprehensive study of U(III)/U(0) system (reduction mechanism).

  Tests on various solid electrode materials to obtain pure and alloyed U deposits.

➢ U-Nd separation

Selection of the solvent and operating conditions; effects on observation of the 2 electrochemical systems (temperature, electrode materials). Determination of the available potential range between 2 reduction peaks to demonstrate the feasibility of separation by U deposition.

1.2.1.2 NdF_3 reduction mechanism

Because of the highly reducing properties of neodymium, investigating the reduction of Nd(III) ions depends on the electrochemical window provided by the fluorinated solvent. A thermodynamic study indicates that no reduction of neodymium ions is observed in LiF-KF and LiF-NaF solvents. In LiF-CaF_2 (**Figure 4**) and pure LiF, however, the Nd(III) ion reduction wave can be observed (Ic/Ia couple). The theoretical work confirmed by experimental studies led us to select a mixture of LiF-CaF_2 salts as the solvent. Replacing sodium (or potassium) by the calcium cation extends the working range of the solvent, but at the cost of a higher working temperature.

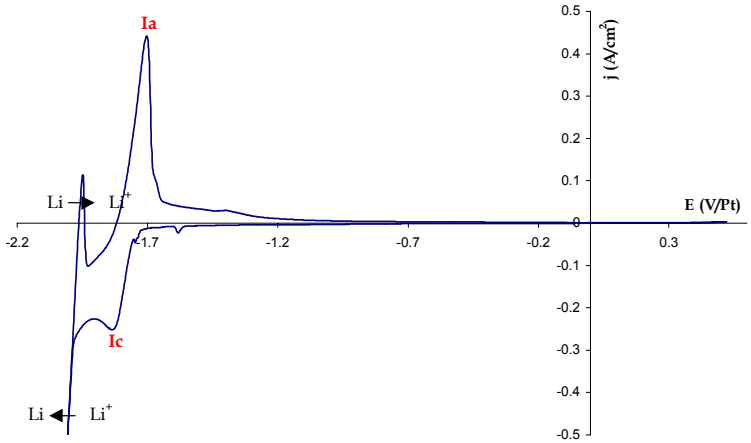

Figure 4. Cyclic voltammogram on Mo in LiF-CaF_2 + NdF_3 (2.4 wt%) at 810°C, scan rate 0.1 V/s, graphite counterelectrode, Pt quasi-reference electrode, S=4.11cm^2

Cyclic voltammetry (**Figure 4**) and chronopotentiometry with and without current reversal (**Figure 5**) were carried out on an unalterable Mo electrode in LiF-CaF_2 at 810°C.

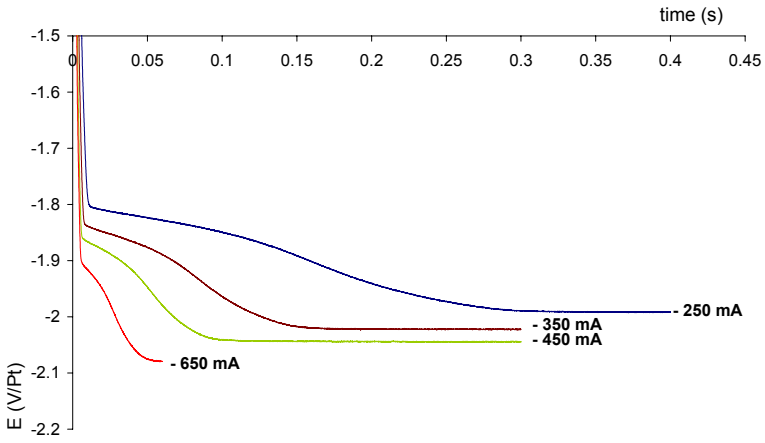

Figure 5. Chronopotentiograms on Mo in LiF-CaF_2+NdF_3 (2.4 wt%) at 810°C; graphite counterelectrode, Pt quasi-reference electrode, *S* = 0.411 cm^2

The results show that the reduction process involves a single step in which 3 electrons are exchanged, and which is limited by Nd(III) diffusion. Analysis of the results shows that an insoluble species does indeed form on the electrode surface and that the reaction leads to the formation of Nd metal.

1.2.1.3 UF_4 reduction mechanism

Uranium is less reductive than neodymium, and a thermodynamic approach suggests that promising results can be obtained with various Li, Na, K, or Ca fluoride salt mixtures.

LiF-NaF was selected to study the reduction mechanism of UF_4 because of its lower melting point than LiF-CaF_2.

This study involved cyclic voltammetry (**Figure 6**), chronopotentiometry with and without current reversal (**Figure 7**), and square-wave voltammetry with an unalterable Ag electrode.

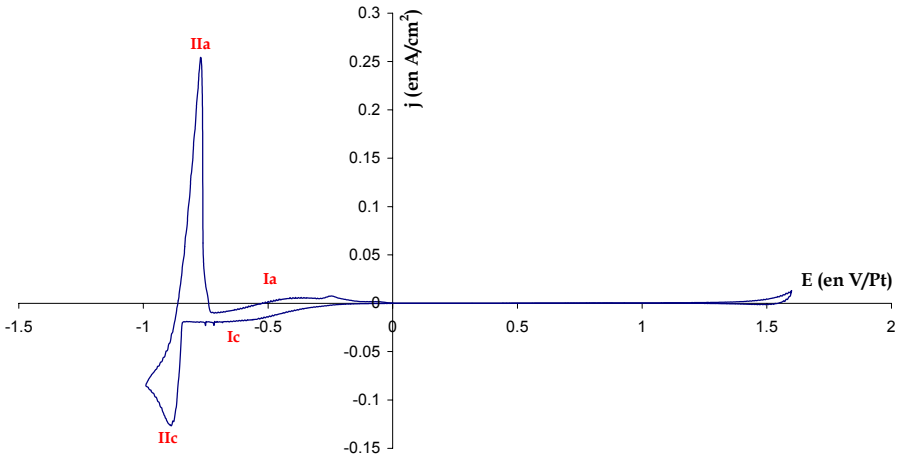

Figure 6. Cyclic voltammogram on Ag in LiF-NaF + UF_4 (1.6 wt%) at 720°C, scan rate 0.1 V/s, graphite counterelectrode, Pt quasi-reference electrode, S=0.35cm_2

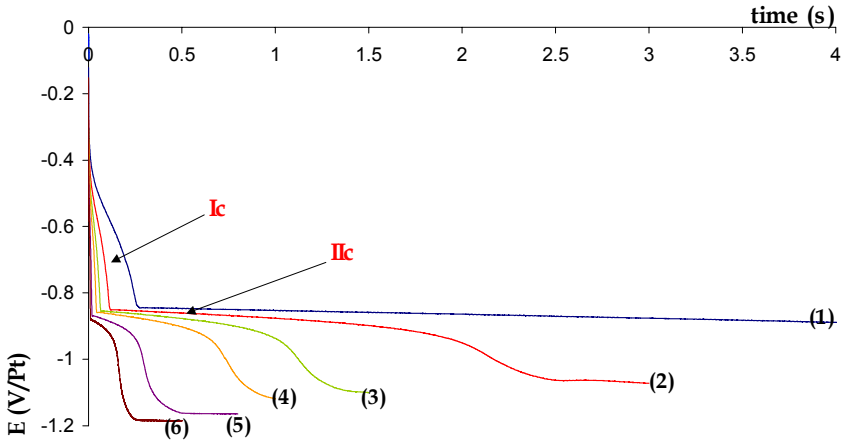

Figure 7. Chronopotentiograms on Ag in LiF-NaF + UF4 (1.6 wt%) at 720°C; graphite counterelectrode, Pt quasi-reference electrode, *I* = (1) -20, (2) -30, (3) -40, (4) -50 (5) -75 (6) -100 mA, *S* = 0.35 cm^2

The results indicate a two-step reduction process: 2 cyclic voltammetry waves (**Figure 6**) and 2 chronopotentiometry plateaus (**Figure 7**) in which first 1 electron then 3 electrons are exchanged. The first step corresponds to a soluble/soluble system and is limited by U(IV) diffusion. The results show the formation of an insoluble species on the electrode surface during step IIc, with partial redissolution of U metal due to the disproportionation reaction: $U + 3UF_4 \leftrightarrow 4UF_3$.

In order to perform a thorough study of the second step in the reduction process, the melt was first chemically reduced with uranium metal as the reducing agent. The study was carried out in two different media: LiF-NaF at 720°C and LiF-CaF_2 at 810°C.

The tests in LiF-NaF show that uranium metal is unstable and becomes oxidized, completely dissolving in the medium. Uranium probably oxidizes as a mixture of U(III) and U(IV). Nevertheless, at the end of the experiment the salts are green (the colour of UF_4 ions).

Conversely, uranium is stable in LiF-CaF_2 and can be used for prior reduction. The fluorinated salts at the end of the experiment are red, indicating the presence of UF_3 ions.

Uranium is stable in LiF-CaF_2, and is oxidized in LiF-NaF. The discriminating factor between the two media is the sodium cation. The instability is probably related to the presence of this cation, which can react with uranium, although neither reaction is thermodynamically favourable at 1073 K: $3NaF + U \leftrightarrow UF_3 + 3Na$ ($\Delta G_r° = 119.426$ kJ) and $4NaF + U \leftrightarrow UF_4 + 4Na$ ($\Delta G_r° = 246.073$ kJ) (pure body data).

The investigation of the mechanism for the second stage of uranium reduction will continue with LiF-CaF_2 under the same conditions as for neodymium.

1.2.1.4 Conclusions and outlook

The two studies have provided additional knowledge of the chemical behaviour the two solutes U and Nd before uranium separation by electrolytic extraction.

The NdF_3 reduction mechanism is a single-step process in which 3 electrons are exchanged. Nd is a highly electronegative element that is reduced near the solvent wall, making an electrochemical study difficult. UF_4 is reduced in two steps during which first 1, then 3 electrons are exchanged. UF_4 is more electropositive than NdF_3, and the solvent does not hinder electrochemical investigation. Prior chemical reduction of UF_4 by U makes it possible to study the reduction of U (step IIc); it is also advantageous during the separation step (in an electrolytic U extraction process, the disproportionation reaction is detrimental to the recovery of pure U metal). The prior reduction step in which the UF_4 bath is reduced to UF_3 was investigated in 2 media. The instability of the metal in LiF-NaF has been demonstrated (oxidation to U(IV) and U(III)). Prior reduction is effective in LiF-CaF_2 and stable massive uranium deposits can be obtained.

Within the context of An-Ln separation, a U-Nd mixture was obtained in the LiF-CaF_2 medium with ($NdF_3 + UF_4 + U$) at 810°C (**Figure 8**). A wide range of potentials was observed between the reduction of NdF_3 and UF_3. The ΔE value of about 450 mV appears high enough to obtain U-Nd separation by selective deposition of uranium on a solid cathode.

The first part of this work was carried out at the LGC (Toulouse) on the feasibility of U-Nd separation; the work showed that separation is possible with satisfactory discrimination. The second portion of the work will be carried out at the CEA's Marcoule

research centre to develop an active experimental cell for Pu-Nd separation, that will initially be used for a fundamental study of the mechanism of PuF_3 reduction.

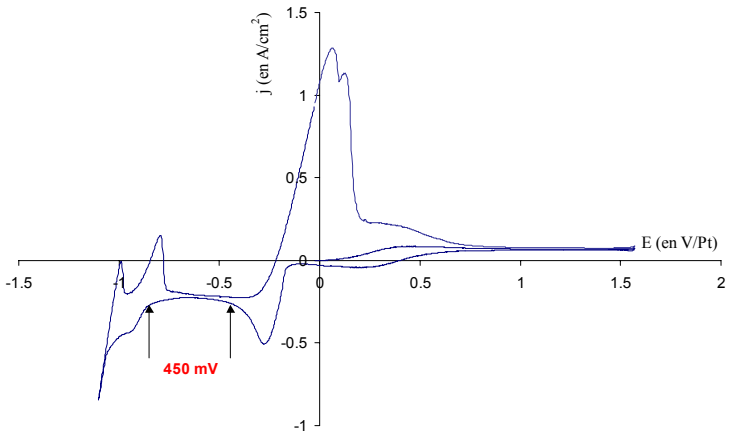

Figure 8. Cyclic voltammogram on Mo in LiF-CaF_2+UF_4 (1.35 wt%) + U + NdF_3 (0.67 wt%) at 810°C, scan rate 0.1 V/s.

1.2.2 NRI contribution (NRI)

The objective of the "Study of electrolytic separation in molten fluoride salt medium" is to assess possibilities for separating the actinides and lanthanides in a molten fluoride salt medium. In order to determine the electrochemical properties important for this assessment, the experimental measurements of selected representatives from each group were realized and measured data were evaluated.

The description of the task accomplishment is divided to the following main parts:

1) preliminary operations (selection and preparation of the melt, designing and assembling of experimental setup, etc.),
2) measurement of electrochemical properties intrinsic to the selected compounds (uranium, thorium, neodymium and gadolinium)
3) evaluation of measured voltammograms and assessment of separation possibilities.

1.2.2.1 Preliminary operations

Eutectic mixtures of fluorides LiF-NaF-KF (FLINAK), LiF-NaF (FLINA), LiF-BeF_2 and later also LiF-CaF_2 were selected as possible carrier melts for the electroseparation studies based on a review of the literature (see section 1.3.1) and thermodynamic calculations. The following properties were considered to be the most important for the appraisal of the melt applicability: low melting point, high solubility of studied compounds, high electrochemical stability and suitable physical properties (electrical conductivity, viscosity etc.). FLINAK (melting point 454°C; see [13] for detailed properties description) was finally selected for the measurements. FLINA was excluded for its high melting point (650°C) and LiF-BeF_2 for its low stability and chemical toxicity. LiF-CaF_2 was proposed at the end of the project for inter-laboratory comparison of our results with CEA measurements using the quasi-reference electrode, but due to technical problems concerning our reference electrode (see below) at needed high working temperature (850°C), no useable measurement was realized with this melt.

The method for raw materials treatment resides in their desiccation under vacuum at step-by-step increasing temperatures (60 – 90 – 150 – 250°C); each step lasts at least 24 hours. A more efficient method was proposed for desiccation of the most hygroscopic compound (KF) by bubbling with fluorine gas. Because of he technically very complicated realization, it was ultimately impossible to apply the method.

Two electrolysers providing electrochemical measurement at high temperatures with the corrosive medium and keeping an inert atmosphere in the electrochemical cell were designed and built. For more detailed description see task 1.3.2.

The experimental setup for electrochemical three-electrode potentiostatic/galvanostatic measurements was assembled in using a high-power Wenking HP 96-20 potentiostat coupled to a Wenking MVS 98 scan generator. The system is controlled by PC, which also enables data acquisition.

The reference electrode was originally designed and produced in our laboratory. It is based on the reference electrode developed in 1970s in ORNL, USA, by H. R. Bronstein and D. L. Manning [14]. The constant electrode potential is provided by the redox couple Ni/Ni^{2+}. Ni^{2+} ions are dissolved in the FLINAK melt in the inner part of the main body made of pyrolytic boron nitride, and nickel is introduced in a form of wire immersed into the melt. Conductive interconnection is provided by very thin (0.1 mm dia.) capillary at the bottom of the electrode body. The reproducibility was successfully proven during brief measurements applying the electrode, but diffusion of Ni^{2+} ions into the measured melt during longer exposure in the melt is very speculative. This fact would disable long-term electrode usage without protecting the capillary by ion-selective diaphragm. The scheme and detail of the final product see **Figure 9**.

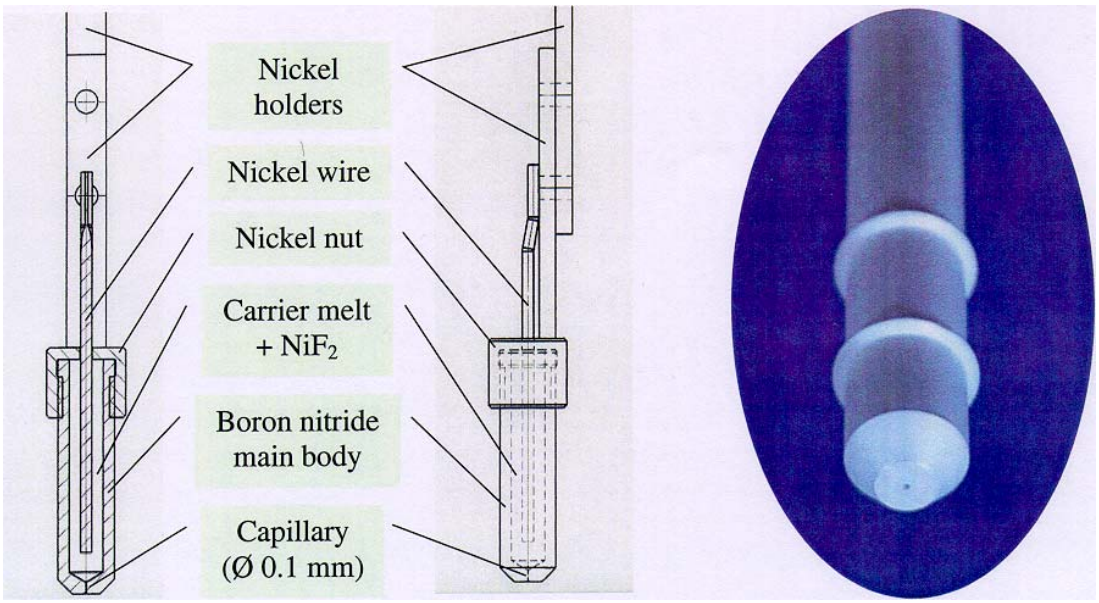

Figure 9. Reference electrode for use in molten fluoride salts:
Part of technical documentation and final product detail

1.2.2.2 Electrochemical measurements

Following systems were experimentally studied using the experimental setup described above (the material of used working electrode is mentioned in brackets):

- pure FLINAK melt (Mo, Pt, glassy carbon, pyrolytic graphite)

- FLINAK – UF_4 (Mo, Pt, glassy carbon, pyrolytic graphite)
- FLINAK – UO_2 (glassy carbon)
- FLINAK – NdF_3 (Mo, Pt)
- FLINAK – GdF_3 (Mo)
- FLINAK – ThF_4 (Mo)

The Linear Potential Sweep Cyclic Voltammetry Method was used as the measurement technique with scan rates from 0.25 mV/s for equilibrium state measurements up to 200 mV/s for dynamic state measurement. A scan rate of 50 mV/s was used in the majority of experiments. The description of the most important results from each measured system follows. All stated potentials are related to the potential corresponding to used reference electrode described above.

The potential range of the FLINAK melt is determined by reduction of alkali metal (probably potassium) in cathodic area at potential of –2.05 V on molybdenum and by oxidation of fluoride ions forming fluorine gas at the anodic limit (the value was not measured). The decomposition of the melt is indicated by sharp current decrease and consequent positive peak during back scan corresponding to stripping of reduced alkali metal. In all cases, the current slope much less steep than the one corresponding to melt decomposition was observed starting app. from potential –1.6 V. This indicates a less intensive reduction process, which can be explained by reduction of alkali metal forming a surface alloy with the working electrode material, while the former reduction as a deposition of metal on metallic layer.

The uranium behaviour was studied separately in cathodic (on Mo an Pt) and anodic (on graphitic materials) areas. Two-step reduction and also two-step oxidation of UF_4 was observed. The particular potential values stated below were assessed from voltammograms measured using molybdenum and pyrolytic graphite working electrodes. A typical voltammogram describing negative potential area of UF_4 in the melt FLINAK is shown in **Figure 10**. The first pair of peaks at potential app. –1.20 V corresponds to the first reduction step from U^{4+} to U^{3+}, the second pair at potential app. –1.75 V to consequential reduction up to uranium metal.

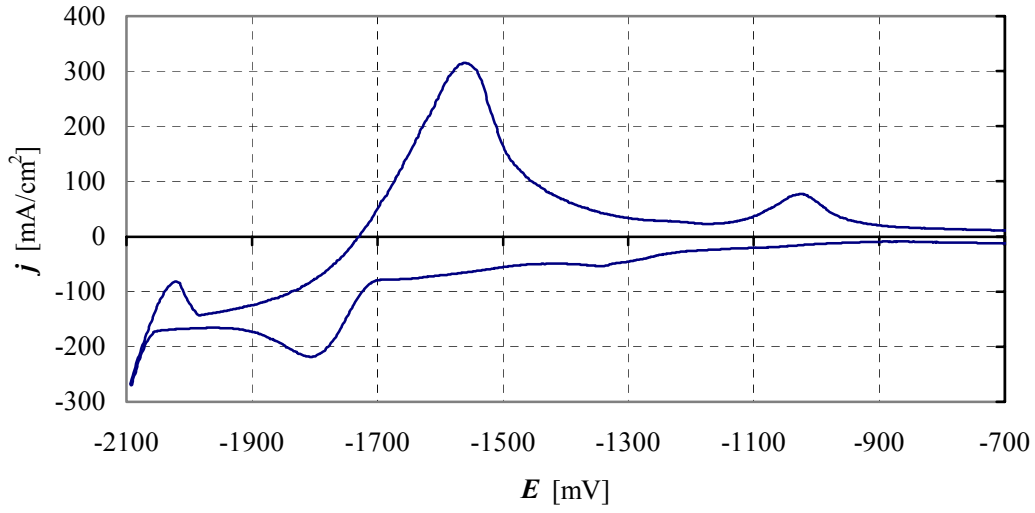

Figure 10. Voltammogram of system FLINAK – UF_4 (1.0 mol%) on Mo working electrode, scan rate 50 mV/s

Similarly, two pairs of peaks were observed in positive potential area, where the measurement was realized separately with UF_4 and UO_2. The first pair at potential app. 0.35 V corresponds probably to oxidation from U^{4+} to U^{5+} ions and it was observed in both studied cases. The second pair at potential app. 1.35 V, which was interpreted like oxidation from U^{5+} to U^{6+} ions, was found only in case of UF_4, whilst in case of UO_2 the formation of oxygen gas preceded and hindered uranium ions further oxidation. Formed compounds containing uranium in higher oxidation states are stable enough to be reduced during back scan. The found fact has to be considered during designing of separation electrolyser, because these compounds will be formed at anode in the course of electrolysis and they would decrease current efficiency of reduction to uranium metal. The electrode areas separation by a diaphragm made from suitable material is recommended.

Neodymium and gadolinium were selected as the representatives of the lanthanides group to study their electrochemical properties and to appraise the separation possibilities between them and uranium. Series of measurements were realized separately with both of them under the same conditions as with uranium. Typical voltammograms of neodymium and gadolinium are shown in **Figure 11**. The first broad pair of peaks was not exactly interpreted, but it was shown to be caused by electrochemical reaction of measured matter. Experiments with different concentrations of NdF_3 ranging from 0.0 to 2.0 mol% were realized, when increasing intensities of peaks were observed depending on increasing concentration. The first reduction step from M^{3+} to M^{2+} (M = Nd, Gd) is the most probable explanation of the fact, but it was neither confirmed nor confuted by calculations due to lack of thermodynamic data.

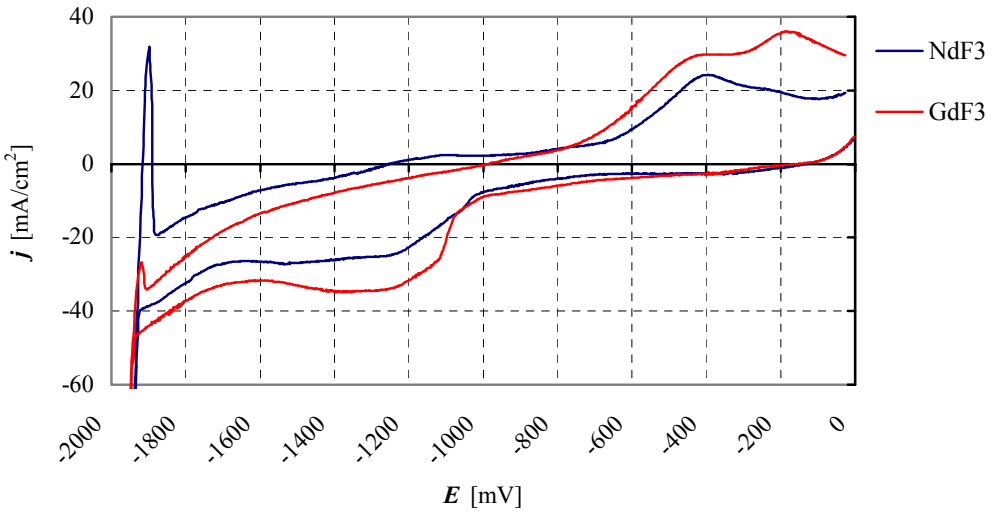

Figure 11. Voltammograms of FLINAK-NdF_3 (blue line) and FLINAK-GdF_3 (red line) systems on Mo working electrode, scan rate 50 mV/s

According to the literature study, two-step reduction of Nd^{3+} ions on molybdenum cathode was reported in [15], while direct reduction to neodymium metal takes place on majority of another cathode materials. e.g. nickel and tungsten [16]. Next considered interpretations deals with partial reduction of Nd^{3+} content up to metal from low-concentrated coordination compound or with formation of an alloy with the electrode material, which could shift the deposition potential to more positive values than theoretically calculated ones.

The reduction to metal was not observed in both studied cases in the melt FLINAK, because it is hindered by the melt decomposition. The found fact corresponds to the

expectations evaluated from thermodynamic calculations. The further studies in more stable melt LiF-CaF_2 were proposed to determine exact deposition potentials, but the measurement has not been finished, because used reference electrode was found unstable at respective working temperature already during the blank experiment.

The last additional measurement was appointed to the study of electrochemical behaviour of thorium in the melt FLINAK, even if it has not been originally planned. The conditions were kept the same again as in case of previous measurements to be able to compare reached results. Thorium was added in a form of ThF_4, which was prepared in laboratory by ThO_2 hydrofluorination and analysed by XRD method. For the measured voltammogram on molybdenum working electrode see **Figure 12**.

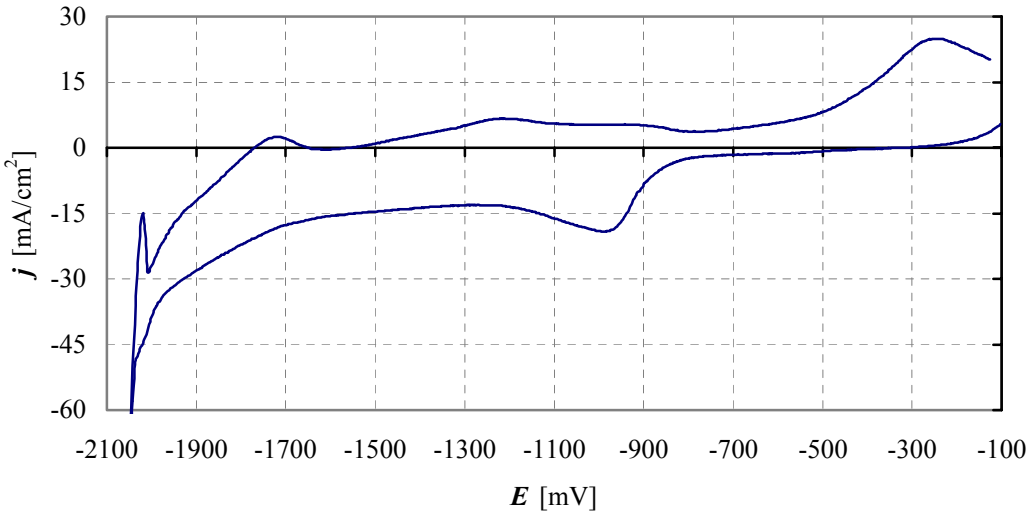

Figure 12. Voltammogram of FLINAK-ThF_4 system (1.0 mol%) on Mo working electrode, scan rate 50 mV/s

The voltammogram consists of the following characteristic features: the pair of peaks at potential app. –0.65 V, the change in current slope very close to the decomposition potential of the melt and a very low-intensity positive peak following stripping of alkali metal during back scan. The first pair can be explained again as a partial reduction, whilst the reduction up to thorium metal takes place at almost the same potential as decomposition of the melt starts and thus it is partially hindered by this action. The results are in good agreement with measurement realized by F.R. Clayton *et al*. in the same melt using different cathodic materials, but comparable reference electrode [17].

1.2.2.3 Evaluation and conclusion

The FLINAK melt could be used as the carrier melt for the electrolytic deposition of matters, whose decomposition potential is not lower than –1.9 V vs. Ni/Ni^{2+} reference electrode. This affirmation is valid assuming the minimal potential difference for the successful separation between two deposited matters is at least 150 mV. According to the observed behaviour of several different working electrode materials, the partial reduction of alkali metal constituting the melt starts already at higher potential, about –1.6 V, when surface alloy alkali metal electrode material is probably formed.

Taking the above stated fact into account, uranium can be removed from the melt by electrodeposition, because the difference between its deposition potential –1.75 V and decomposition potential of the melt is app. 300 mV. However, no uranium metal was

found at the cathode surface after 100 min of electrolysis, even though the current density was stable at the expected value. The problem of uranium deposition resides in the following facts:

- Uranium metal has poor adhesion on the materials of electrodes.
- U^{5+} and U^{6+} ions are produced at the anode, remain in the melt in the form of reducible coordination compounds, and diminish the current efficiency of the reduction process
- Uranium reacts with U^{4+} ions present in the melt, forming U^{3+} ions which result in the dissolution of deposited material

The electrode characterized by a large, structured surface and suitable material (probably with possibility of formation an alloy with uranium) will have to be used for uranium metal deposition. Moreover, it can be strongly recommended to separate electrode areas by a diaphragm to prevent diffusion of anodic products to the cathode.

None of the other studied compounds can be removed from the FLINAK melt by electrodeposition without simultaneous decomposition of the melt. Thorium is reduced to metal at almost the melt decomposition potential, whilst in case of both measured lanthanides this reduction was not detected because it was hindered just by the melt decomposition.

An electrochemical action preceding the reduction up to metal was observed on voltammograms in all studied cases. The expected interpretation exists for uranium, where it corresponds to the first reduction step from U^{4+} to U^{3+} ions. A similar explanation of the observed peaks is assumed for the other cases, but there are more possible interpretations.

The final appraisal concerning the separation possibilities of studied compounds can be realized even if it was impossible to determine all the deposition potentials. The minimal potential difference was counted using the decomposition potential of the melt instead of their exact deposition potentials and resulting value is higher than 150 mV required for satisfactory separation. It is possible to separate uranium from both measured lanthanides and from thorium as well, whilst the separation possibilities cannot be evaluated for thorium-lanthanide pairs or for mutual separation between lanthanides. According to observed very similar electrochemical behaviour of the lanthanides, the separation between them will be probably impossible, whilst separation between the whole group of lanthanides and thorium seems to be feasible in a molten fluoride salt medium.

1.3 Materials and technology

1.3.1 Material selection

This task focused on selecting and corrosion testing of construction and auxiliary materials suitable for use in a device in contact with a molten fluoride salt medium. The materials should be sufficiently resistant at high temperatures in very corrosive environment of molten fluorides. The research also included the materials tested during the studies dealing with the electroseparation processes.

1.3.1.1 Experimental setup

The corrosion studies were carried out in the experimental setup depicted in **Figure 13**. It consists of a nickel vessel and a structural steel flange in which a sample holder, a thermocouple probe, an argon inlet and an outlet are built in. The flange with a system of

PTFE cones enables gastight positioning of the holder. The whole vessel is placed in a resistance oven with heating up to 1000°C.

The crucible with the molten salt is placed at the bottom of the vessel and the sample is dipped and raised by moving the holder.

The carrier melt should provide mainly the following important properties:

- low melting point
- high solubility of fuel components
- sufficient irradiation resistance
- suitable physical properties.

The mixtures of LiF-NaF and LiF-NaF-KF were selected according to the literature study and thermodynamic calculations. In connection with the electroseparation studies using the ternary eutectic mixture of LiF, NaF and KF (acronym FLINAK), all the investigated materials were examined in this molten salt under identical conditions: at a temperature of 530°C in inert atmosphere of highly pure argon (99.998 wt%).

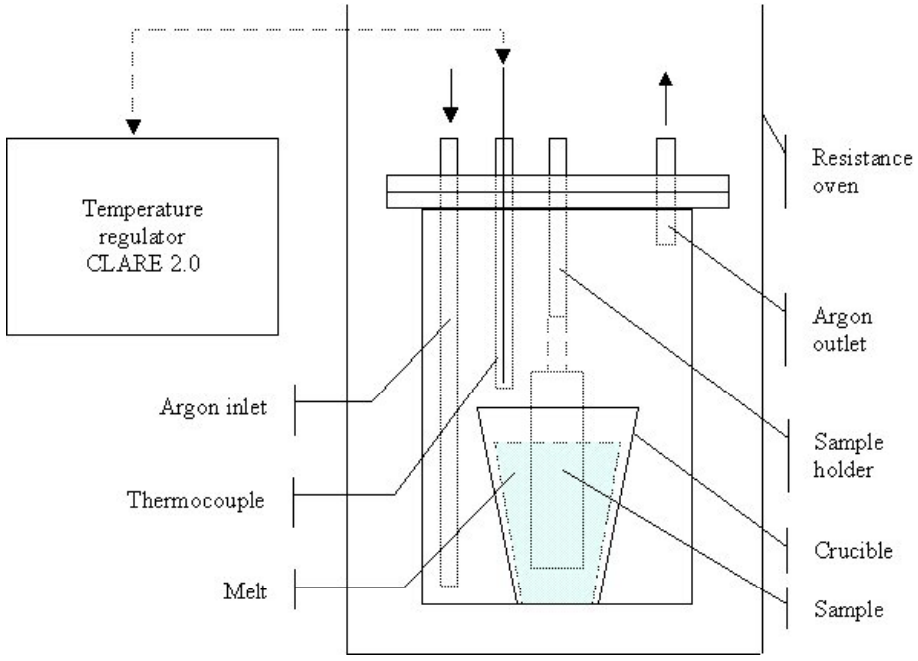

Figure 13. Scheme of experimental setup for stationary corrosion tests

1.3.1.2 Metal construction materials

As a starting point, a literature study dealing with suitable and commercially available constructional materials for molten fluoride salts and with appropriate experimental methods for evaluation of corrosion test results was realized in cooperation with the Department of Metals and Corrosion Engineering of the Institute of Chemical Technology in Prague.

The following recommendations have arisen from the literature study:

- The metallic materials used in a molten fluoride salt environment should have a tendency to passivate their surface.
- The passive film should be as insoluble as possible in the melt.

- During the exposure of metals in the melts, it is necessary to restrict the access of substances containing oxygen to the minimum.
- Temperature of bath and temperature gradient should be as low as possible to lower the diffusional flow of ions to the melt and solubility of the possible passive film.
- The content of chromium and iron in the composition of alloys should be as low as possible.
- Mechanical properties should depend minimally on temperature.

With regard to the literature study, the mid-term stationary corrosion studies focused on testing of the materials with a high percentage of nickel: pure nickel, Hastelloy C-276, MONICR and Inconel 718. The list of samples is stated in **Table III** together with their chemical composition and with the time of their exposure in the melt.

Table III. Chemical composition of acquired constructional materials and time of their exposure

Material	Chemical composition (wt%)									Total exposure time (h)
	Ni	Mo	Cr	Fe	W	Mn	Al	Ti	Nb	
Nickel sheet	100	-	-	-	-	-	-	-	-	511
Hastelloy C-276 sheet & welded sheet	55.60	17.50	14.88	6.30	5.01	0.41	0.31	-	-	1100
MONICR sheet	76.24	15.50	6.00	2.00	-	-	0.10	0.10	-	265
Inconel 718 sheet	54.35	3.09	18.32	17.71	-	-	0.52	0.92	5.08	1100

The samples of the procured materials (together with nickel metal from our own sources) were prepared by abrading and buffing and their structure was documented both before and after testing by the following metallographic evaluation methods:

- Optical light microscopy (Epiphot 300, camera DVC, analyser Lucia G) to evaluate the material microstructure and measure the grain size.
- RTG microanalysis (RTG scanner Epson Perfection 124OU) for semi-quantitative analysis of chemical composition.

The weight and size changes of the samples were monitored as well. The changes in weight can be caused also by increasing of mass due to the formation of corrosive products.

1.3.1.2.1 Results and discussion

The microstructure of all tested materials after exposure was identical with the incipient state and no changes in morphology or in grain size were observed.

As concerns nickel, globular particles appeared at its grain interface after 100 hours of exposure. These particles grew with the exposure time, but the depth of this attack did not increase: it was detected to a maximal depth of 50 μm. After a longer exposure time, inter-crystalline corrosion began and it could progressively cause the surface grains to detach.

Non-uniform attack was observed on Hastelloy C-276. Inter-crystalline corrosion increasing with the exposure time was detected on all the samples. The depth of the attack was about 100 μm for exposure time 1100 hours. After 550 hours of exposure, the surface of the samples was covered by continuous 4 μm thick corrosive layer with high chromium content. This layer partially dissolved during longer exposure and became discontinuous. No measurable differences were noticed between plain metal sheets and welded parts.

Although MONICR alloy was originally developed for LiF-BeF_2 mixtures, it was tested also in the FLINAK melt. The structure of this alloy consists of large and small grains. Corrosion selectively attacked the small grains and caused falling out of small grain chains and consecutively also falling out of the large grains after longer exposure. This alloy is therefore unsuitable for use in the FLINAK melt.

In case of Inconel 718 alloy, its surface exposed to FLINAK was not markedly attacked after 1100 hours. This material seems to be chemically resistant.

1.3.1.2.2 Conclusion

Pure nickel and alloys Hastelloy C-276, MONICR and Inconel 718 were studied by mid-term stationary corrosion tests with following results. Nickel, Hastelloy C-276 and MONICR are not suitable for the FLINAK fluoride melt. Inconel 718 seems to be intact by this melt.

1.3.1.3 Other electrolyser constituent materials

The behaviour of the materials constituting the devices produced for electrochemical studies was tested in operational conditions during measurements. These include both metal construction materials (electrolyser vessels, electrode materials) and non-metallic (gaskets) and ceramic material necessary for the construction of non-conducting parts of the reference electrode for molten fluoride salts (see 1.2.2).

1.3.1.3.1 Results and discussion

Concerning construction materials, pure nickel proved to be suitable for electrolyser vessels and electrode holders. PTFE appeared to be suitable for gaskets zones where the temperature does not exceed 200°C. Copper was found to be stable in the presence of an inert atmosphere at working temperature and is recommended for electrical contacts between electrodes and their holders to lower their contact resistance.

Materials for working electrode and for crucibles serving as auxiliary electrode were examined to determine their electrochemical stability and limitations in use. The influence of working electrode material on the measured system in negative potential area was also studied. It seems to be rather significant, because it can shift the redox potentials of all the elements present (including elements constituting the melt) to more positive values by formation of alloys with electrode material; for example, the reaction of liquid sodium with platinum at temperatures up 400°C was confirmed by phase diagrams. Knowledge of relevant phase diagrams is important for proper interpretation of measured data.

Molybdenum, platinum and graphitic materials (pyrolytic graphite and glassy carbon) were tested over the whole potential range by linear sweep cyclic voltammetry. Molybdenum starts to dissolve at a potential of ~ +500 mV and platinum at ~ +1 500 mV vs. Ni/Ni^{2+} reference electrode (see 1.2.2), which precludes their use for anodes in electro-deposition processes. Anodic dissolution causes degradation of the electrode material. In the case of platinum, the formation of coordination compounds is possible due to chemical

reactions of platinum ions with uranium, potassium and fluorine ions. These reactions can diminish the current efficiency of the electrodeposition.

Graphitic materials were found to be electrochemically inactive over the whole investigated potential range and they can be used both as cathode and anode. Mechanical stability problems occurred with pyrolytic graphite: the melt was soaked up into the flaky structure of the material. Glassy carbon has satisfactory mechanical properties and was used as the anode crucible for electrochemical measurements. A graphite crucible was used for melting of the fluoride salt, but its mechanical properties appeared to be unsuitable due to chemical dissolution of the bonding agent into the melt, which passed through the crucible after several hours of heating. Thus, no electrochemical measurements were performed with the graphite crucible.

O^{2-} ions can be oxidized at the specific potential to oxygen gas on the anode. When graphitic material is used as the anode, oxygen can react with electrode material at the working temperature, forming carbon monoxide or dioxide. Oxygen ions can be presented in the melt as an impurity (e.g. like traces of chemically bonded water presented in the melt in spite of thorough desiccation) or can be adsorbed at the electrode surface in a form of carbonates.

Due to the results of electrochemical measurements with uranium (see 1.2.2), a sample of nickel foam was tested as possible electrode zone separator for the electrodeposition processes. The sample was supplied by Inco Ltd. (UK). Unfortunately, the material near the phase interface was the most affected area and its mechanical properties were modified. Another material considered to be suitable is sintered corundum, but it could chemically contaminate the melt by aluminium and thus influence measured signals. Otherwise, its electrical non-conductivity represents its main advantage.

Concerning non-metallic materials for construction of the reference electrode body, hot-pressed boron nitride, silica glass and sintered Al_2O_3 were selected and tested in the FLINAK melt. Silica glass and Al_2O_3 were strongly damaged after only 50 h of exposure. Boron nitride appeared to be a suitable material and was used for the construction.

1.3.1.3.2 Conclusion

The following materials proved their suitability as device construction materials for electroseparation studies in the molten salt FLINAK. Nickel was selected for electrolyser vessels and PTFE for the gaskets. Electrochemical measurements showed that molybdenum, pyrolytic graphite and glassy carbon are suitable as cathodic materials and glassy carbon as anodic material. Hot-pressed boron nitride proved to be the suitable non-conductive ceramic material for the reference electrode body.

1.3.2 Construction of electrolyser

Within the PYROREP project, two electrolyser prototypes for studies of electroseparation of the lanthanides and actinides from the molten fluoride melt media were designed, built and successfully tested during electrochemical experiments.

1.3.2.1 Two-electrode electrolyser

The first prototype was produced in October 2000 and it served for preliminary two-electrode electrolytic experiments. **Figure 14** shows a schematic and a photo of the electrolyser in the laboratory environment, with a description in **Table IV**.

Figure 14. The prototype electrolyser:
3D drawing and final product placed in the resistance oven

Table IV. Description of the prototype of two-electrode electrolyser

Material	Vessel	Pure nickel metal
	Auxiliary parts	Pure nickel metal: internal parts; copper: contacts; construction steel: flanges
	Gaskets	PTFE
Inert atmosphere		Yes
Heating		No, another source is needed
Electrodes		2
Gaskets for gastight movement of electrode holders		System of PTFE cones pressed by flange
Max. crucible diameter		120 mm

This device consists of a nickel vessel and internals – an electrode holder, an argon inlet and outlet and a thermocouple probe built into a structural steel flange. Electrical contacts are made of copper and gaskets from PTFE. The flange and pressed PTFE cone system enables gastight vertical and rotational motion of the electrode holder.

The vessel can be used under inert atmosphere or vacuum. It is placed in a precisely regulated resistance oven capable of reaching a temperature of 1000°C and the temperature inside the vessel is measured simultaneously by the thermocouple.

Preliminary two-electrode measurements with stabilized voltage source (without reference electrode) were carried out in this setup under pure argon atmosphere with 10 kPa overpressure. These preliminary experiments concerned the electrochemical behaviour of uranium in fluoride the melts, and focused on testing the first electrolyser prototype under working conditions from the standpoint of material stability and verifying the electrolysis cell design.

All the materials and the design of the main vessel appeared to be satisfactory for work in aggressive environment of molten fluoride salts at high temperatures if inert atmosphere was present and also internal gastightness was verified even during electrode movements.

This two-electrode cell can be used in electrolytic processes in which the cell should be as simple as possible, electrochemical properties are known and it is not necessary to use any reference electrode.

1.3.2.2 Three-electrode electrorefiner

Based on the experiences acquired from the work with the first electrolyser, the new modified prototype was designed and produced in cooperation with the Clasic company, special Czech producer of heating techniques, in January 2001. **Figure 15** shows a drawing and photo, and the unit is described in **Table V**.

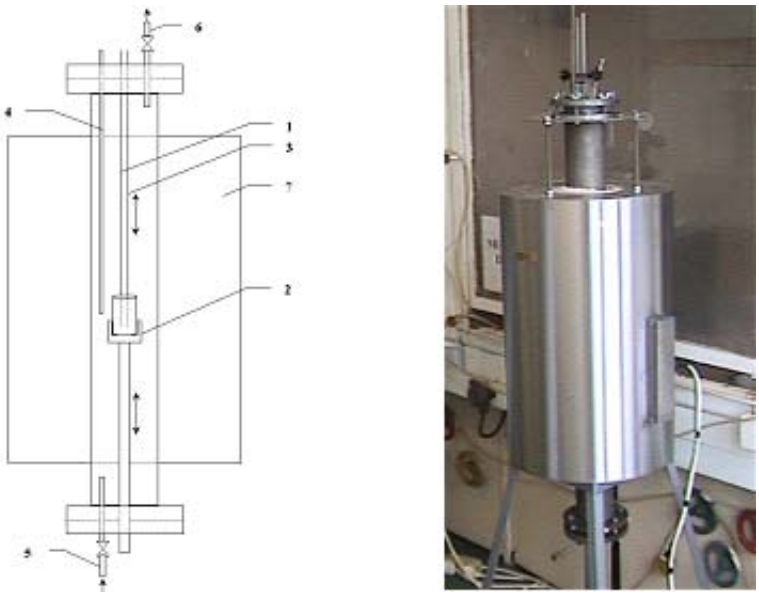

Figure 15. Prototype electrorefiner: Cross-sectional drawing and final product.
Key: 1 – Cathode holder, 2 – Crucible (anode) holder, 3 – Reference electrode holder, 4 – Thermocouple, 5,6 – Valve for inert inlet/outlet, 7 – Heater (resistance oven)

Table V. Description of the prototype of three-electrode electrorefiner

Material	Vessel	Pure nickel metal
	Auxiliary parts	Pure nickel metal: internal parts; copper: contacts; construction steel/nickel: flanges
	Gaskets	PTFE
Inert atmosphere		Yes
Heating		Yes, vertical resistance oven up to 1000°C
Electrodes		3
Gaskets for gastight movement of electrode holders		Combination of PTFE and special gaskets from automobile engine pistons
Max. diameter of crucible		80 mm

This laboratory electrolyser is inserted in a vertical resistance oven with a homogenous temperature field up to 1000°C. The construction also makes it possible to keep an inert atmosphere or vacuum in the cell, gastight vertical and rotational motion of the working and reference electrodes. In case of future experimental requirements the whole cell is interchangeable. The cell and gasket materials are identical with those of the first electrolyser: pure nickel and PTFE, respectively.

Important design changes in comparison with the first electrolyser include the possibility of operating the main vessel both from upper and lower part; a reference electrode holder has been added and the system of electrode holding and fitting has been improved – it is made from special original arrangement inspired by the system of automobile pistons gaskets.

The second prototype was successfully tested by electrochemical measurements. Several important facts arose from them for further modification of electrochemical cell design. The main reason is lowering of working electrode current efficiency by the possible formation of stable electro-active species at the auxiliary electrode (anode). Due to this reason the electrolytic cell should be separated by chemically resistant porous diaphragm.

1.3.2.3 Conclusion

Two functional prototypes have been built and are ready for use in the electrochemical processes, both of them allow working under inert atmosphere or vacuum. The new advanced electrolyser is designed applying the experiences obtained by electrochemical measurements realized in the existing prototypes. On the base of the results, separation of the electrochemical cell by diaphragm will be realized, especially for the separation of uranium from the molten fluoride melt medium.

1.4 Conclusions of fluoride media studies

Two separation concepts were investigated in fluoride media: selective electrodeposition and reductive extraction. In both cases the objective was to separate the actinides collectively from the fission products.

- Selective electrolytic extraction of the actinides

The CEA and NRI worked on similar concepts in different salt media:

- The CEA study was limited to the basic mechanisms of cathodic reduction of UF_4, and NdF_3 in LiF-NaF and LiF-CaF_2.
- NRI conducted similar fundamental research on the reduction of NdF_3, UF_4 and ThF_4 in a fluoride salt mixture of LiF, NaF and KF known as FLiNaK, and in LiF-CaF_2.

The cyclic voltammograms obtained by both laboratories clearly show that U/Nd separation is thermodynamically possible, and thorium measurements in FLiNaK indicate that U/Th separation should also be possible. However, the results of these studies are inconclusive with regard to the possibility of Th/Nd or Th/Gd separation in FLiNaK.

NRI also performed more technological studies for the selection of suitable materials for the electrodes and for the electrolyser unit, and the development of a reference electrode.

NRI fabricated a reference electrode from the design developed in the 1970s at ORNL to allow measurements in FLiNaK salt: the constant electrode potential is provided by the redox couple Ni/Ni^{2+}. Reproducible results were obtained during brief measurements by applying the electrode, but diffusion of Ni^{2+} ions into the melt during longer exposures

tends to affect the results. This fact would prevent extended electrode usage unless the capillary is protected by an ion-selective diaphragm.

Corrosion studies were also carried out to select suitable construction materials for equipment used in molten LiF-NaF and LiF-NaF-KF salt media. Several high-nickel materials (pure nickel, Hastelloy C-276, MoNiCr and Inconel 718) were submitted to corrosion tests at 530°C in 99.998% argon atmosphere under steady-state conditions. The results showed that only Inconel 718 provided satisfactory resistance under these conditions. Although nickel raises long-term intercrystalline corrosion problems, it was nevertheless satisfactorily used for the experimental electrolysis vessels.

Other electrolysis cell component materials were also tested.

- Reductive extraction of the actinides by aluminium in LiF/AlF_3

The CEA also worked on group separation of the actinides from fission products by reductive salt/metal extraction.

The results obtained with plutonium, americium cerium and samarium in the (LiF-AlF_3)/(Al-Cu) medium revealed the potential of this system for separating the actinides from the lanthanides. More exactly, with a salt composition corresponding to the basic eutectic (LiF-AlF_3, 85-15 mol%), up to 99% of the plutonium and americium could be recovered in a single stage, with cerium and samarium separation factors exceeding 250. The experiments show that the distribution coefficients of these elements vary inversely with the AlF_3 concentration.

2 Chloride media

2.1 Conversion to halide form

2.1.1 Introduction

The objective of this task is to determine the viability of direct chlorination of oxide fuel, as it could simplify fuel treatment by pyrochemical processes.

The starting material considered is a chemical analogue of UO_2-type fuel (simfuel), provided by AECL, which simulates a fuel of 50 $MWd \cdot kgU^{-1}$ burnup. Based on RIAR experience with oxide fuels the aim of the present study is to demonstrate experimentally (at laboratory scale) that UO_2 type fuels could be directly dissolved in molten salt and to provide the optimum conditions and chlorinating mechanisms.

The methodology proposed in this study is based on the construction and comparison of the E-pO^{2-} diagrams for uranium and rare-earth oxide compounds and the chlorinating gaseous mixtures. It enables us to propose the main lines for the pyrochemical separation process. Experimental solubilization tests are then performed using pure HCl and Cl_2 gases and the chlorinating Cl_2(g)+C(s) mixture. Although this chapter focuses on the solubilization studies, several tools and basic data reported in section 2.2.1 and Deliverable 3 have been used.

A comparative study of dissolution kinetic obtained by the chlorinating mixtures considered is also provided

Several variables, including particle size and surface area, sample size and temperature, influenced the kinetics of the solubilization processes. These variables were studied for REs and uranium, allowing us to propose the best solubilization conditions. The experimental procedure and the study performed are described in detail in Deliverable 19 [18-27].

2.1.2 Main Results

2.1.2.1 Solubilization of Simfuel and UO_2 La, Ce, Pr, Nd, Y and Mo oxides in the eutectic LiCl-KCl mixture at 450ºC.

The potential-acidity (E-pO^{2-}) diagram for the species was established from the values of the solubility products of the compounds, the equilibrium potentials of the different redox couples, some published thermochemical data and the activity coefficients. The diagrams summarize the main oxo-acidity and redox properties of the elements in the molten salt mixture. Comparing the E-pO^{2-} diagram of RE oxide compounds and U oxides with the E-pO^{2-} diagrams of chlorinating mixtures provided the chlorinating conditions summarized in **Table VI** and **Table VII**. Thermodynamic predictions were experimentally verified by solubilization tests with the selected chlorinating mixtures. Chlorinating reaction rates were calculated from the experiments. The effect of temperature, surface area and therefore particle size and sample size on reaction kinetics was determined.

Table VI. Chlorinating conditions of RE-O compounds

Mixture	LaOCl La_2O_3	CeOCl Ce_xO_y	NdOCl Nd_2O_3	PrOCl Pr_xO_y	Y_2O_3
Cl_2+O_2	*	–	*	–	+
Cl_2+C	+	+	+	+	+
Cl_2+CO	+	+	+	+	+
$HCl+H_2O$	*	*	*	*	+
$HCl+H_2O+H_2$	*	*	*	*	+
$HCl+CO+H_2$	*	*	*	*	+

(+) At every gas pressure; (*) At most gas pressures; (–) Under very restricted conditions

Table VII. Chlorinating conditions of UO_2

Mixture	Cl_2+O_2	Cl_2+C	Cl_2+CO	$HCl+H_2O$	$HCl+H_2O+H_2$	$HCl+CO+H_2$
UO_2	+	+	+	*	*	*

(+) At every gas pressure; (*) At most gas pressures; (–) Under very restricted conditions

Solubility tests confirmed the chlorinating predictions of REs and UO_2. In the case of REs, higher kinetics are obtained with HCl as the chlorinating agent. Solubilization of UO_2 is faster by carbochlorination than by HCl gas mixture. Although we do not have a clear explanation of this phenomenon, it could be due to differences between a commercial solid and a sintered solid. Solubilization conditions tested on UO_2 were used with simfuel. As expected simfuel exhibited behaviour similar to that of unirradiated UO_2. (**Figure 16**).

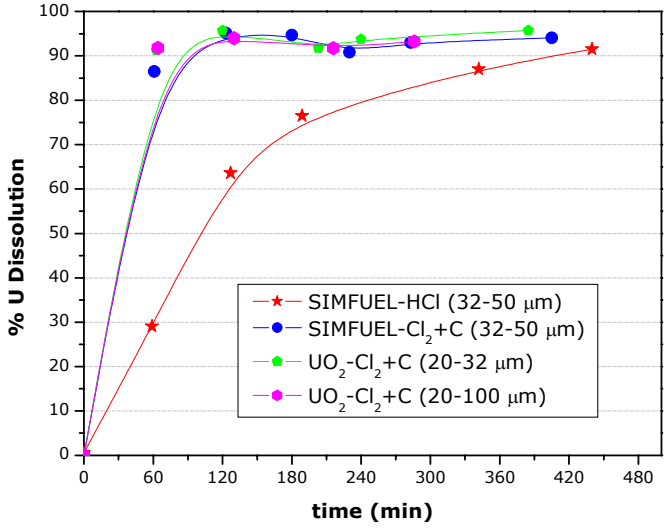

Figure 16. Solubilization of simfuel and UO_2 (gas mixtures HCl and Cl_2+C)

RE reaction rates were calculated from experiments performed with samples of an individual RE oxide and from experiments carried out with a mixture of RE oxides. Amount of individual samples considered and amount of the mixture was similar and less than 1 g in all the experiments.

The RE chlorination rates observed are shown in **Table VIII** to **Table X**.

Table VIII. Chlorination rates (× 10^5 mol·kg^{-1}s^{-1}) of RE oxides with HCl (g)

m range (g)	CeO_2	La_2O_3	Y_2O_3	Nd_2O_3	Pr_6O_{11}
0.48–0.80	3.1	3.6	3.4	1.2	0.6
0.16–0.26	–	0.9	0.9	0.7	0.3
0.09–0.14	0.28	0.25	0.21	0.14	0.07
≈ 0.05	0.12	0.12	0.11	0.06	0.03

Table IX. Chlorination rates of RE oxides with Cl_2

	Mass (g)	Rate (× 10^5 mol·kg^{-1}s^{-1})
Nd_2O_3	0.0.6670	0.2
Y_2O_3	0.1946	0.4

Table X. Chlorination rates of RE oxides with Cl_2+C

	Mass (g)	Rate (× 10^5 mol·kg^{-1}s^{-1})
La_2O_3	0.6008 (700ºC)	0.5
Nd_2O_3	0.9063 (450ºC) 0.9063 (700ºC)	0.3 0.6
Y_2O_3	0.3555 (700ºC) 0.1827 (700ºC)	0.9 0.9

Reaction rates obtained in experiments with simfuel are shown in **Table XI**, together with the influence of particle size on the kinetics.

Table XI. Simfuel dissolution rates

Sample size (g)	Particle size (μm)	T (ºC)	Chlorinating gas	Dissolution rate (mol·kg^{-1}s^{-1})
0.1798	32-50	550	HCl	1.0×10^{-8}
0.1682	32-50	550	Cl_2+C	2.6×10^{-8}
0.1823	100-315	550	HCl*	3.9×10^{-9}
0.1782	100-315	550	Cl_2+C*	1.12×10^{-8}
0.3664	100-315	550	Cl_2 + C**	1.9×10^{-8}
0.1794	100-315	550	Cl_2*	1.4×10^{-8}
0.1849	315-500	550	Cl_2 + C	1.2×10^{-8}

* control of gas stream: Q = 2.5 L/h
** control of gas stream Q = 3 L/h

Experiments performed with UO_2 or simfuel pellets provided low dissolution efficiencies (10–14%) due to the low surface area of a sintered material. Nevertheless, pellets results should not be extrapolated to irradiated materials as surface area of irradiated fuel is estimated to be about 6 times higher than unirradiated UO_2.

2.1.3 Conclusions

- After establishing the E-pO^{2-} diagrams of the RE-O and U-O compounds, it is possible to predict the best chlorinating conditions of the oxy-compounds by different chlorinating mixtures based on gaseous HCl and Cl_2.
- Experimental solubilization tests of different rare earth oxy-compounds were performed using HCl(g), Cl_2(g) and the chlorinating mixture Cl_2(g)+C(s), showing different solubilization mechanisms of gaseous HCl and Cl_2 and different diffusion properties in both gases provided lower kinetics with Cl_2(g).
- The dissolution results of REs obtained with the Cl_2+C mixture indicated that increasing the working temperature leads to higher kinetics, due to the increase in the solubilization of Cl_2(g).
- The following rating is based on the estimated dissolution rates of the RE_xO_y compounds with HCl(g):

  $v(CeO_2) \cong v(La_2O_3) \cong v(Y_2O_3) > v(Nd_2O_3) > v(Pr_6O_{11})$
- The RE-O dissolution rates obtained show that an increase in sample size results in higher dissolution rates.
- UO_2 chlorination by HCl(g) and Cl_2+C (graphite tube) provides efficiencies higher than 90%. Higher kinetics are obtained by carbochlorination
- At the highest temperature tested, 550°C, total UO_2 dissolution with HCl requires a longer time than by carbochlorination
- The solubilization behaviour of simfuel is similar to solubilization of UO_2. Therefore, conclusions obtained for UO_2 may extrapolated to simfuel.
- UO_2 and simfuel dissolution showed a slight influence of sample size: the larger the sample, the longer the time required.
- Particle sizes below 500 μm provide dissolution rates in the range of $1–2.5 \times 10^{-8}$ $mol \cdot kg^{-1}s^{-1}$. Direct chlorination of pellets leads to the lowest dissolution rates, as expected in a sintered material.
- Assuming that for spent fuel the average surface area is around 6 times higher than for unirradiated fuel due to irradiation effects on fuel structure (porosity, cracks, grain size growth, etc.), the dissolution rate of irradiated UO_2 could be similar to the obtained by the unirradiated fuel fraction between 100–315 μm (experimental verification of this assumption with spent fuel will be necessary). Then, it is considered that a previous step of decladding and maybe solid preparation should be performed if direct chlorination of oxide type fuel is selected.

2.2 Basic data acquisition

2.2.1 Simfuel

This task focused on determining the electrochemical behaviour and separation factors using a simulated nuclear fuel (simfuel) in a chloride medium: LiCl-KCl with solid and/or liquid cathodes.

In order to maximise the processing rate of the electrorefining step, it is necessary to analyse and predict the kinetic behaviour of the actinides and rare earth elements in the electrolytic cell and the thermodynamic properties in the selected molten media. Therefore, this work package focused on the study of the electrochemical behaviour of uranium and rare earth elements, which are the most difficult fission products to separate from actinides due to their similar chemical properties in LiCl-KCl. The studies performed are described in detail in Technical report D3 [25-57].

Studies were carried out to determine thermodynamic properties and to elucidate RE electrochemical deposition mechanisms with solid (W and Mo) and liquid (Cd and Bi) cathodes. In addition, a study of the electrochemical behaviour of REs into aluminium was initiated.

Uranium electrochemical studies were performed with uranium solutions obtained from UO_2 or simfuel as starting material, as it does not influence the electrochemical behaviour of uranium. This study used a solid cathode (W).

In general the experimental steps followed in this WP are:

- thermodynamic properties:
- stable oxidation states
- standard potentials values of the different electrochemical systems in LiCl-KCl
- activity coefficient in the eutectic LiCl-KCl.
- Gibbs energy, enthalpies and entropies of formation.
- metal electrodeposition studies
- solid electrodes (W, Mo):
- electro-crystallization studies.
- kinetic parameters of reaction steps (k_0, α)
- activation energy for the diffusion and diffusion coefficients.
- liquid electrodes (Cd or Bi pools and CdTFE) and preliminary studies on Al electrode
- ΔG^o_f of intermetallic compounds
- standard potential values in the metal phases: E^o RE(III)/RE-Cd and RE(III)/RE-Bi,
- estimation of the activity coefficients of the RE in the metal phase γ (RE in Cd) γ (RE in Bi).
- temperature effect ΔH and ΔS of mixing.

2.2.1.1 UO_2

2.2.1.1.1 Introduction

The aim of this work is to determine basic thermodynamic data of uranium, such as the standard reduction potential of UCl_3, activity coefficient, diffusion coefficients, Gibbs energy of formation of UCl_3 in the eutectic LiCl-KCl, in order to design a separation process. The temperature range considered was from 450º to 550ºC. Electro-crystallization of U at W substrates was investigated.

2.2.1.1.2 Main results

- In LiCl-KCl several stable oxidation states of uranium were observed: UO_2^{2+}, UO_2^{+}, U^{4+}, U^{3+} and U^0.
- The U(IV)/U(III) reduction reaction proceeds through a reversible soluble-soluble reaction with the exchange of one electron.
- The U(III)/U(0) reduction reaction proceeds through a quasi-reversible soluble-insoluble reaction with the exchange of three electrons.
- The electro-crystallization of the uranium metal at the electrode surface is the controlling step of the reaction. The analysis of the I-t transients shows a progressive nucleation mode.
- The diffusion coefficient was determined for the 450-550°C temperature range and the Arrhenius law was confirmed.
- From the Gibbs energy of formation of UCl_3 the activity coefficient was calculated indicating complexation of the uranium trichloride ion into the molten LiCl-KCl. The enthalpy and entropy of UCl3 formation were determined from the variation of ΔG_f^o with the temperature.

2.2.1.2 Fission products

2.2.1.2.1 Main results

- Electrochemical properties of REs were studied using tungsten and molybdenum wires as working electrodes in the eutectic LiCl-KCl at temperatures between 673 and 823 K.
- Stable oxidation states of La, Ce, Pr and Y were found to be (III) and (0). In the case of neodymium, oxidation state (II) was also found to exist. The stability of the rare earth metals was demonstrated, and their solubility in the molten chloride containing RE(III) ions at low concentration was considered to be negligible. In the case of cerium and praseodymium, voltammetry curves did not show any anodic signals apart from the anodic limit of the melts (chlorine evolution), indicating the oxidizing behaviour of Ce(IV) and Pr(IV) species, which react with the chlorides of the melt according to:

  $$2\ Cl^- + 2\ Ce(IV) \text{ or } Pr(IV) \leftrightarrow Cl_2\ (g) + 2\ Ce(III) \text{ or } Pr(III)$$

- The standard potentials of the different RE(III)/Re(0) redox couples were determined by potentiometry measuring the emf between the Ag|AgCl reference and a RE electrode in solutions containing different RE(III) concentrations. Extrapolation of measured values of E to $x_{RECl_3} = 1$ or $C_{RECl_3} = 1$ mol·kg^{-1} permits the calculation of E^o_x or E^0_m respectively.

- In the case of neodymium, the reaction:

  $2\ Nd(III) + Nd(0) \leftrightarrow 3\ Nd(II)$

  prevents potentiometric determination of the standard potential of the Nd(III)/Nd(0) couple. The E^o of Nd(III)/Nd(II) and Nd(II)/Nd(0) systems were determined by different electrochemical techniques (i.e. cyclic voltammetry and convolution analysis) by means of the appropriate equations.
- The variation of the standard potentials with the temperature was also studied, yielding a shift toward more positive values when increasing the working temperature.
- Knowing the E^o of the different RE(III)/RE(0) systems, it is possible to determine the Gibbs energy of formation of $RECl_3$, and the activity coefficients of $RECl_3$ compounds can be calculated by comparison with the pure compounds. The results showed that the rare earth cations are solvated by the chlorides:

  $RE(III) + 6\ Cl^- \leftrightarrow RECl_6^{3-}$
- Moreover, activity coefficients of rare earth chlorides have been calculated, showing that the most polarizable cation Y(III) possesses the lowest activity coefficient, i.e. it is the rare earth cation most solvated by the molten chlorides.
- Voltammetric and chronoamperometric techniques showed that nucleation and growth of the metallic lanthanum and yttrium deposit play an important role in the overall electrodeposition process. No UPD of metallic RE on tungsten or Mo substrates was found. Analysis of the transient curves (both the rising leg and the complete curve according to a non-dimensional model) showed that the initial stages of electrochemical deposition of lanthanum and yttrium on a tungsten electrode can be explained in terms of a model involving instantaneous nucleation (i.e. all the nuclei are formed "immediately" after applying the potential step) with three-dimensional growth of the nuclei. Identical results were found when varying the working temperature from 673 up to 823 K.
- However in the case of cerium, praseodymium and neodymium we found that it is the charge transfer step rather than nucleation and crystal growth which controls the electrodeposition process. The values of the charge transfer constant, k^o, calculated by logarithmic analysis of the convoluted voltammetric curves, showed a quasi-reversible behaviour of the systems.
- Moreover, the diffusion coefficients of the RE(III) ions were obtained by different electrochemical techniques (i.e. convolution and chronopotentiometry) and showed a temperature dependence according to the Arrhenius law.
- The electrode reaction of the RE(III)/RE(0) couples at liquid Cd or Bi electrodes was investigated using the corresponding metal pool and film electrodes. The redox potentials of the RE(III)/RE couples at both liquid electrodes were observed at less cathodic potentials than those at a solid W electrode. This potential shift was interpreted as a lowering of activity of the deposited metal in the metal (Cd or Bi) phase due to the stable chemical interaction between the RE and M (M=Cd or Bi).
- Cyclic voltammetric experiments carried out using a fresh Cd or Bi film electrode, evidenced the formation of different intermetallic compounds.
- The equilibrium potentials versus RE(III)/RE for the formation of these intermetallic compounds were estimated by open circuit chronopotentiometry in a molten LiCl-

$KCl\text{-}RECl_3$ system at 723 K, making it possible to estimate the activities and the relative molar Gibbs energies of RE in the intermetallics, as well as the Gibbs energies of formation of the different RE-Cd and RE-Bi alloys.

- The activity coefficients of REs (La, Ce, Pr, Nd and Y) in liquid cadmium and bismuth at temperatures between 693 and 823 K were estimated by comparing the standard potential values of the electrochemical systems RE(III)/Re in solution with the standard potential values of the electrochemical systems in the Cd or Bi metal phase derived from the voltammetry. Special attention should be given to the surface of the electrode and the RE(III) concentration in solution in order to prevent saturation of the electrode surface.
- The activity coefficients of REs are smaller in Bi than in Cd, and their order in both liquid Cd and Bi is:

$$\gamma_U > \gamma_{Pu} > \gamma_Y > \gamma_{Pr} \cong \gamma_{Ce} \cong \gamma_{La} \cong \gamma_{Nd}$$

- The ratios between the activity coefficients of uranium and REs and plutonium and REs in Bi are smaller than those in Cd.
- The differences between the activity coefficients of Ln and U, Ln and Y and probably Ln and Pu decreased with increasing temperature.
- The partial molar enthalpy of mixing and the partial molar excess entropy of solutes in liquid cadmium was evaluated from the change in the activity coefficients with temperature.
- The partial molar enthalpy of mixing and the partial molar excess entropy, which are useful for estimating the variation in the separation factor with increasing temperature were calculated from the estimated molar excess Gibbs energy of the solute RE. The results indicate that the order of the partial molar enthalpy of mixing in both liquid metals Cd and Bi is:

$$\Delta H^{mix}_U > \Delta H^{mix}_Y > \Delta H^{mix}_{Pu} > \Delta H^{mix}_{La} \cong \Delta H^{mix}_{Pr} \cong \Delta H^{mix}_{Nd} \cong \Delta H^{mix}_{Ce}$$

- The formation of RE-Al alloys was investigated in a molten $LiCl\text{-}KCl\text{-}RECl_3$ system by cyclic voltammetry and chronopotentiometry in open circuit using one Al phase at temperatures between 673 and 823 K.
- EMF measurements for the RE-Al intermetallic compounds in two-phase coexisting states were carried out at several temperatures (673, 693, 723, 773 and 823 K). The activities of RE in the Al phase and the standard Gibbs energies of formation for RE-Al intermetallic compounds were estimated as well as the standard enthalpies and entropies of formation.

2.2.1.3 Conclusions of simfuel studies

The reduction potentials of RE(III)/RE for solid cathodes, liquid cadmium and bismuth cathodes and one Al cathode in comparison with the reduction potential of actinides are summarised in **Figure 17**.

Effective separation of U from transuranium and lanthanide elements will be obtained by solid cathodes (W).

Separation of Pu from lanthanides and Y seems to be easier with aluminium electrodes than with Cd and Bi liquid cathodes.

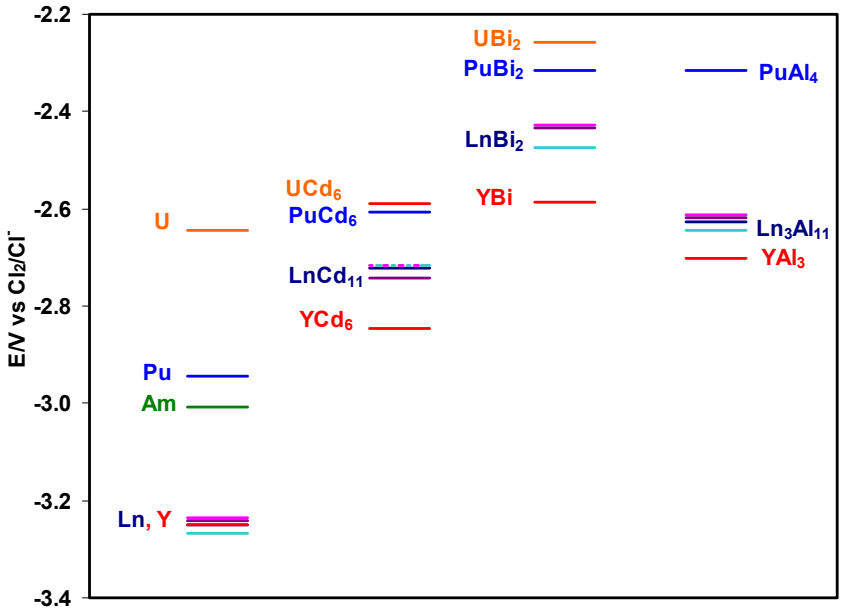

Figure 17. Reduction Potentials of RE(III)/RE and RE(III)/RE in Bi, Cd and Al cathodes. T=723 K, $X_{M\ in\ salt} = X_{M\ in\ Cd} = X_{M\ in\ Bi} = 0.001$; $a_{Pu\ in\ Al} = 3 \times 10^{-13}$; $a_{Ln\ in\ Al} = 1 \times 10^{-13}$; $a_{Y\ in\ Al} = 3 \times 10^{-12}$ (Actinide values are taken from the literature)

2.2.2 Actinides

2.2.2.1 Introduction

Electrorefining in molten LiCl-KCl eutectic is the most common pyrochemical separation process used for nuclear fuels. The actinides are separated from the bulk of fission products by electrotransport in the molten salt electrolyte, i.e. uranium onto a solid cathode and plutonium and minor actinides (MA) into a liquid Cd cathode [58]. Additional systems for the separation of Pu and MA are now being developed such as molten metal /molten salt extraction, electrotransport into different molten metal cathodes (for example Bi) and deposition or co-deposition of Pu and MA onto different solid cathodes. The aim is to optimise the separation efficiency and to minimise the content of fission products, especially lanthanides (Ln) due to their high neutron capture. For this type of research, it is important that a set of accurate electrochemical and thermochemical data for all actinides is available [59-61]. This is the reason for initializing a systematic electrochemical study of the actinides in LiCl-KCl eutectic melt. So far electrochemical data for Am and Pu have been obtained and are reported.

2.2.2.2 Experimental

The electrochemical experiments, storage and handling of all chemicals were carried out in a glovebox in purified Ar atmosphere (< 1 ppm of water and oxygen). The glovebox is equipped with a well-type oven in which the experimental setup can be moved up and down by means of a lifting system. The electrodes, thermocouple and a stirrer are positioned through a water-cooled flange, which supports the Al_2O_3 or quartz crucible used in the electrochemical cell. The electrolytic bath consisting of Pu^{3+} dissolved in LiCl-KCl eutectic (Aldrich 99.99%) was prepared by oxidising Pu-metal (ITU stock material) introduced in a molten Bi phase in the bottom of the crucible by adding $BiCl_3$ the salt phase. The Am^{3+} bath was prepared by the same method but by oxidising Am-metal (ITU

stock material, Am^{241} high purity, > 99%) introduced in a molten Cd phase in the bottom of the crucible by adding $CdCl_2$ to the salt phase. The following redox reactions are obtained:

$$Pu^{0}_{Bi\ phase} + Bi^{3+}_{salt\ phase} \leftrightarrow Pu^{3+}_{salt\ phase} + Bi^{0} \quad \textbf{(3)}$$

$$2Am^{0}_{Cd\ phase} + 3Cd^{2+}_{salt\ phase} \leftrightarrow 2Am^{3+}_{salt\ phase} + 3Cd^{0} \quad \textbf{(4)}$$

No clear evidence for the formation of stable Am(II) is observed using this procedure to prepare the Am containing salt. On the other hand, presence of black powder in the salt phase is observed when Am metal is directly introduced in LiCl-KCl melt containing $CdCl_2$ without any Cd metallic phase. A chemical reaction between generated Am(III) and Am(0) leads in this case to the formation of Am(II) in chloride melt like in the case of Nd [62]:

$$2Am(III) + Am(0) \leftrightarrow 3\ Am(II) \quad \textbf{(5)}$$

The electrochemical techniques used, i.e. cyclic voltammetry and chronopotentiometry, were carried out in an electrochemical cell having a three-electrode setup and a PAR 273 potentiostat with EG&G M270 electrochemical software. Inert working electrodes were prepared using 1 mm metallic W or Mo wires and inserted approximately 5 mm into the bath. The surface area could be determined after each experiment by measuring the immersion depth of the electrode. The reference electrode used was an Ag/LiCl-KCl-AgCl (1 wt%) prepared in a Pyrex glass tube and the auxiliary electrode a 1 mm Mo wire bent into the shape of a spiral. The electrochemical setup is shown in **Figure 18**.

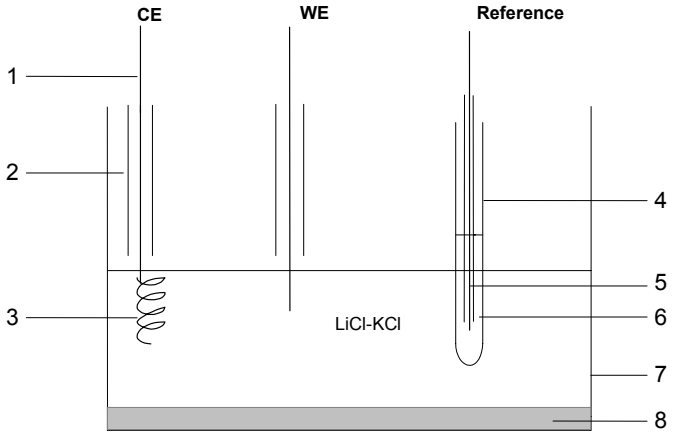

Figure 18. Electrochemical cell; 1) Ni wire; 2) Alumina tube; 3) Mo spiral; 4) Pyrex glass tube; 5) Ag wire; 6) LiCl-KCl-AgCl (1 wt%); 7) Alumina crucible; 8) Liquid Cd pool.

Samples (about 100 mg) were taken from the salt phase, dissolved and diluted in nitric acid. The Pu concentration was determined by ICP-MS analysis and by HPGe γ counting [63,64].

2.2.2.3 Electrochemical behaviour

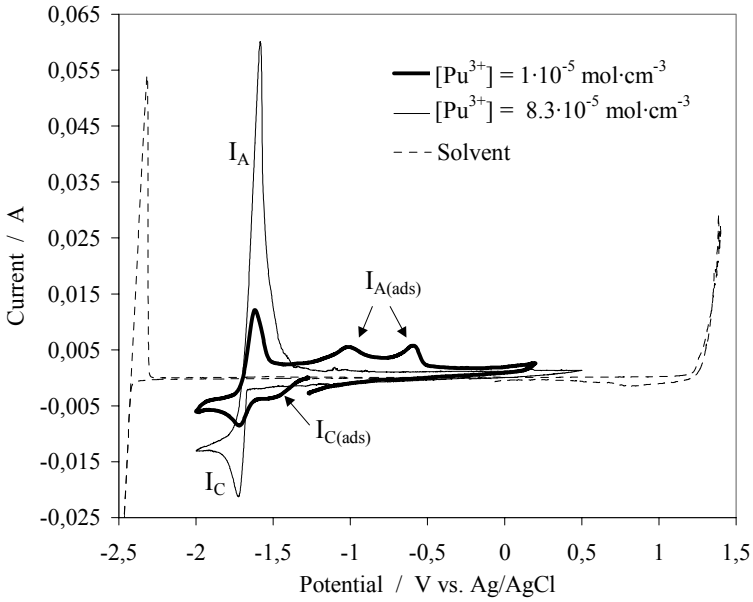

Figure 19. Cyclic voltammograms obtained for Pu^{3+} in LiCl-KCl eutectic salt.
W working electrode (S = 0.2 cm^2), Temperature = 733 K. Reference electrode Ag/AgCl 1 wt%.

The cyclic voltammograms obtained at the W working electrode at 733 K in a solution of $PuCl_3$ (8.3×10^{-5} mol·cm^{-3}) in LiCl-KCl eutectic salt are shown in **Figure 19** [65,66]. A single cathodic peak I_C is clearly associated with a sharp anodic peak I_a. It can thus be concluded that the electroreduction of Pu^{3+} ions proceeds via a one-step process (peak I_c at –1.76 V vs. Ag/AgCl 1 wt%). Peak I_a corresponds to the re-oxidation of the metal deposit formed during the cathodic sweep at the W working electrode. At lower Pu^{3+} concentrations, a second smaller cathodic peak $I_{c(ads)}$ ($E_p \sim -1.5$ V) peak is observed, attributed to underpotential deposition of Pu on the tungsten electrode, probably due to interactions between Pu metal and the surface of the W electrode [66]. This cathodic peak is associated with two re-oxidation peaks $I_{a(ads)}$ occurring at more anodic potentials than peak I_a which corresponds to re-dissolution of deposited Pu metal.

The current of the I_c peak is directly proportional to the square root of the polarisation rate, v (mV/s). Moreover, up to a polarisation rate of 200 mV/s the value of the peak potential E_p is constant and independent of the polarisation rate. According to the theory of linear sweep voltammetry [67], the electrode process is thus reversible and controlled by the rate of mass transfer. For higher polarisation rates (v > 200 mV/s), the cathodic peak potential is shifted negatively, indicating that the system becomes quasi-reversible [29].

A typical cyclic voltammogram obtained at a W working electrode in a solution of $AmCl_3$ (mol·cm^{-3}) in LiCl-KCl eutectic salt is shown in **Figure 20**. The reduction of americium trichloride takes place in two steps. The cathodic wave I_c associated with the anodic wave I_a, which shapes are characteristic of a soluble-soluble exchange, are related to the Am(III)/Am(II) transition. This first wave is followed by second peak II_c which is associated with a sharp anodic peak II_a characteristic of a system involving an insoluble compound corresponding to Am(II)/Am(0) system.

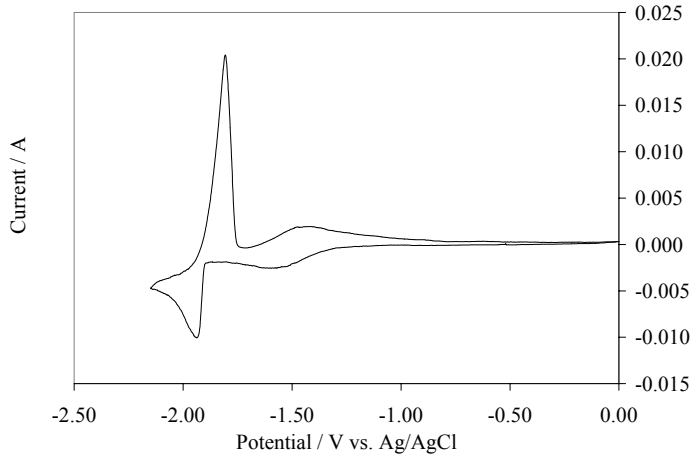

Figure 20. Cyclic voltammograms obtained for Am3+ in LiCl-KCl eutectic salt. W working electrode (S = 0.2 cm2), Temperature = 733 K. Reference electrode Ag/AgCl 1 wt%.

2.2.2.3.1 Diffusion coefficient

For cyclic voltammetry (CV), the diffusion coefficient of Pu^{3+} and Am^{3+} species was calculated using equations (**6**) and (**7**) for reversible systems, controlled by diffusion [29,30,68], assuming that the number of electrons exchanged in the reduction process involved in peak I_c equals 3 for Pu(III) and 1 for Am(III) for which the reduced species are soluble:

$$\frac{I_p}{\sqrt{v}} = 0.61(nF)^{3/2}(RT)^{-1/2} SD^{1/2}_{\mathrm{Pu(III)}} C_{\mathrm{Pu(III)}} \qquad \textbf{(6)}$$

$$\frac{I_p}{\sqrt{v}} = 0.446(nF)^{3/2}(RT)^{-1/2} SD^{1/2}_{\mathrm{Am(III)}} C_{\mathrm{Am(III)}} \qquad \textbf{(7)}$$

where I_p is the peak cathodic current (A), F is Faraday's constant, R is the universal gas constant, T is the absolute temperature, S is the electrode surface area (cm^2), C is the bulk concentration of the electroactive species ($mol \cdot cm^{-3}$), D is the diffusion coefficient ($cm^2 \cdot s^{-1}$), v is the potential sweep rate ($V \cdot s^{-1}$), and n the number of electrons involved in the reaction.

In addition, the linear potential sweep data were transformed according to the convolution principle [29,69] into a form resembling a steady-state voltammetric curve. Typical semi-integrals for voltammetric curves at low scan rates indicate that the m^* value, which is the maximum of the semi-integral of the voltammetry current, is constant. According to the theory of convolution [70,71], the diffusion coefficient of Pu(III), Am(III) and Am(II) is obtained (**Table XII**) using equation (**8**):

$$m^* = -nFSC_{\mathrm{An(III\,or\,II)}} D^{1/2} \qquad \textbf{(8)}$$

The chronopotentiogram (CP) for the electroreduction of Pu(III) to Pu(0) show one step and for Am(III) to Am(0) two electroreduction steps are clearly defined, corresponding to the reduction of Am(III) to Am(II) and of Am(II) to Am(0). As the electrochemical reduction of Pu^{3+} to Pu and Am^{3+} to Am^{2+} can be considered to be diffusion-controlled processes the diffusion coefficients of Pu(III) and Am(III) in the LiCl-KCl eutectic can be calculated (**Table XII**) using the Sand equation [29]:

$$i\sqrt{\tau} = \frac{nFC_{\mathrm{Pu(III)}}s\sqrt{\pi D}}{2} = \text{constant} \quad \textbf{(9)}$$

where i is the current (A) and τ is the transition time (s).

Table XII and **Table XIII** show the diffusion coefficient of Pu^{3+} and of Am^{3+} and Am^{2+} in LiCl-KCl as obtained by the different techniques. The results obtained by different techniques are in fair agreement with each other as the evaluations are affected by experimental uncertainties (e.g. in the determination of the active electrode surface area and by graphical evaluation of transition times in chronopotentiometry). As expected, there is no evidence of a concentration dependence. The average diffusion coefficient obtained by the different techniques is 1.6×10^{-5} $cm^2 \cdot s^{-1}$, 2.4×10^{-5} $cm^2 \cdot s^{-1}$ and 1.15×10^{-5} $cm^2 \cdot s^{-1}$, for Pu^{3+}, Am^{3+} and Am^{2+}, respectively.

Table XII. Diffusion coefficient of Pu^{3+} in LiCl-KCl at 733 K

	Pu^{3+} ($mol \cdot cm^{-3}$)	**Diffusion coefficient 10^5 $D_{Pu^{3+}}$, ($cm^2 \cdot s^{-1}$)**
Cyclic voltammetry	8.3×10^{-5}	1.5
Convolution	8.6×10^{-5} 1.2×10^{-4}	1.3 1.6
Chronopotentiometry	8.6×10^{-5} 1.2×10^{-4}	1.85 1.7

Table XIII. Diffusion coefficient of Am^{3+} and Am^{2+} species in LiCl-KCl

	Diffusion coefficient 10^5 $D_{Am^{3+}}$ ($cm^2 \cdot s^{-1}$)			**Diffusion coefficient 10^5 $D_{Am^{2+}}$ ($cm^2 \cdot s^{-1}$)**		
Temperature (K)	733	783	823	733	783	823
Cyclic voltammetry	2.4	3.2	4.6	1.2	1.7	2.5
Convolution	2.3	3.0	4.9	1.1	1.6	2.7
Chronopotentiometry	2.6	3.4	5.1	-	-	-

2.2.2.4 Apparent standard potential

2.2.2.4.1 Pu^{3+}

By applying the Nernst equation in the case of the formation of a metallic deposit, logarithm analysis of semi-integral curves allows to calculate the number of electrons exchanged as well as the standard potential of the studied redox couple according to [70]:

$$E^0_{\mathrm{Pu(III)/Pu(0)}} + \frac{RT}{nF}\ln\left(\frac{a_{\mathrm{PuCl_3}}}{a_{\mathrm{Pu(0)}}}\right) + \frac{RT}{nF}\ln\left(\frac{m^* - m}{m^*}\right) \quad \textbf{(10)}$$

where $E^0_{Pu(III)/Pu(0)}$ is the standard potential of the Pu(III)/Pu(0) redox couple, $a_{\mathrm{PuCl_3}}$ and $a_{\mathrm{Pu(0)}}$ are the activity of $PuCl_3$ and pure plutonium metal, respectively. The chronopotentiometry curve for reversible electroreduction with formation of an insoluble metallic

deposit, assuming the activity of the pure metal is 1, can be described [72] by the following equation:

$$E(t) = E^{0}_{\mathrm{Pu(III)/Pu(0)}} + \frac{RT}{nF}\ln\left(a_{\mathrm{PuCl_3}}\right) + \frac{RT}{nF}\ln\left(\frac{\sqrt{\tau}-\sqrt{t}}{\sqrt{\tau}}\right) \quad \textbf{(11)}$$

By introducing the apparent standard potential, E^{*0}, for the Pu(III)/Pu(0) redox couple as:

$$E^{*0}_{\mathrm{Pu(III)/Pu(0)}} = E^{0}_{\mathrm{Pu(III)/Pu(0)}} + \frac{RT}{nF}\ln\gamma_{\mathrm{PuCl_3}} \quad \textbf{(12)}$$

where $\gamma_{\mathrm{PuCl_3}} = \frac{a_{\mathrm{PuCl_3}}}{X_{\mathrm{PuCl_3}}}$ is the activity coefficient of $PuCl_3$.

Equations (**10**) and (**11**) can be rewritten as:

$$E = E^{*0}_{\mathrm{Pu(III)/Pu(0)}} + \frac{RT}{nF}\ln X_{\mathrm{PuCl_3}} + \frac{RT}{nF}\ln\left(\frac{m^{*}-m}{m^{*}}\right) \quad \textbf{(13)}$$

$$E = E^{*0}_{\mathrm{Pu(III)/Pu(0)}} + \frac{RT}{nF}\ln X_{\mathrm{PuCl_3}} + \frac{RT}{nF}\ln\left(\frac{\sqrt{\tau}-\sqrt{t}}{\sqrt{\tau}}\right) \quad \textbf{(14)}$$

For cyclic voltammetric curves obtained at reversible conditions ($v < 200$ mV/s), plots of the electrode potential versus $\ln\left(\frac{m^{*}-m}{m^{*}}\right)$ (eq (**13**)) at constant mole fraction are linear which is also the case for chronopotentiometric plots of the cathodic potential versus $\ln\left(\frac{\sqrt{\tau}-\sqrt{t}}{\sqrt{\tau}}\right)$ (eq (**14**)). The slopes averaged 0.023 V·decade^{-1} and 0.022 V·decade^{-1} for CV and CP, respectively, and are in agreement with the theoretical value of 0.021 V·decade^{-1}, expected for a three electron process. This proves, for both techniques, that the Pu^{3+}/Pu^{0} system is reversible in the chosen experimental conditions. Knowing the mole fraction of $PuCl_3$, the apparent standard potential can be obtained from eq (**13**) and (**14**). It was calculated for two mole fractions and three different temperatures and the results are listed in **Table XIV**.

Table XIV. Apparent standard potentials and Gibbs free energy of formation of $PuCl_3$

T (K)	X_{PuCl_3}	E^{*0} vs. Ag/AgCl	E^{*0} vs. Cl_2/Cl^-	$\Delta G^{\infty}_{PuCl_3}$ (kJ·mol^{-1})	Average $\Delta G^{\infty}_{PuCl_3}$ (kJ·mol^{-1})
733	1.662×10^{-3}	CV -1.5715	CV -2.7975	- 809.9	- 809.5
		CP -1.5629	CP -2.7889	- 807.4	
	3.03×10^{-3}	CV -1.5804	CV -2.8064	- 812.4	
		CP -1.5664	CP -2.7924	- 808.4	
773	1.662×10^{-3}	CV -1.5336	CV -2.7699	- 801.9	- 801.9
		CP -1.5312	CP -2.7675	- 801.2	
	3.03×10^{-3}	CV -1.5432	CV -2.7695	- 802.8	
		CP -1.5327	CP -2.7690	- 801.6	
823	3.03×10^{-3}	CV -1.4961	CV -2.7416	- 793.7	- 792.1
		CP -1.4865	CP -2.7302	- 790.4	

2.2.2.4.2 Formal Standard potential of the Am^{3+}/Am^{2+} redox couple

On cyclic voltammograms and the corresponding convolution curves, the apparent standard potential of the involved redox couple, $E'^{0}_{Am^{3+}/Am^{2+}}$, can be deduced in case of the reversible reduction with formation of a soluble compound by:

$$E = E_{1/2} + \frac{RT}{nF}\ln\left(\frac{m^* - m}{m}\right) \quad \textbf{(15)}$$

$$\text{with } E_{1/2} = E^{0}_{Am^{3+}/Am^{2+}} + \frac{RT}{nF}\ln\left(\frac{\gamma_{Ox}}{\gamma_{Red}}\right) + \frac{RT}{nF}\ln\left(\frac{\sqrt{D_{Red}}}{\sqrt{D_{Ox}}}\right) \quad \textbf{(16)}$$

$$\text{and } E'^{0}_{Am^{3+}/Am^{2+}} = E^{0}_{Am^{3+}/Am^{2+}} + \frac{RT}{nF}\ln\left(\frac{\gamma_{Ox}}{\gamma_{Red}}\right) \quad \textbf{(17)}$$

The values of $E'^{0}_{Am^{3+}/Am^{2+}}$ obtained by these different techniques are listed in **Table XV**.

Table XV. Apparent standard potentials and Gibbs free energy of formation for the Am^{3+}/Am^{2+} redox couple

T (K)		$E'^{0}_{Am^{3+}/Am^{2+}}$ vs. Ag/AgCl		$E'^{0}_{Am^{3+}/Am^{2+}}$ vs. Cl_2/Cl^-	$\Delta G^{\infty}_{Am^{3+}/Am^{2+}}$ (kJ·mol^{-1})	Average $\Delta G^{\infty}_{Am^{3+}/Am^{2+}}$ (kJ·mol^{-1})
	CV	-1.463	CV	-2.690	-259.6	
733	Conv	-1.466	Conv	-2.693	-259.8	-260.1
	CP	-1.475	CP	-2.702	-260.8	
	CV	-1.446	CV	-2.681	-258.7	
773	Conv	-1.443	Conv	-2.678	-258.4	-258.2
	CP	-1.435	CP	-2.670	-257.6	
	CV	-1.398	CV	-2.641	-254.9	
823	Conv	-1.393	Conv	-2.636	-254.4	-254.1
	CP	-1.377	CP	-2.621	-252.9	

2.2.2.4.3 Formal standard potential of the Am^{2+}/Am^0 redox couple

The formal standard potential $E'^{0}_{Am^{2+}/Am^0}$ can be calculated using simple analysis of the cyclic voltammograms as well as convolutive analysis. For a reversible reduction with formation of an insoluble species, the potential peak is linked to the formal standard potential by the following equation [62].

$$E_p = E^0_{Am^{2+}/Am^0} + \frac{RT}{nF}\ln\left(\frac{a_{Am^{2+}}}{a_{Am^0}}\right) - 0.854\frac{RT}{nF} \quad \textbf{(18)}$$

Assuming that the activity of the deposited americium is unity and that no Am^{2+} is present initially in the bulk (i.e. $c_{Am^{3+}} = c_{Am^{2+}}$), equation (**18**) can be rewritten in the mole fraction scale as:

$$E_p = E'^{0}_{Am^{2+}/Am^0} + \frac{RT}{nF}\ln(X_{Am^{3+}}) - 0.854\frac{RT}{nF} \quad \textbf{(19)}$$

Considering voltammograms recorded at scan rate below 200 mV·s^{-1} for which the system Am^{2+}/Am^0 is considered as reversible, the apparent standard potential is deduced from the measurement of the potential of the peak II_c using equation (**19**), see **Table XVI**.

Table XVI. Apparent standard potentials and Gibbs free energy of formation of Am^{2+}/Am redox couple

T (K)	$E'^{0}_{Am^{2+}/Am^{0}}$ vs. Ag/AgCl		$E'^{0}_{Am^{2+}/Am^{0}}$ vs. Cl_2/Cl^-		$\Delta G^{\infty}_{AmCl_2}$ (kJ·mol^{-1})	Average $\Delta G^{\infty}_{AmCl_2}$ (kJ·mol^{-1})
733	Conv	-1.686	Conv	-2.913	-562.3	-561.9
	CV	-1.682	CV	-2.909	-561.4	
773	Conv	-1.656	Conv	-2.891	-557.9	-558.3
	CV	-1.661	CV	-2.895	-558.7	
823	Conv	-1.625	Conv	-2.869	-553.7	-554.3
	CV	-1.631	CV	-2.874	-554.8	

2.2.2.4.4 Thermodynamic properties of $PuCl_3$, $AmCl_3$ and $AmCl_2$

The standard free energy of formation, $\Delta G^{\infty}_{AmCl_2}$ at infinite dilution is calculated from the apparent standard potentials according to:

$$\Delta G^{\infty}_{AnCl_x} = nFE^{*0}_{An(III\,or\,II)/Am(0)} \quad \textbf{(20)}$$

and listed for $PuCl_3$, $AmCl_3$ and $AmCl_2$ in **Table XVII**.

The plot of $\Delta G^{\infty}_{PuCl_3}$, $\Delta G^{\infty}_{AmCl_3}$ and $\Delta G^{\infty}_{AmCl_2}$ as a function of temperature shows a linear dependence. A least-squares fit of the standard Gibbs free energy of formation versus temperature data can then be expressed by the following equation:

$$\Delta G^{\infty}_{AnCl_x} = \Delta H^{\infty}_{AnCl_x} - T\Delta S^{\infty}_{AnCl_x} \quad \textbf{(21)}$$

from which values of enthalpy ($\Delta H^{\infty}_{AnCl_x}$) and entropy ($\Delta S^{\infty}_{AnCl_x}$) of formation at infinite dilution are obtained:

$$\Delta G^{\infty}_{PuCl_3} = -956.6 + 0.200\cdot T \quad \textbf{(22)}$$

$$\Delta G^{\infty}_{AmCl_3} = -933.6 + 0.152\cdot T \quad \textbf{(23)}$$

$$\Delta G^{\infty}_{AmCl_2} = -623.9 + 0.085\cdot T \quad \textbf{(24)}$$

Table XVII. Gibbs free energy of formation for AmCl2 and AmCl3

T (K)	$\Delta G^{\infty}_{Am^{3+}/Am^{2+}}$ (kJ·mol^{-1})	$\Delta G^{\infty}_{AmCl_2}$ (kJ·mol^{-1})	$\Delta G^{\infty}_{AmCl_3}$ (kJ·mol^{-1})	$\Delta G^{\infty}_{PuCl_3}$ (kJ·mol^{-1})
733	-260.1	-561.9	-821.9	-809.5
773	-258.2	-558.3	-816.6	-801.9
823	-254.1	-554.3	-808.3	-792.1

2.2.2.5 Electrolysis of An onto solid and liquid electrodes

The choice of cathode material onto which An are deposited during electrolysis is essential. Two characteristics must be taken into account. On one hand, the metallic deposit must be stable enough to prevent undesired side-reactions. In the case of deposition on most solid cathodes this is difficult because the deposited metallic Am, for example, reacts with the dissolved Am(III) to form Am(II) according to:

$$2Am(III) + Am(0) \leftrightarrow 3Am(II)$$

On the other hand, enough difference in reduction potentials between An (especially the MA) and Ln is needed to allow a selective electrochemical reduction. **Table XVIII** lists the reduction peak potentials obtained from cyclic voltammetry measurements of Pu, Am, La and Nd on W, Al and Bi cathodes. For example, only 100 mV is found between Pu and La reduction on molten Bi, compared with nearly 300 mV on solid Al (**Table XVIII**). The difference in reduction potentials on an Al electrode between Am^{3+} (0.45 wt%) and Nd^{3+} (0.5 wt%) at 733 K is around 100 mV. A separation of these two elements is therefore conceivable according to the results obtained by means of cyclic voltammetry.

Table XVIII. Potential peak (*Ep*) of cyclic voltammetric curves obtained on Al, Bi and W cathodes (obtained at a scan rate of 100 mV/s in LiCl-KCl media (733 K) for a MCl_3 (where M = Pu, Am, La or Nd) concentration in the range of 0.5 to 1.5 wt%).

	E_p (V vs. $Ag/^{1wt\%}AgCl$)		
	W	Bi	Al
Pu	-1.75	-1.15	-1.22
Am	-1.95	-1.18	-1.30
Nd	-2.08	-	-1.40
La	-2.10	-1.25	-1.49

Electroseparations have been performed on liquid bismuth electrodes starting with solutions of LiCl-KCl eutectic containing $PuCl_3$ and $LaCl_3$ salts. The experiments were carried out using the dissolution of a Pu metallic rod as anodic reaction and the reactions involved in the electrolysis are the following:

anodic side $\quad Pu^0 \rightarrow Pu^{3+} + 3e^-$

cathodic side $\quad M^{3+} + 3e^- \xrightarrow{Bi} M^0{}_xBi_y$

where M can be Pu or La depending on the efficiency of the electrolytic separation.

The electroseparations were carried out using different ratios of Pu^{3+} and Ln^{3+} (Pu^{3+}/La^{3+} = 4 and 10) and with different current densities (**Table XIX**). During the experiment, salt samples were taken to monitor the Pu and La concentrations. The molten Bi pool electrode (S ~ 5 cm^2, h ~ 7–8 mm) was not continuously stirred during the electrolysis. The main results from the salt analysis are also listed in **Table XIX**.

Table XIX. Results from separation of Pu from La onto liquid Bi

Run	Pu/La Ratio	Current density (mA/cm^2)	E_c (V) vs. Ag/AgCl	E_a (V) vs. Ag/AgCl	Pu and La in salt (wt%)			
					Before		After	
					Pu	La	Pu	La
1	4	10	-1.1	-1.55	0.85	0.18	0.70	0.18
2	4	30	-1.2 to -1.45	-1.37	0.83	0.19	0.87	0.10
3	10	20	-1.15	-1.41	1.85	0.18	1.42	0.17
4	10	50	-1.4	-1.20	1.89	0.18	1.66	0.08

The results, **Table XIX**, show that the current density must be carefully chosen in order to accomplish an efficient separation of Pu from La on a molten Bi electrode. From the decrease in La concentration in run 2 and 4 it can be concluded that lanthanum was co-deposited together with Pu. This is confirmed by the value of the cathodic potential during the electrolysis, i.e. reduction of La occurs around –1.4 V. The current density applied in the experiment can be divided by the initial Pu concentration and it is seen that separation of Pu from La (low current densities) is accomplished for 12 and 11 mA·cm^{-2}·wt%$^{-1}$. At higher current densities, where reduction of Pu and La occur simultaneously, these values are 36 and 27 mA·cm^{-2}·wt%$^{-1}$, respectively. The optimal current density to avoid La reduction is linearly dependent on the concentration of Pu^{3+}. In view of a process development, an efficient separation at sufficiently high current density will be achieved by increasing the amount of actinides in the salt phase and the electrode surface area.

2.2.2.6 Pu/Al alloy characterisation

Pu was electrodeposited onto a thin Al foil in order to characterize the alloy product formed on solid Al. The electrodeposition was carried out in a LiCl-KCl + $PuCl_3$ mixture (T = 733 K) using the dissolution of a Pu metal rod as the anodic reaction. During the experiment the anodic and cathodic potentials showed stable values (–1.5 V and –1.2 V, respectively), which for the cathodic potential is in good agreement with the value obtained for the cyclic voltammetric reduction of Pu^{3+} on an Al electrode. The clean surface revealed a compact and adherent deposit, which could be analysed using SEM-EDX. SEM analysis (**Figure 21**) of the surface revealed the presence of a homogeneous deposit with an atomic ratio of about 80/20, i.e. the formation of a $PuAl_4$ alloy.

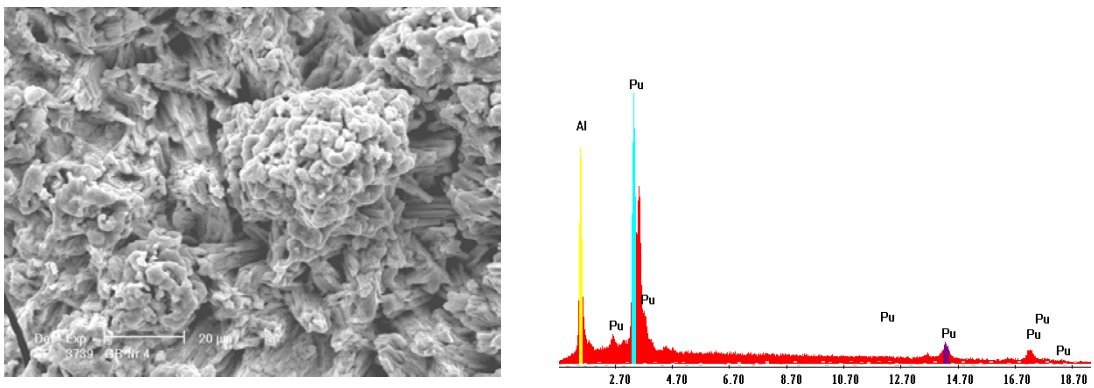

Figure 21. SEM-EDX analysis Al cathode covered by $PuAl_4$ deposit

2.2.2.7 Electroseparation of Pu from Nd onto solid Al

Figure 22 shows the applied current and the cathodic potential obtained from the experiment separating Pu from Nd (initial wt% ratio ~ 2.7) by electrolysis onto an Al foam cathode in LiCl-KCl at 733 K. At the start-up of the electrolysis the current density had to be gradually increased to remove an oxide layer from the Al until stable cathodic and anodic potentials (–1.2 V and –1.45 V, respectively) were obtained.

The results for the concentrations of Pu and Nd in the salt phase before and after the experiment as well as the faradic yield are listed in Table XX. As expected, the Pu^{3+} concentration remained almost constant during the electrolysis, as it was balanced by close to 100% faradic anode and cathode processes:

anodic side $\quad Pu0 \rightarrow Pu^{3+} + 3e^-$

cathodic side $\quad Pu^{3+} + 3e^- \rightarrow Pu^0(Al)$

Also the Nd^{3+} concentration remained unchanged in the salt phase during the electrolysis as the cathode potential (–1.2 V compared to –1.4 V for $Nd^{3+}/Nd^0(Al)$) was not negative enough to allow its reduction. It can be concluded that an efficient separation of Pu from lanthanides can be performed onto solid Al with a faradic efficiency close to 100%.

Table XX. Results of Pu/Nd electroseparation on solid Al foam

Pu and Nd concentration (wt%)				m_{before} (g)	m_{after} (g)	Δm (g)	m_{th} (g)	R (%)
Before		After						
Pu	Nd	Pu	Nd	0.8883	1.2137	0.3254	0.3302	98.5
1.39	0.51	1.26	0.50					

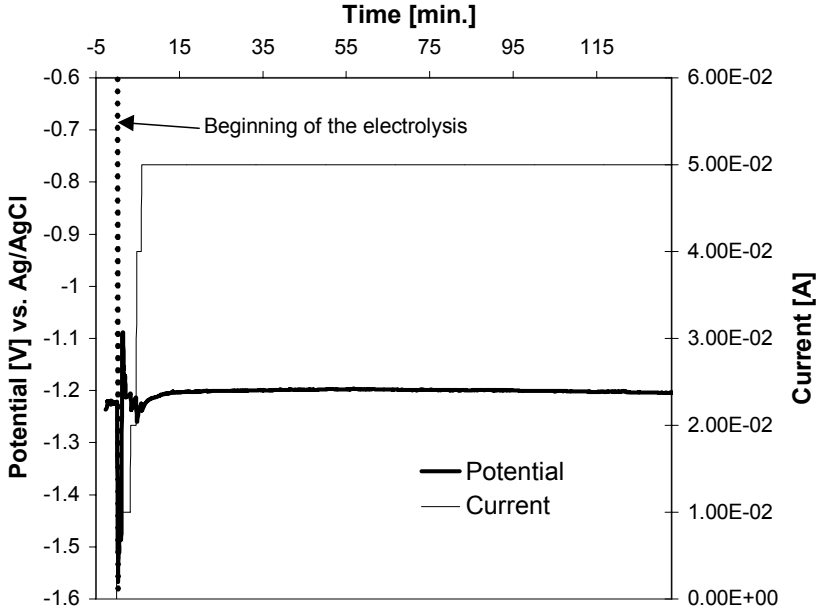

Figure 22. Applied current and cathodic potential

2.2.2.8 Electroseparation of Am from Nd onto solid Al

The electrolysis was carried out with a starting solution of LiCl-KCl (733 K) containing $AmCl_3$ and $NdCl_3$ (Am/Nd ratio ~ 1.8). In the beginning of the electrolysis, the applied current was gradually increased until a stable cathodic potential more positive than –1.3 V, corresponding to the reduction of Am^{3+} on Al was reached (**Figure 23**). At this potential, co-deposition of Nd cannot occur as the reduction of Nd^{3+} on Al requires a cathodic potential more negative than –1.35 V. After 130 minutes of electrolysis, the cathodic potential starts decreasing, obviously due to a decreasing Am^{3+} concentration in the salt phase. Consequently, to avoid Nd co-reduction, the applied current had to be decreased in several steps in order to stay at the potential of Am^{3+} reduction. Finally, at a current of 0.02 A, a stable cathodic potential was reached, probably corresponding to co-reduction of Am-Pu as Pu^{3+} ions had been sufficiently accumulated in the salt melt.

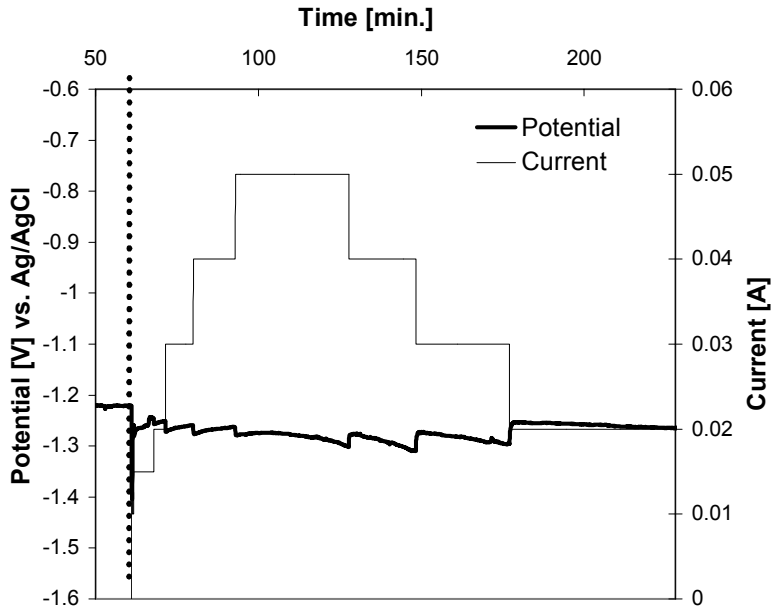

Figure 23. Evolution of potential during electrolysis of Am from Nd on solid Al

The electrolysis was stopped after 340 C and a salt sample was taken to analyse the concentrations of Am, Pu and Nd in the salt melt. A fresh Al foam cathode was then introduced and a second electrolysis carried out using the same conditions.

The results concerning salt composition before and after the two electrolyses are listed in **Table XXI** together with the analysis of the Al foam cathodes after complete dissolution in hydrochloric acid (2 M). It can be seen that the Am concentration in the salt phase decreased in both electrolyses, starting from an initial of 186 mg and ending with 12 mg. Excellent agreement is also obtained comparing the amount of Am recovered from Al electrode to the amount removed from the salt phase. It can therefore be concluded that the Am_xAl_y alloy is stable enough to avoid chemical reaction with Am(III) species in the melt (see eq (**3**)). Moreover, it is also seen that Nd is not reduced during the electrolysis as its concentration in the salt phase is constant. This is supported by the analysis of the Al foam cathodes where almost no Nd was found in the dissolved cathode product. The small amounts of Nd found in the deposit could also be a contamination due to salt still attached to the cathode after cleaning.

Table XXI. Results of Am/Nd electroseparation on solid Al foam

Run	Am, Pu and Nd concentration in salt (mg)						Am, Pu, Nd in Al foam (mg)			*Q* (C)	*R* (%)
	Before electrolysis			After electrolysis							
	Am	Pu	Nd	Am	Pu	Nd	Am	Pu	Nd		
1	186	17	102	50	162	102	135	120	2	340	98
2	54	160	103	12	211	101	46	235	1	300	110

2.3 Electrorefining studies

2.3.1 BNFL contribution

The electrorefiner designed by BNFL and operated by AEAT (Harwell) is based on experience gained at Argonne National Laboratory (ANL). The principle of the process is illustrated schematically in **Figure 24** and has the following main features.

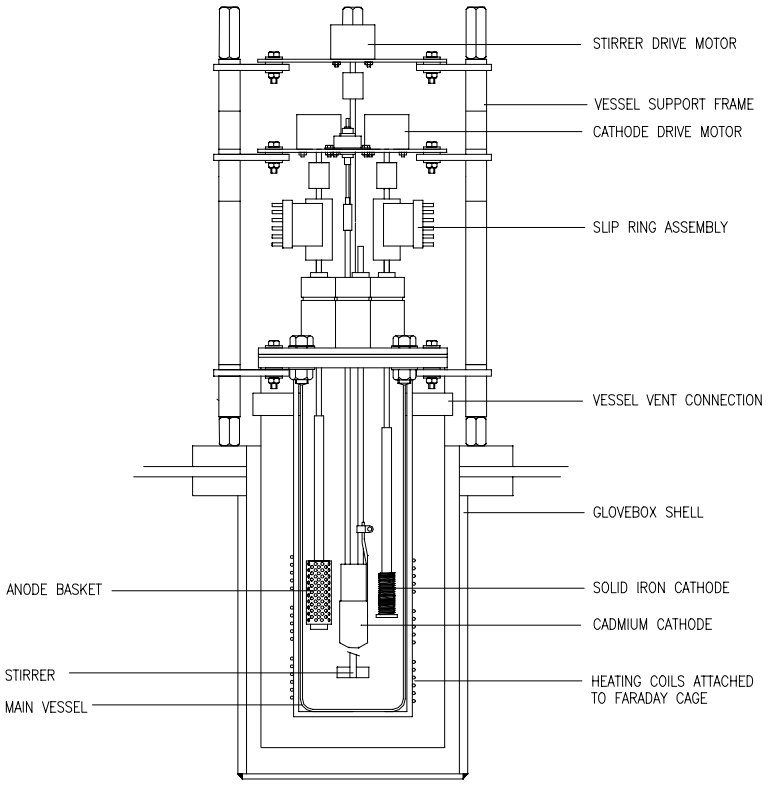

Figure 24. Schematic of the BNFL electrorefiner

1) The electrodes were immersed in molten salt (1.6 kg), typically at 450^{o}C. The salt was the eutectic mixture of LiCl and KCl i.e. 44 wt% LiCl and 56 wt% KCl (i.e. a Li:K mole ratio of 1.4:1).

2) In the case of the experiments described in this report, U was placed in a rotating stainless steel anode basket, immersed in the molten salt and oxidised into the salt as UCl_3. Dissolution required good electrical contact between the fuel and basket.

3) UCl_3 (and in some cases $PuCl_3$) was introduced into the salt to initiate electro-transport to the iron cathode using the reaction.

$$2U + 3CdCl_2 \rightarrow 2UCl_3 + 3Cd$$

4) Uranium was reduced and deposited as metal onto a rotating iron cathode, by the following reaction.

$$U^{3+} + 3e^- \rightarrow U^0$$

Such a solid cathode should only collect U from a mixture of U and more reactive elements such as Pu and Am, which will remain in the salt, since their chlorides are more stable than UCl_3.

$$UCl_3 + Pu \rightarrow PuCl_3 + U$$

5) When $PuCl_3$ was present Pu^{3+} was reduced and deposited into a liquid cadmium cathode with U in proportion to their concentrations in the salt. A 'pounder' was used to disrupt any U metal deposits on the surface of the cadmium which would result in it behaving like the iron cathode and attracting only U.

6) A cadmium pool (3.6 kg Cd) under the electrodes was present to capture any deposits of U which broke away from the cathode. The uranium was recovered from the pool by deposition onto the solid electrode in a separate step.

7) A stirrer for the bulk salt ensured good rates of mass transfer between the electrodes.

8) An Ag/AgCl reference electrode or U metal quasi reference electrode was used for electrochemical control.

Note that in the case of irradiated fuels, the U and Pu products are separated from the fission products because:

- the more reactive fission products such as alkali metals and alkaline earth metals remain in the molten salt in chloride form;
- the noble fission products such as ruthenium and palladium are probably not oxidised and are retained in the anode basket or fall into the cadmium pool, although this remains to be proven and depends on their behaviour at the anode.

2.3.1.1 Assessment of controlling parameters

A number of rate-controlling parameters were assessed, these were:

- Effect of concentration
- Mass transport (in salt and at electrode surfaces)
- Electrode surface
- Electrode potential
- Effect of temperature
- Saturation levels of liquid cadmium
- Equilibration

2.3.1.1.1 Concentration effects

During the early stages of the experimental programme, the uranium concentration in the electrolyte was steadily increased from around 1 wt% to approximately 4 wt%. It was found that the polarisation of the cathode was reduced with increasing concentration. Hence, much higher currents were observed in the higher concentration solution at the same cathode potential. No significant effect of increasing the Pu concentration and reducing the U concentration were observed.

2.3.1.1.2 Mass transport

Effects of mass transport can be seen in two main areas:

- mobility of electroactive species (linked to concentration) dissolved in the electrolyte, which is often observed as a depleted boundary layer at an electrode;
- diffusion or migration of a species into an electrode, which in this case is the migration of deposited metal into a liquid Cd cathode.

The cell employed in these experiments used three electrodes:

- a solid rotating iron cathode,
- a stainless steel anode basket,
- a Cd liquid metal cathode.

➢ Effect of solid electrode rotation speed

The anode was rotated at 0, 7 and 60 rpm for periods of 10 minutes, with a cathode speed of 0.9 rpm and static salt mixer. As **Figure 25** below shows, there was little effect with anode speed. However, the basket shape was changed, so that it has two opposing flat sides, to provide improved mixing.

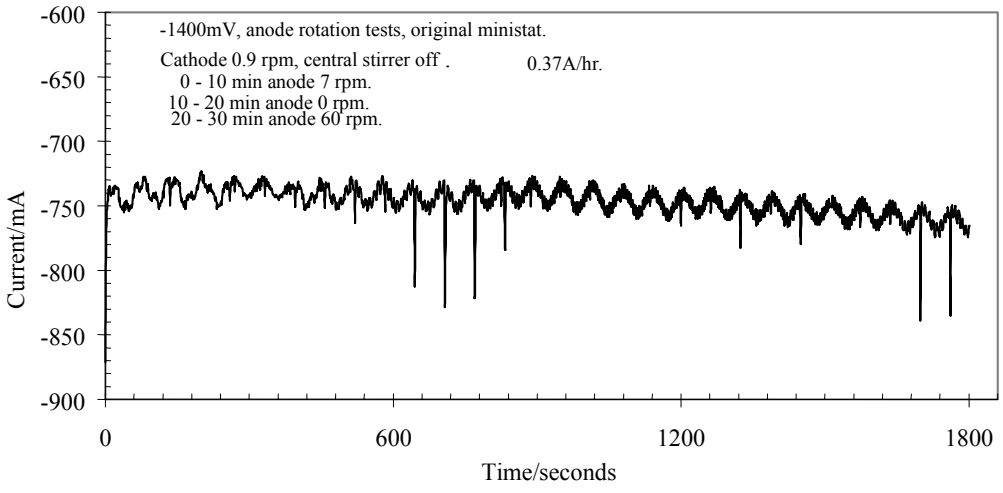

Figure 25. Variation of current with time and anode rotation speed at -1.4V)

Tests with cathode, rotation speeds of 1, 4 and 75 rpm for periods of 10 minutes were performed, with an anode rotational speed of 2 rpm and static salt mixer. A small increase in current was noted (from 770 mA to 820 mA).

- Effect of Salt Stirrer rotation speed

Figure 26 shows the small effect of stirrer speed on cell current with a ~50 mA increase in current with ~100 rpm stirrer speed. It also shows a general lack of sensitivity to rotation of anode, cathode or stirrer.

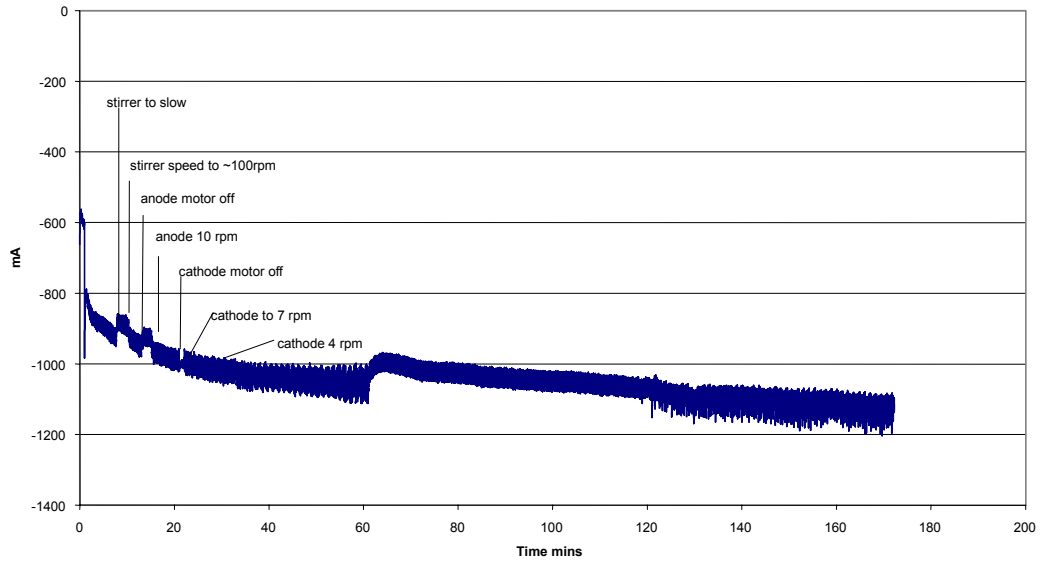

Figure 26. Current vs. Stirring Speed

2.3.1.1.3 Electrode surface

- Solid Surface

Deposition of a metal at a solid surface was found to be unpredictable. Dendritic growth was found to be patchy and inconsistent across a metal surface that was theoretically the same. This has remained largely unexplained, but could be linked to the way the initial few monolayers of deposit are laid down on the electrode surface. This could also be related to the formation of highly reactive sites, for example sites comprising a Fe/U alloy, which is known to form, and has been observed as an underpotential deposition on an iron cathode. This underpotential deposition has not been observed on a tungsten electrode. The most likely effect of inconsistent yields is thought to be surface condition of the cathode.

- Liquid Surface

Surface effects at the liquid Cd electrode surface were found to be more complex. It was observed that current could either increase or decrease during metal deposition with time. In the first case, where the current increased with time, it was found that disturbing the electrode surface reduced the current to a number, which approximated that of the original value in most cases. This was explained as solid U metal forming at the liquid metal cathode surface at a greater rate than it could migrate into the bulk metal Cd.

The variation of current with time, for constant cathode potentials ranging from –1.3 V to –1.45V, is shown in **Figure 27**. The current was constant at the lower overpotentials, but at –1.4V (105 mA) and –1.45V (140 mA) the current rose with time suggesting that the surface area was increasing as a result of dendrite formation at these higher currents. Current densities ranged from 25 $mA \cdot cm^{-2}$ at –1.3V to 60 $mA \cdot cm^{-2}$ at –1.45V.

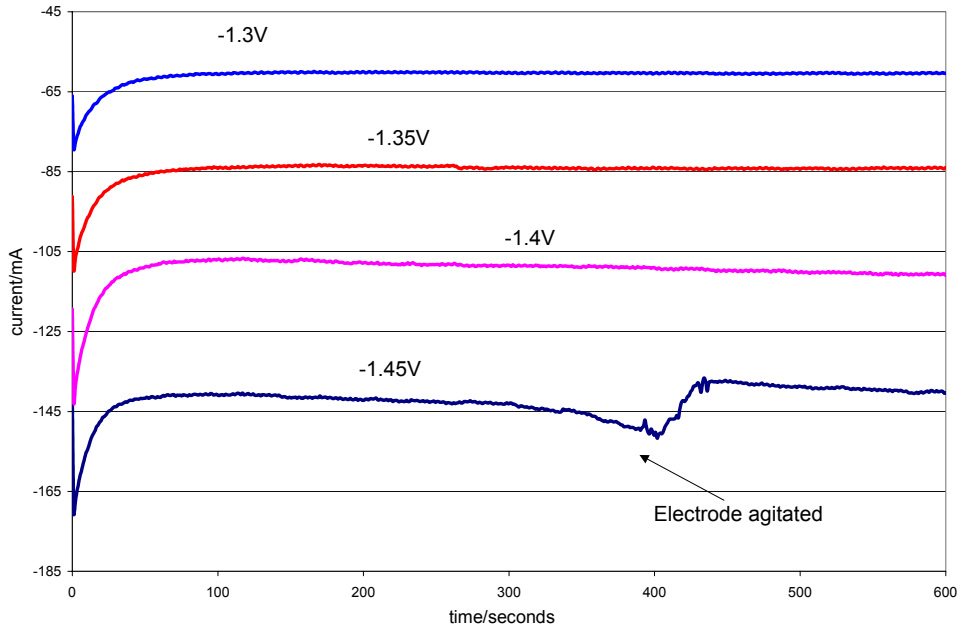

Figure 27. Variation of current with time for liquid Cd cathode (potentials between –1.3 and –1.45 V)

During agitation of the liquid cadmium, by raising and lowering the cathode, the current increased because of the increased cadmium surface area. After agitation, the current fell to a lower level, possibly because dendrites had been submerged or dissolved, but then increased again with time. The variation of current with time, with unsaturated Cd and under potentiostatic conditions of –1.45 V, is given in **Figure 28** which shows that the current was reduced to close to its original level by operating the pounder.

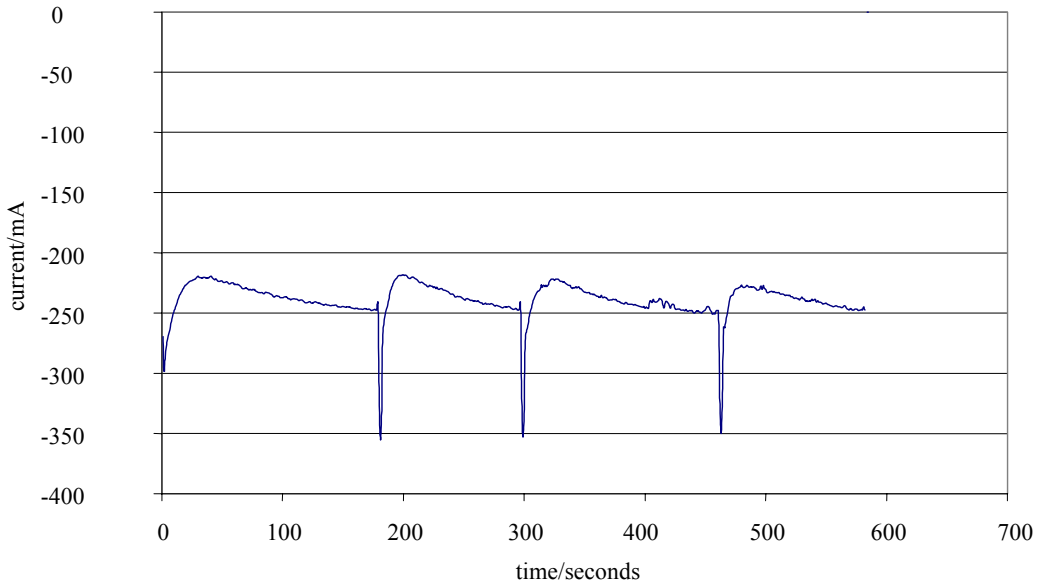

Figure 28. Variation of current with time for liquid Cd cathode below saturation and operated at –1.45V

On approaching the U solubility limit of the cadmium (1.6 wt% U at 450°C) the current rose with time even at the lowest voltage indicating that dendrite formation could not be suppressed with pounding. This effect is illustrated by **Figure 29**.

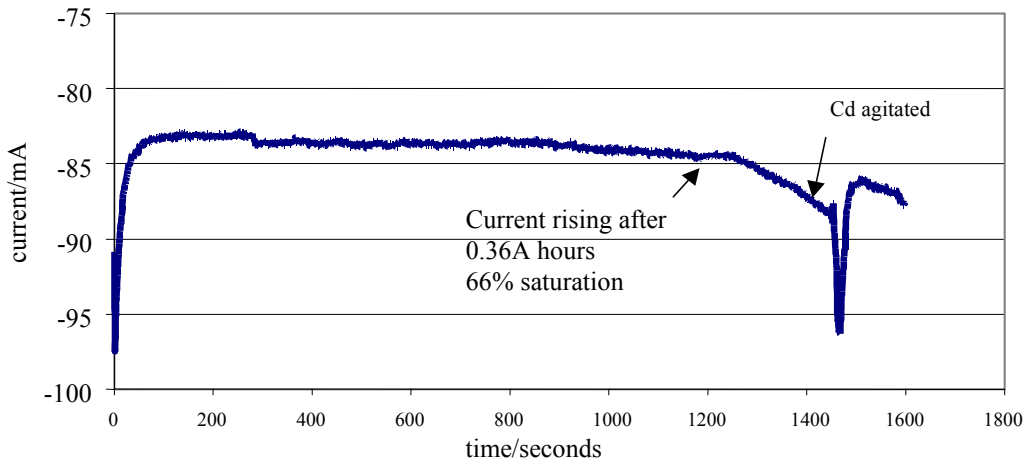

Figure 29. Variation of current with time for liquid Cd cathode at –1.35 V

As the Cd became saturated and then super-saturated with U to a maximum U concentration that was 1.8 times saturation, the pounder became less effective at reducing current, as shown in **Figure 30** below.

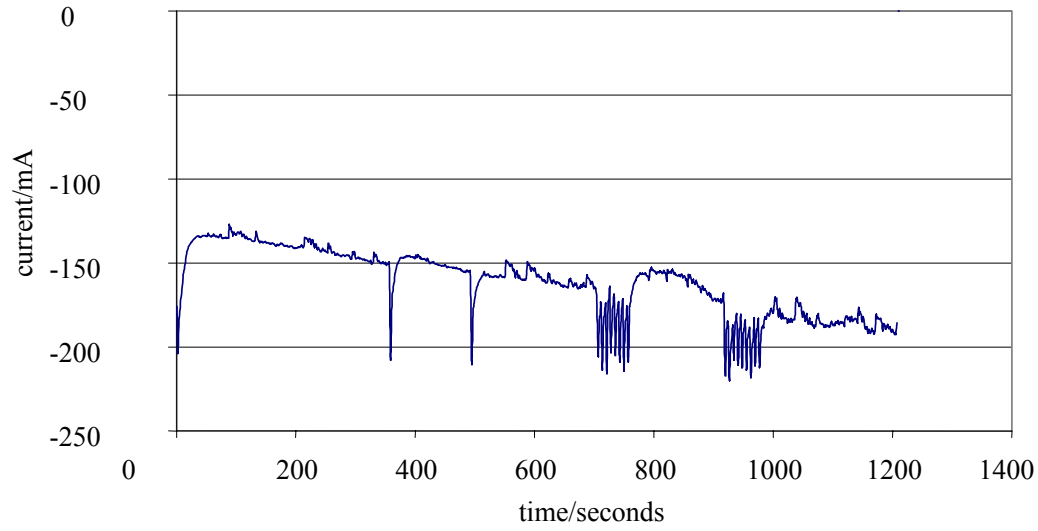

Figure 30. Variation of current with time for saturated U electrode operated at –1.45 V

2.3.1.1.4 Electrode potential

The potential of an operating electrode is not associated with a single property, but made of several components, for example:

- resistive losses in the electrolyte (normally compensated for by use of a Luggin capillary), related to salt concentration and composition with respect to a reference electrode;
- specific surface area of the electrode;

- activity of electroactive species at the electrode surface.

The equipment was not designed to interrogate the specific aspects of electrode potential; however, the generic effects were observed in many of the other controlling parameters discussed in this section.

2.3.1.1.5 Effect of temperature

There was a slight increase in U/Pu and Pu/Am separation factors, but no major effect of temperature was observed between 450°C and 500°C, although the UCd_{11} stability boundary is thought to be about 480°C. Higher temperatures would be expected to increase the diffusion coefficients, this should give rise to smaller concentration gradients and this effect should be calculable. Although, there is a huge range of reported diffusion coefficients, which would make the calculation unreliable. However, use of high temperatures would lead to significant problems from Cd volatilisation.

2.3.1.1.6 Effect of Cd saturation on separation factors

No major effect was observed after exceeding U saturation although the separation factors did rise slightly in three out of four measurements. Local equilibrium would predict that once the U reaches saturation the following occurs:

1) The U concentration in the Cd becomes constant.
2) Further deposition of U occurs but it precipitates.
3) Deposition of other species continues to occur and their concentrations in the Cd increase.
4) The cadmium becomes out of equilibrium with the salt, i.e. the ratio of RE to U in the cadmium is too great compared with the salt so a chemical reaction between RE in the cadmium and U or Pu in the salt occurs
5) Effectively, no further electrolytic deposition of other elements will occur.

It is likely that this will only occur at low currents or with well mixed interfaces such that chemical back (re-oxidation) reactions can compete with electrolytic forward (reduction) reactions. Koyama [73] observed this effect with a current of 130 $mA \cdot cm^{-2}$ (~ 2–3 times the highest value used here) but also with stirring the Cd at a speed of ~100 rpm.

2.3.1.1.7 Effect of equilibration

The effect of leaving the electrode to equilibrate with the salt after completion of electrolysis was for the separation factors to approach the reported chemical equilibrium values. The separation factor for Pu/U increased to ~2 whilst for Pu/Am it increased from 1.1 to about 1.3 in the first test and 1.5 in the second test, agreeing well with the literature value (1.5), and higher than values obtained between the salt and Cd pool. The U/Nd separation factors also increased although the results from the low concentrations of Nd are considered to be less accurate.

This is because concentration gradients formed during electrolysis disappear, chemical reactions occur and hence the separation factors improve and approach values predicted by thermodynamic calculations:

$$Pu^0_{Cd} + U^{3+} \leftrightarrow Pu^{3+} + U^0_{Cd}$$

where the equilibrium constant for the reaction is the equilibrium separation factor.

2.3.1.2 Decontamination factors for U and Pu from the minor actinides (WP1 1.9)

2.3.1.2.1 U/Pu separation – solid cathodes

Three main experimental runs were performed, where uranium was deposited onto an Fe cathode, from a salt with a U:Pu ratio of 4:1. The first run was used to check that the analysis procedures chosen would be acceptable, while the second and third runs, determined the effect of high (2–2.5 A) and low (0.8 A) current on U/Pu separation factors. The U/Pu separation factors achieved were found to be 350, 2250 and 6000.

The highest purities measured were U/Pu ratios of 16000 and 17000. Lower values were normally associated with large amounts of Cd or the inclusion of large amounts of salt.

For Pu to deposit on a solid cathode, one should consider the following:

The electrode potentials for U/U^{3+} and Pu/Pu^{3+} are 0.31 V apart. Assuming equilibrium at the electrode, the equilibrium constant for the reaction:

$$UCl_3 + Pu \rightarrow PuCl_3 + U$$

is given by:

$$K = e^{\frac{nF\Delta E}{RT}} = 2 \times 10^6$$

i.e. for metallic Pu to exist with U, the ratio Pu^{3+}/U^{3+} must exceed 2×10^6. However, it is the surface concentrations which are important: as the voltage is increased the surface concentration of U^{3+} could become very low.

Clearly, with the right combination of surface concentration and avoidance of Cd and salt inclusion, very high decontamination factors are possible.

No separation of a combination of U and Pu from minor actinides is possible on solid cathodes

Cadmium contamination of the uranium product was another unexplained phenomenon. One possibility was that it resulted from contact with the alumina scrapers fixed to the vessel inner wall, but that does not seem to be the case since tests involving mechanical contact between the scraper and a larger clean cathode failed to show any deposit. It often occurred late in a test when the U deposit had built up, in one run a good deposit of U free of Cd was observed but later it was covered in Cd. Other possibilities are that after prolonged stirring a ‘mist’ of Cd develops in the salt or produces a vortex sending the Cd up the walls of the ER vessel, which could contact the U deposit after reaching a certain size. Slowing the stirrer and raising the cathode to a higher position in the salt could reduce the latter effect. Cd migration is an issue which should be addressed in future work.

2.3.1.2.2 U/Pu separation – liquid cathodes

Separation of U/Pu from minor actinides is discussed in the next section on WP 10. However it is not possible to separate U/Pu from Am at liquid cathodes because the separation factor is too small. This is confirmed by our results

2.3.1.3 Decontamination factors for minor actinides from lanthanides

Experiments were carried out with liquid cadmium cathodes to measure the separation factors of U, Pu, Am, Nd and Ce.

Graphs of current as a function of time, for two typical low current and high current runs, are shown in **Figure 31** and **Figure 32**. In the low current/voltage runs, the current decreases with time probably as a result of increasing U concentration in the Cd. The current appears to become constant when the Cd becomes saturated with U.

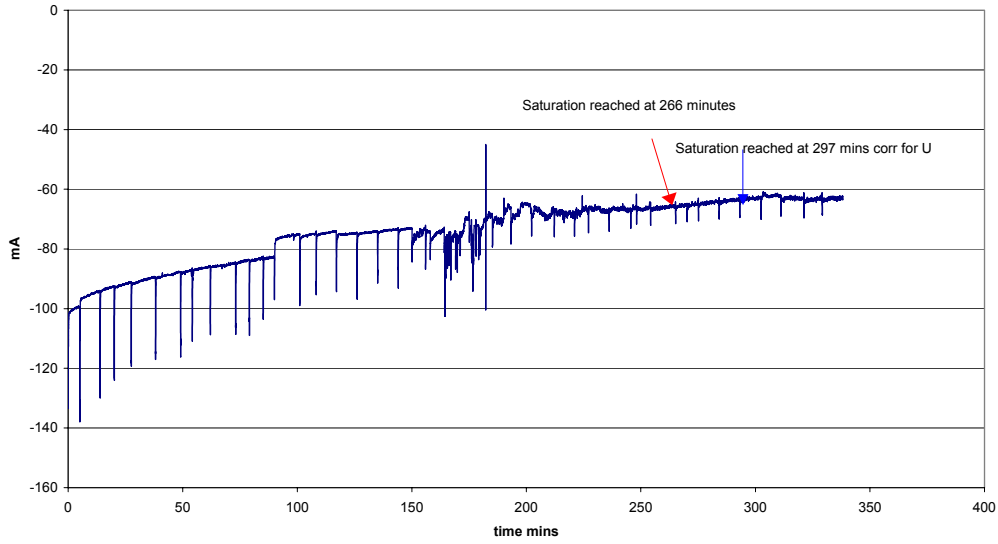

Figure 31. The deposition of U, Pu, Am and a representative rare earth fission product, Nd, into a liquid: low current

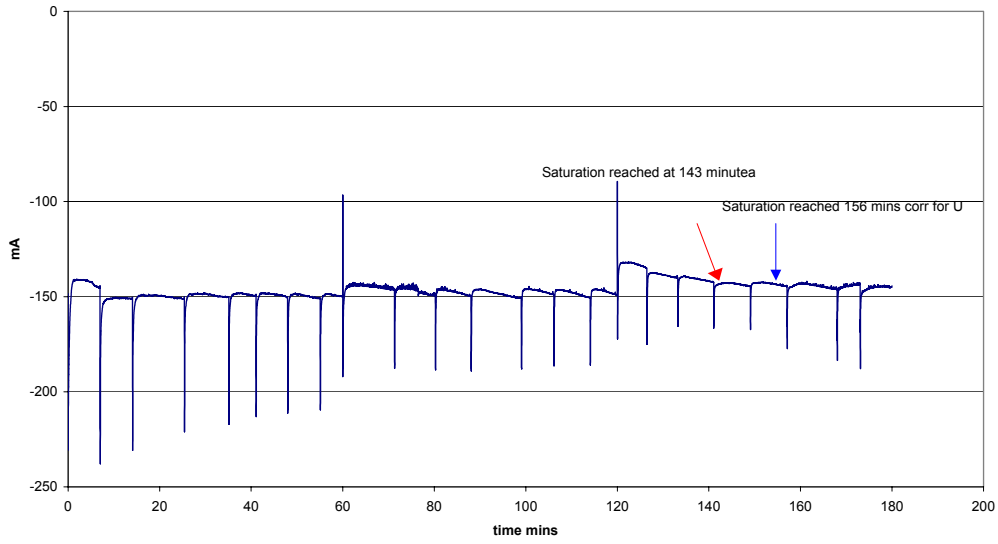

Figure 32. The deposition of U, Pu, Am and a representative rare earth fission product, Nd, into a liquid: high current

Results and conditions for liquid Cd cathode tests are summarised in **Table XXII** below.

Table XXII. Summary of measured SFs in LCC.

U/Pu	Current mA[1]	Separation Factors[3,4]			
		U/Pu	Pu/Am	U/Nd	Pu/Ce
–	Lit[2]	2	1.5	44	23
4:1	75	1.6	1.3	14	–
	75 (500°C)	1.5	1.3	20	–
	150	1.0	1.1	6	–
	150 (500°C)	1.1	1.2	13	–
0.6:1	75	1.4	1.3	11	12
	150	1.2	1.1	4.6	9
	230	0.98	1.1	4.3	4.8

[1]Measured currents were not converted to current densities due to lack of precise value for area (~2.5 cm^2).

[2]Equilibrium SFs [74,75].

[3]Temperature of 450°C (unless noted otherwise).

[4]All SFs are from data when the Cd was below saturation; in several cases the measured SF increased after exceeding the solubility limit for U.

[5]Potentials were approximately –80 mV, –170 mV and –250 mV for the three currents used.

In almost all cases the effective separation factors measured in this work were less than those reported from chemical equilibrium studies. Furthermore, separation factors measured at high current were lower than those at low current. Separation factors for U/Pu, ranged from 1 at high current to 1.5 at low current whereas the equilibrium value is 1.9, which compares well with a separation factor of 2 obtained after letting an electrode equilibrate in the ER on completion of electrolysis. Pu/Am SFs are the most reliable since they were determined by γ-spectroscopy techniques only. These varied from 1.1 at high current to 1.3 at low current, compared with a reported equilibrium value of 1.5. After allowing the liquid cadmium cathode to equilibrate, SFs of 1.3 and 1.5 were obtained. Separation factors for U/Nd are less reliable but low current values were often in the range 14–20 compared with high current values of 6–13. Only a few U/Ce SFs are reliable, the values for the highest current was 4.8, well below the chemical equilibrium value of 23. The variation of separation factor for Pu/Am with current is shown in **Figure 33**

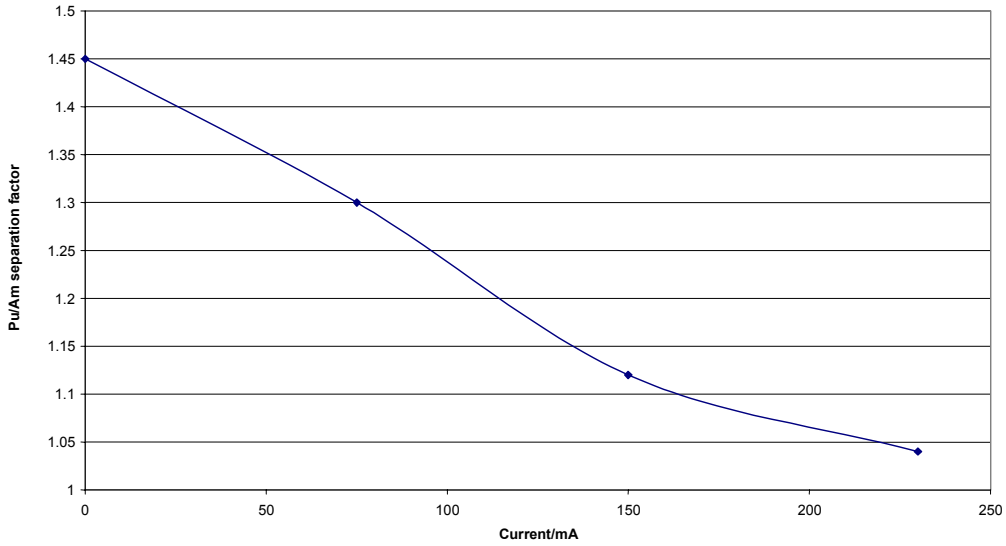

Figure 33. Separation factor for Pu/Am as a function of current

2.3.1.4 Salt decontamination

One of the objectives of the work is to consider methods of salt clean-up. There were two methods considered in this work programme: Li drawdown and electrolytic clean-up using an anode containing Li.

2.3.1.4.1 Li Drawdown

Li, partly in the form of Li/Cd alloy (30g), was contacted with a sample of salt (20 g) from the main electrorefiner vessel in an alumina crucible identical to those used for the liquid cadmium cathodes. The salt was sampled over the following 72 hours. The colour of the salt went from dark purple to white within 2 hours. The change in Am concentration with sample number is shown in **Figure 34**, showing a decontamination factor of 10 000 for Am. Recovery of Pu and Am in the cadmium was >95%

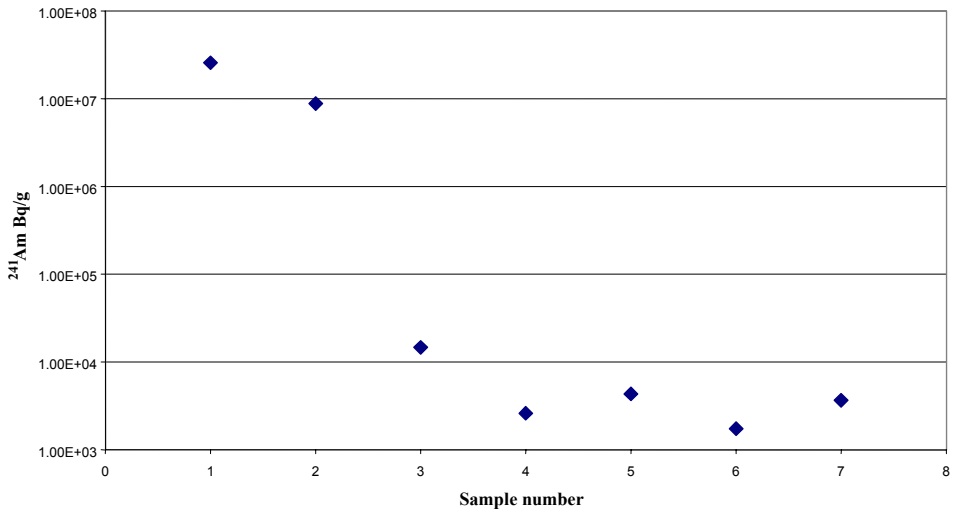

Figure 34. Change of Am activity in salt vs. sample number

2.3.1.4.2 Electrochemical drawdown with Li/Cd anode

In this test Li was dissolved from a Li/Cd anode whilst U was deposited at a solid cathode, thus serving to decontaminate the salt of U. A liquid Cd cathode could be substituted to obtain further selective decontamination of U/Pu and minor actinides from salt. A surprising feature was the problem with anode voltage, which restricted current densities to 50 $mA \cdot cm^{-2}$ whereas it had been anticipated that with an alloy with a composition corresponding to $Li_{0.43}Cd_{0.57}$ there would be virtually no depletion of Li in the boundary layer. A possible explanation may be that precipitation of U/Pu, from chemical reaction of Li, into the layer of Cd at the surface affected the subsequent behaviour of Li.

A relatively small anode surface area was chosen to try to restrict the chemical reduction of U/Pu/RE at the anode. Reduction still occurred to the extent that the U would have precipitated from Cd. Both these aspects could be considered in an anode design. It is likely however, that any modification which improved the current would also increase the chemical reduction reaction. Continued anodic oxidation after removal of Li is possible, but the low concentrations of U and Pu in the Cd would almost certainly only support a low current.

2.3.1.5 Conclusion

In these experiments, there appeared to be two main controlling parameters;

- concentration of the electrochemically active species in the salt;
- the rate at which metals enter the liquid metal cathode.

The separation factor for U/Pu on solid cathodes is high (up to 17 000) but dependent on residual salt and cadmium contamination.

The separation factors for U/Pu on the liquid metal cathode range from 1.6 to 1. For Pu/Am and U/Nd, the SFs ranged between 1.10 to 1.42 and 9 to 35 respectively.

Separation of U from other solutes is possible on a solid cathode and U/Pu and minor actinides from RE is possible at liquid cadmium cathodes depending on their relative concentrations in the salt phase.

Li reduces U, Pu, minor actinides and RE quantitatively leaving a clean salt product.

2.3.2 CRIEPI contribution

2.3.2.1 Introduction

Figure 35 shows the pyroprocess fuel cycle under development by CRIEPI. Pyroreprocessing has been developed for a metal-fuel FBR. This technique is also suitable for a partitioning and transmutation (P-T) process for long-lived nuclides.

Molten salt electrorefining of metallic alloy fuel, as shown in **Figure 36**, is the main process of pyroreprocessing. Electrorefining of unirradiated alloy fuel (71 wt% U, 19 wt% Pu, 10 wt% Zr) already fabricated in ITU for transmutation experiments, has been carried out to obtain basic knowledge of 1) anodic dissolution behaviour of the alloy, 2) recovery of U onto a solid cathode and 3) recovery and separation of actinides into a liquid cadmium cathode.

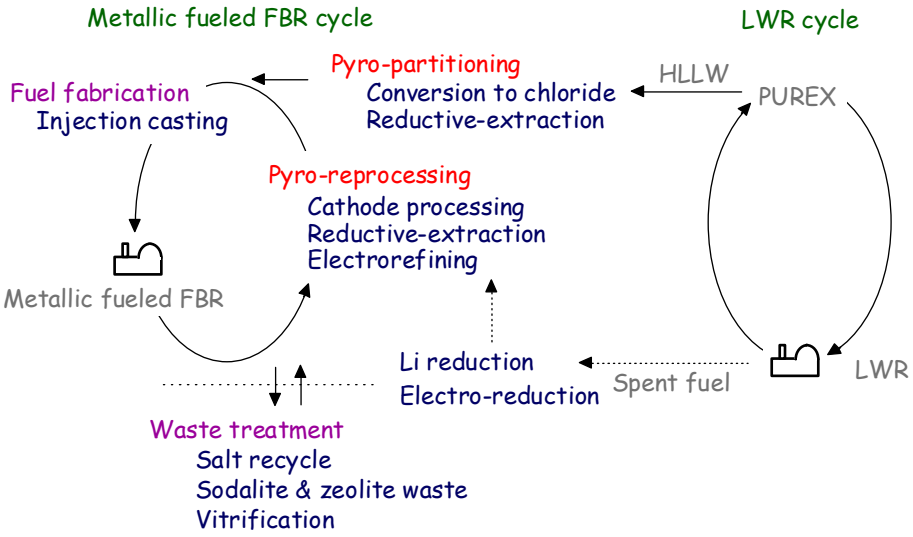

Figure 35. Process flow diagram of pyroprocess fuel cycle

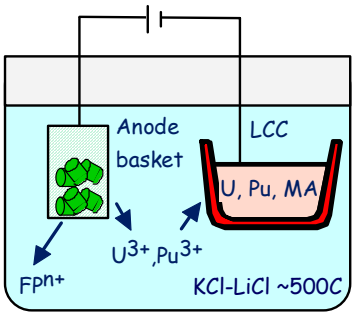

Figure 36. Schematic view of electrorefining

2.3.2.2 Experimental

All the experiments were carried out in a cell with high-purity argon atmosphere. Both the oxygen and the moisture levels in the atmosphere were kept below 10 ppm during the tests. A schematic view of the electrorefiner installed in the cell is shown in **Figure 37**. The inside diameter and depth of the steel crucible were 100 mm and 130 mm, respectively, in which about 1000 g of LiCl-KCl eutectic salt was loaded. A cylindrical steel cathode 20 mm in diameter and 40 mm high was used to recover U, and 60 to 80 g of Cd charged in AlN or Al_2O_3 crucibles were used as a liquid Cd cathode to recover Pu and MAs. One or two pieces of U-Pu-Zr alloys 4.8 mm in diameter and 10 to 50 mm long, were placed in a steel mesh basket used as anode 20 mm outside diameter and 50 mm high. An Ag/AgCl (1 wt% AgCl in LiCl-KCl) reference electrode contained in a thin Pyrex glass tube was used to monitor the electrorefining experiments.

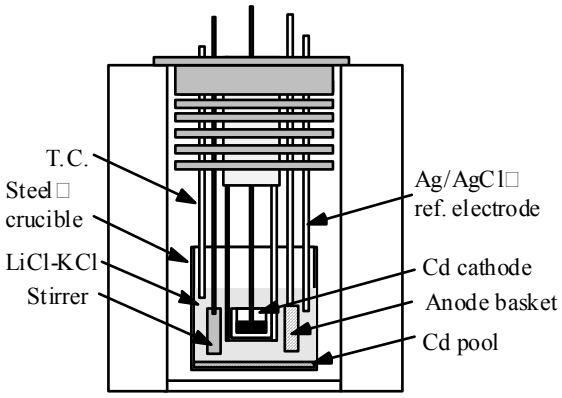

Figure 37. Schematic view of the electrorefiner

Constant current, 100 mA to 800 mA, was passed between the anode and the solid cathode or the liquid Cd cathode. When the determined coulomb was passed, the current supply was stopped and the electrodes were withdrawn. After cooling down, the solid cathode with deposit, the Cd cathode ingot and the remaining anode alloy were recovered from the unit, the ceramic crucible and the anode basket, respectively. During the experiments, salt samples were periodically taken from the electrorefiner using a stainless steel rod as a cold finger. Cd samples were taken using a quartz glass tube and a syringe. The samples were dissolved in nitric acid, and the solutions were analysed using either ICP-MS or XFR.

2.3.2.3 Recovery of U onto solid cathode

Figure 38 (a and b) shows the outside and cutting surface of recovered U onto a solid cathode, respectively. **Table XXIII** shows the summary of condition and result of experiments. The ratio of Pu/U in the salt bath was about 4 before and about 7 after electrolysis. The deposits contain 50–64 wt% of salt and their shape are completely different from a dendrite deposit which is typical for U deposition onto solid cathodes. It seems therefore difficult to obtain a dense uranium deposit in the case of a low U concentration in the salt bath. But collection efficiencies are high, around 90%, and the content of U in the deposit are also high, around 95%. Zr also deposits on the solid cathode and can be recovered.

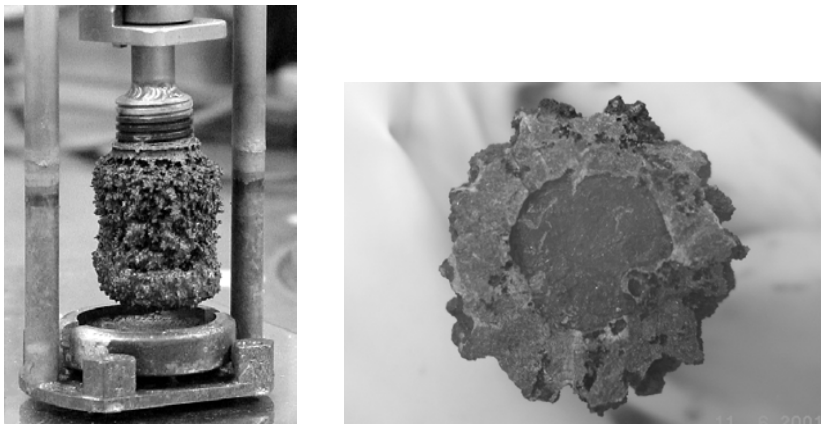

Figure 38. U deposit onto solid cathode (left) with cutting surface (right)

Table XXIII. Experimental conditions and results from U deposition onto a solid cathode

	#4	#7	#10
Current (mA)	400	400	800
Coulomb (C)	8700	16000	10000
Concentration in salt before electrolysis			
U conc. (wt%)	0.73	0.77	0.79
Pu conc. (wt%)	3.1	2.9	3.0
Pu/U ratio	4.3	3.8	3.8
Recovery (%)	86	83	94
Salt in deposit (wt%)	50	64	62
U conc. in metal deposit (wt%)	*	*	94

*Not evaluated due to lack of analytical data for Zr

2.3.2.4 Recovery of U, Pu and MA into liquid Cd cathode

Figure 39 shows the recovered Cd ingot with the broken Al_2O_3 crucible. The upper side in this photo is the bottom of the crucible. The Cd ingot is about 5 mm deep and the remainder of the crucible is occupied by salt. The experimental results are summarised in **Table XXIV** with the experimental conditions. The amount of the actinides and other elements deposited into the cathode was derived from the chemical analysis of Cd taken from the cathode. As seen in **Table XXIV**, the Cd cathode contained Pu and U with a small amount of MAs, Zr and REs.

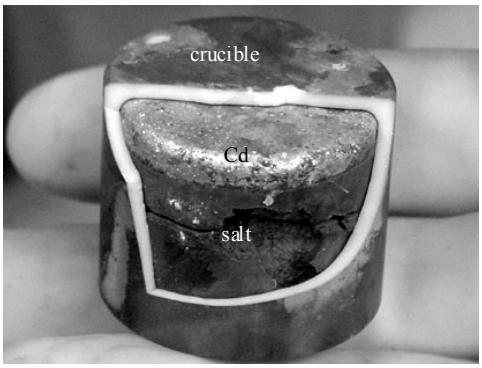

Figure 39. Alumina crucible with cathode Cd ingot

The total concentrations of U and Pu in the Cd cathode in Run #8 and #11 were 3.2 wt% and 3.1 wt%, respectively, which are close to the solubility of Pu in Cd at 753 K (3.03 wt%). In case of the experiments of electrorefining of U and Pu into a liquid Cd cathode from a liquid Cd anode, the total solubility of U and Pu in Cd was reported to be slightly higher than that of Pu in Cd. The concentration of U and Pu derived from a sample taken from the liquid Cd cathode did not increase after reaching the solubility of them because U and Pu formed solid compounds as $(U,Pu)Cd_6$ or $(U,Pu)Cd_{11}$ and they were not taken in a liquid sample of Cd cathode.

Table XXIV. Experimental conditions and results from deposition into a liquid Cd cathode

	#8	**#11**	**#19**
Cathode crucible	AlN	Al_2O_3	Al_2O_3
Current (A)	0.2	0.2–0.12	0.2
Coulomb (C)	3370	4270	2640
Concentration in salt before/after experiment (wt%)			
U	4.4E-1 / 6.4E-1	5.6E-1 / 8.0E-1	1.0E-0 / 1.2E-0
Np	- / -	- / -	- / 3.0E-3
Pu	3.2E-0 / 3.2E-0	3.1E-0 / 3.0E-0	2.5E-0 / 2.5E-0
Am	7.0E-3 / 6.9E-3	7.0E-3 / 6.8E-3	1.4E-2 / 1.3E-2
Cm	- / -	- / -	- / 5.8E-6
Concentration in recovered Cd (After experiment)			
U	7.8E-1	1.1E-0	8.1E-1
Np	-	-	9.3E-4
Pu	2.4E-0	2.0E-0	8.3E-1
Am	3.7E-3	3.1E-3	2.5E-3
Cm	-	-	1.0E-6

Table XXV. Separation factor of each element against Pu in LiCl-KCl/Cd system

	#8 753 K	**#11 753 K**	**#19 783 K**	**Ref. [76] 773 K**	**Ref. [77] 773 K**	**Ref. [78] 773 K**	**Ref. [41] 723 K**
U	1.9E+0	2.43E+0	2.04E+0	1.90E+0	1.88E+0	1.90E+0	1.82E+0
Np	-	-	9.49E-1	-	8.87E-1	1.05E+0	-
Pu	1.0E+0	1.0E+0	1.0E+0	1.0E+0	1.0E+0	1.0E+0	1.0E+0
Am	6.97E-1	6.59E-1	5.97E-1	6.44E-1	6.10E-1	-	-
Cm	-	-	5.34E-1	-	5.34E-1	-	-
Zr	6.52E-1	8.90E-1	2.96E+0	-	-	-	-
Ce	3.76E-2	6.12E-2	3.93E-2	3.88E-2	4.18E-2	3.88E-2	-
Nd	-	4.62E-2	6.31E-2	4.32E-2	4.82E-2	4.22E-2	4.00E-2
La	-	1.40E-2	2.51E-2	1.46E-2	-	1.46E-2	-

Table XXV shows the separation factors of each element versus Pu. The separation factors in the previous experiment in the equilibrium condition are also shown in the table. The separation factor (SF) of metal M is here defined by $SF = D_M/D_{Pu}$, and D_M is distribution coefficient of M, which is defined here by $D_M = X_M/Y_M$ where X_M and Y_M are the mole fractions of MCl_n in the molten salt bath and of M in liquid Cd in the cathode crucible, respectively. The separation factors of U, Np, Am, Cm and Ce against Pu in Run #19, determined from the composition in the recovered Cd and of the salt bath, were about 2.04, 0.949, 0.597, 0.534 and 0.0393, respectively. **Table XXV** shows that the separation

factors of each element in this electrorefining experiments are similar to these in the previous equilibrium experiments. This result indicated that the separation of actinides from REs was achieved effectively by means of the electrorefining and the separation efficiencies of them in the electrorefining, before reaching solubility of them in the Cd cathode, could be almost estimated using the data from equilibrium condition.

2.3.2.5 Dissolution behaviour of U-Pu-Zr alloy

The remained U-Pu-Zr alloys were removed easily from anode basket after electrolysis. As seen in **Figure 40**(a), which shows the radial cutting surface of the alloy, dissolution of the alloy was found to progress from outside to inside leaving a layer around the alloy. **Figure 40**(b) shows that a lump still remained even after the initial U-Pu-Zr alloy had almost completely disappeared.

Table XXVI shows the composition of U and Pu in a small sample from the lump shown in **Figure 40**(b). About the half of the lump was water-soluble and the other half was insoluble. The concentrations of each actinide in the water-soluble part were almost the same as that in the bulk salt. On the other hand, the concentrations of each actinide were very low in the insoluble part, which indicated that the insoluble part consisted mainly of Zr metal. Therefore the layer around the alloy consisted of salt and Zr metal. The dissolution ratios of U, Pu and Zr from the alloy could be estimated using the data of **Table XXVI** and the amount of the initial alloy and of the recovered lump. The calculated dissolution ratios of each U and Pu were 99.92% and 99.97%, respectively. These are higher than the target value of the anodic dissolution ratios of U and Pu in the CRIEPI study to design and evaluate a pyro-reprocessing plant for the metal fuel FBR cycle: 99.5% and 99.9% for U and Pu, respectively. The calculated dissolution ratio of Zr was about 45% in this case. In the other experiment, this kind of lump disappeared completely after excess current was passed. The Zr remaining in the lump was assumed to dissolve completely with electrolysis or disperse into the salt bath as small metal particles.

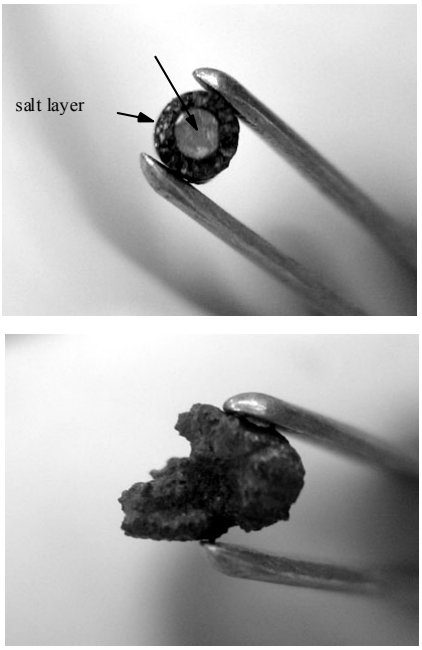

Figure 40. Cutting surface of U-Pu-Zr alloy recovered after electrolysis (top), and recovered salt and Zr metal mixture (bottom)

Table XXVI. Concentration of U and Pu in the salt lump recovered after electrolysis

	Weight (mg)	U (wt%)	Pu (wt%)
Water-soluble part	100.7	0.655	3.32
Insoluble part	101.6	1.02	0.102

2.4 Design and construction of an electrorefiner

2.4.1 Introduction

The general purpose of the activity performed was the transfer of laboratory data obtained during electrorefining experiments to a semi-industrial scale, by means of the design, installation and testing of a plant. A series of campaigns are scheduled to evaluate the distribution behaviour of elements simulating nuclear wastes between molten LiCl-KCl eutectic salt and liquid bismuth. In particular studies of reaction kinetics, reductive extraction and electrorefining, conducted at large scale will provide useful data to validate a mathematical model able to interpret the physicochemical phenomena involved and to furnish elements for design.

Bismuth has been preferred to cadmium metal because the separation factors of trivalent rare-earth elements to uranium or neptunium in the LiCl-KCl/Bi system are one or two orders of magnitude larger than in the LiCl-KCl/Cd system [78].

2.4.2 Description of the PYREL Plant

An electrorefiner designated PYREL has been designed, built and installed in an argon atmosphere glove box (about 1 m wide, 1 m deep and 0.95 m high), and cold tested at the ENEA Brasimone Research Centre (**Figure 41** to **Figure 43**). Prior testing, which simulated some operations to be carried out in the plant, gave useful indications as to melting of salts and bismuth metal, stirring of the liquids, and sampling procedures.

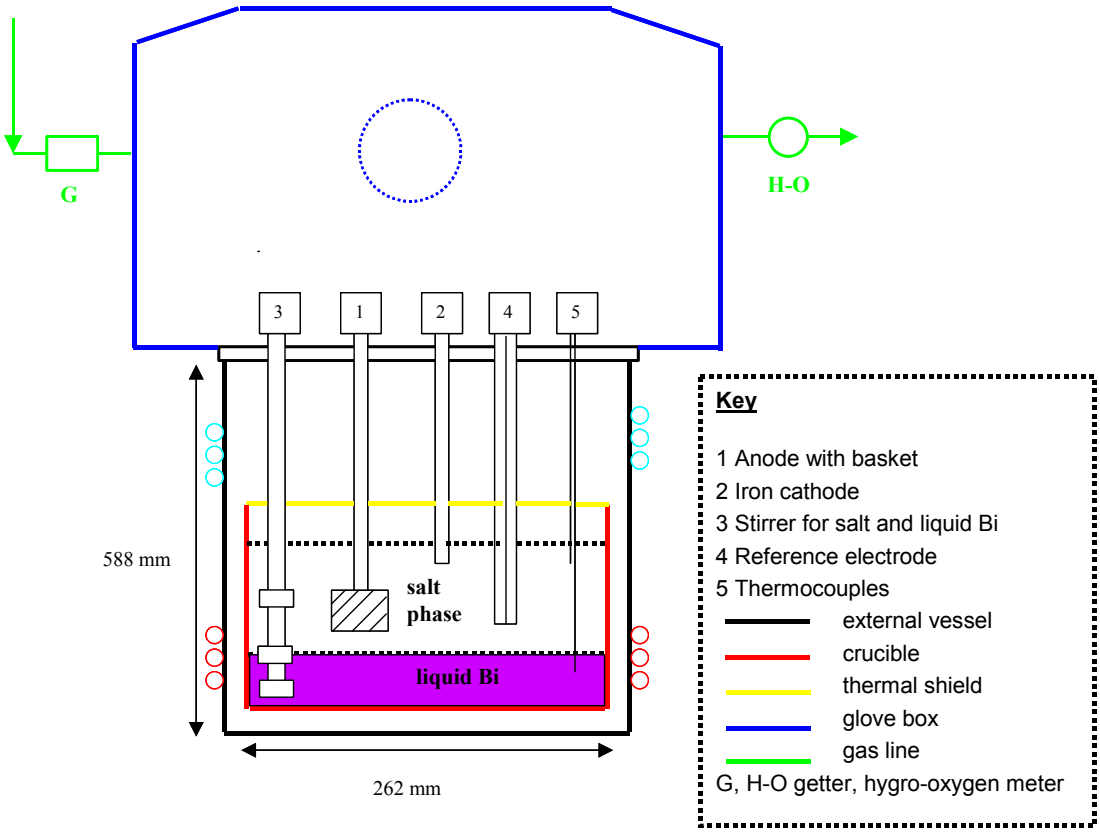

Figure 41. Conceptual scheme of the PYREL Plant

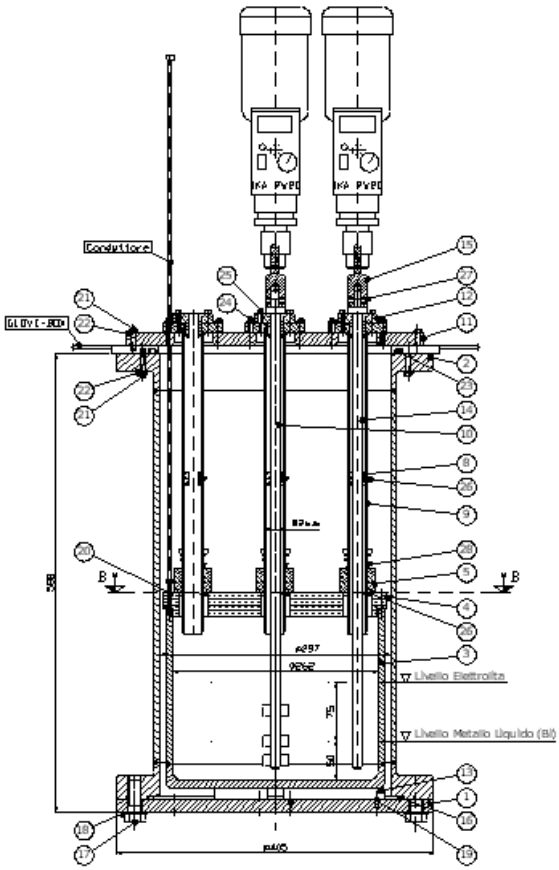

Figure 42. Project drawing showing the vertical section of the electrorefiner and the top cover with nine penetrations

Figure 43. General view of the plant, with steel glove box, electrical supply for heating the ER, and the PC data acquisition system

The electrorefiner is a mild steel vessel (262 mm ID × 220 mm high) heated by a 3-zone furnace supported in an externally water-cooled well in a steel glove box (**Figure 44**). The argon atmosphere is maintained by a continual purge of about 10 $L \cdot min^{-1}$. The electrorefiner contains 26.5 kg Bi (2.69 L) and 6.67 kg LiCl/KCl (4.04 L) and is currently operated at 450°C. The height of the liquid bismuth is 5.0 cm, while that of the liquid salt reaches 7.5 cm. The salts were loaded in two batches, to avoid overflowing [79].

Figure 44. Detail of the thermal insulation of the ER, also showing the copper coil used for cooling

The insulated top plate of the electrorefiner has eight 50 mm penetrations for two stirrers, the thermocouple tube, the reference electrode, and guide-tubes for loading the salts and for introducing the sampling device (**Figure 45**). An additional central penetration is provided for positioning the solid cathode (working electrode). This is a mild steel rod, 12 mm in diameter, encased in a guide-tube in such a way that an apparent surface area of 5.65 cm^2 is exposed to the electrolyte. The pool of molten bismuth serves as a counter-electrode.

The electrodes (anode, cathode, and Ag/AgCl reference electrode) are connected to an Amel Instruments potentiostat (Model 2053) with data logging via a PC.

The oxygen content of the glove box atmosphere is maintained below 20 ppm, and the moisture below 10 ppm during all the operations.

The glove box is fitted with over and under pressure trips. It is also equipped with a transfer box (50 cm long, 31 cm dia.) to limit oxygen ingress during posting.

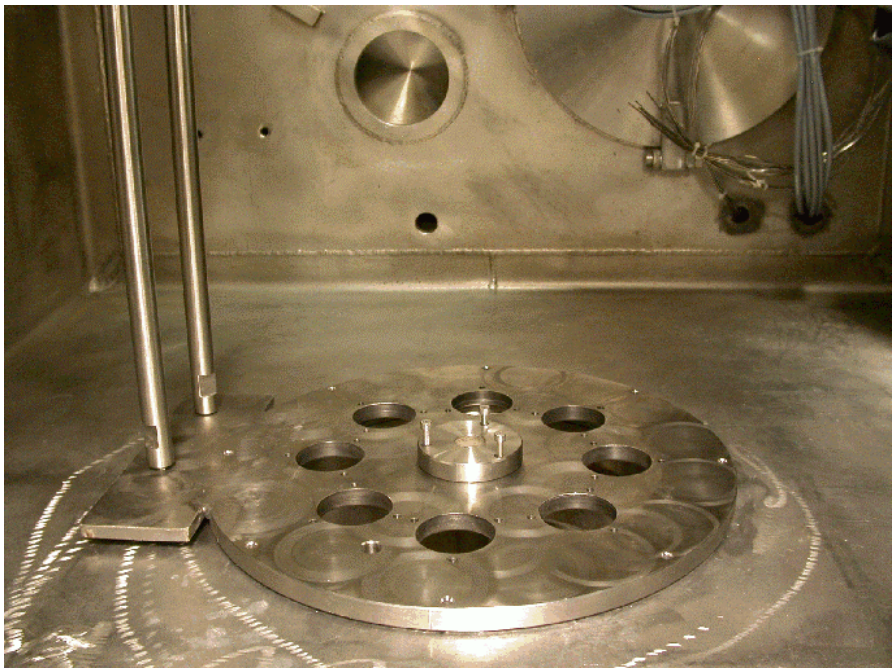

Figure 45. Perforated top cover of the ER, fixed at the internal floor of the glove-box

Six calibrated chromel-alumel thermocouples allow temperatures measurements within ±0.5°C during the experiments (**Figure 46**). They are positioned as follows: Tc 1: liquid metal, Tc 2: molten salt, Tc 3: gas zone in the upper part of the ER, Tc 4: glove-box floor, Tc 5: external jacket, Tc 6: external flange.

Figure 46. Diagram showing the trend of the temperatures after loading the first batch of salts

The values given by the thermocouples are recorded and sent to a PC, together with the data furnished by a Mitchell Instruments hygrometer.

2.4.3 Preliminary tests

Tests were conducted to optimize some operations to be made during the experimental campaigns. They included:

- melting of salts and metal,
- stirring of the liquids,
- collection of samples.

Figure 47. Sample of molten bismuth (~1 kg) used for preliminary tests

2.4.3.1 Melting of salts and metal

A small bismuth ingot (~1 kg) was fused both separately and together with 252 g of LiCl/KCl salt. The melting tests, conducted in a stainless steel vessel (about 10 cm dia.), were followed by visual inspection (**Figure 47**).

2.4.3.2 Stirring of the liquids

In order to ensure uniform mixing of the immiscible liquids of different viscosity, two motor-driven stirrers, each supporting a steel rod with three baffles (whose position corresponds to molten salts, salt/metal interface, and liquid metal) (**Figure 48**) were located in the mild steel vessel in such a way that the optimum homogenization of the two liquid phases was achieved. Aimed at verifying the effectiveness of the mixing system, the two stirrers were used to mix an aqueous solution of glycerine, with a viscosity at 25°C corresponding to that of the molten eutectic at 450°C (2.44 mPa·s). A small quantity of fine aluminium powder was spread over the liquid surface, to follow the motion of individual particles. The two motors were started and rotated clockwise, thus giving rise to a pattern of equipotential surfaces like those created by two electrical point charges of the same sign (**Figure 49**). In this configuration the aluminium particles were homogeneously distributed everywhere on the liquid surface.

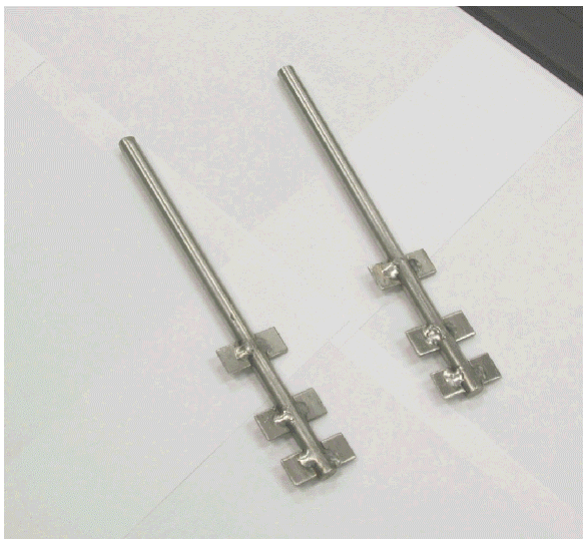

Figure 48. Pair of paddle-shaped stirrers with three baffles used for evaluating the mixing efficiency

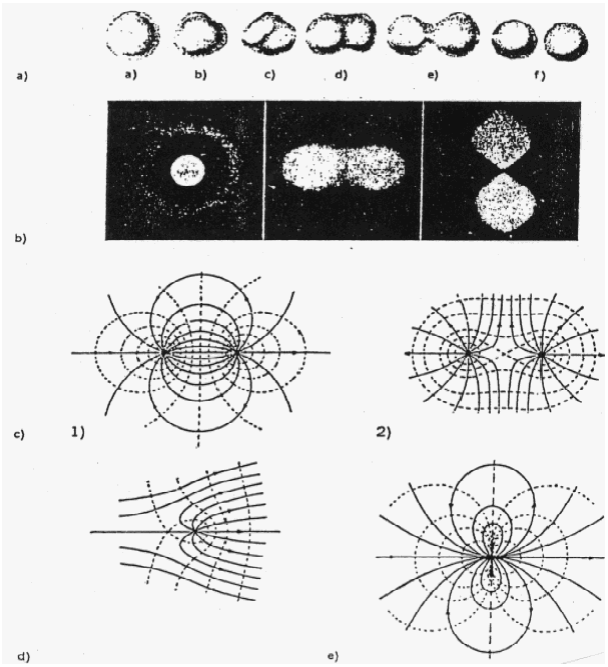

Figure 49. The pattern of equipotential surfaces originated by two electrical point charges of the same sign (Figure c2, centre right) is very similar to that created by two motor-driven stirrers both rotating clockwise. (Two stirrers rotating in opposite directions would generate two distinct regions of mixability, with a distribution of equipotential surfaces like that due to two electrical charges of opposite sign (figure c1, centre left))

2.4.3.3 Collection of samples

- Salt phase

A glass rod (8 mm dia.) was used for sampling the salt, by quickly dipping it into the salt and withdrawing it to let the salt freeze. The sample was then mechanically removed, put inside a small container, dissolved in 1N HNO_3, and sent to the analysis laboratory.

- Metal phase

The metal phase was sampled by inserting into the liquid bismuth a mild steel tube (14 mm OD, 12 mm ID) with a Poral filter (3 mm long, with a pore size of 40 μm) fitted into the lower end. The tube was preheated in the phase being sampled for a couple of minutes, then a sample was drawn into the tube by applying a vacuum to the upper end. By following this procedure the metal samples can be contaminated with salt as the tube passed through the salt. Possible sources of contamination were the salt on the outer surface of the tube or salt inadvertently collected on the filter and drawn into the tube with the metal sample. The former was minimized by carefully cleaning the outer tube surface, and the latter was minimized by using tubes having filters flush with the end of the tube, by inserting the tube through the salt as rapidly as possible, and by manipulating the valves in the proper way [80].

After sampling, the outer surface of the steel tubes was cleaned and the tubes cut into approximately 0.5 cm long sections (**Figure 50**). Only the third or fourth section of each tube, dissolved in 1N HNO_3, is submitted for analysis.

Figure 50. Section of a sample of bismuth (left) extracted from the ER by means of a tube with a PORAL filter (right) fitted in the lower end

2.4.4 Conclusions

An electrorefiner has been installed and the mechanical and electrical components, refrigeration system, vacuum system and instrumentation have been tested.

The ER was progressively loaded with both bismuth metal (26.5 kg) and LiCl-KCl (6.67 kg), which were melted and maintained at 450°C for a period enough to allow equilibration.

The functional tests performed up to now suggest some improvements and modifications to the PYREL plant, generally aimed at satisfying safety criteria and simplifying the operations.

A series of experimental chemical-electrochemical separations of metals simulating the nuclear fuel are scheduled for the next future.

Note : Poral is the name of a high-strength, porous metal material manufactured by Ugine-Carbone from metallic powders using appropriate sintering techniques. High strength results from the strong inter-grain bonding produced by sintering. Porosity results from the use of a powder as starting material. The Poral filter used in the experiments with PYREL is made of stainless steel.

2.5 Assessment of sodalite as confinement material for chloride salts containing fission products

2.5.1 Sodalite synthesis and FP incorporation study

The pyrochemical process can produce a salt waste containing Li, K and FP chlorides [81]; after several batches they accumulate in the molten salt media and therefore, become a difficult problem because of their high solubility in water. In fact it is well known that water soluble halides cannot be inertized in a glass matrix [82]. This means that the glass technology cannot be applied in the case of halide waste.

Sodalite is a natural occurring mineral that contains halide salts stably in its cage structure (**Figure 51**).

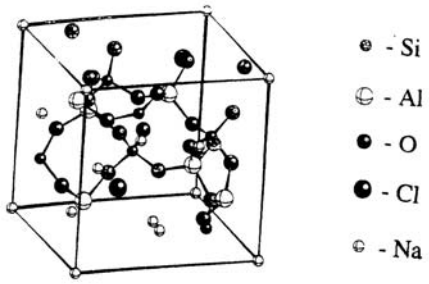

Figure 51. Cubic cell of natural sodalite

The ideal formula of natural sodalite is [83]:

$Na_8(Al_6Si_6O_{24})Cl_2$

- The synthesis of pure sodalite by hydrothermal process

Since our purpose is the preparation of several samples of pure sodalite to be used as reference materials for a further activity on the synthesis of modified sodalites, a simple method, starting from kaolinite in basic environment has been adopted [84].

Kaolinite is an aluminium silicate with the formula $Al_2Si_2O_5(OH)_4$.

Sodalite synthesis takes place in bland conditions:

NaOH 4M solution, 2 g of kaolinite, 10 g of NaCl at 80°C

Then filtration, water washing and oven drying

The assumed chemical reaction is:

$$3[Si_2\ Al_2O_5(OH)_4] + 6NaOH + 2NaCl \rightarrow Na_8(Al_6Si_6O_{24})Cl_2 + 9H_2O$$

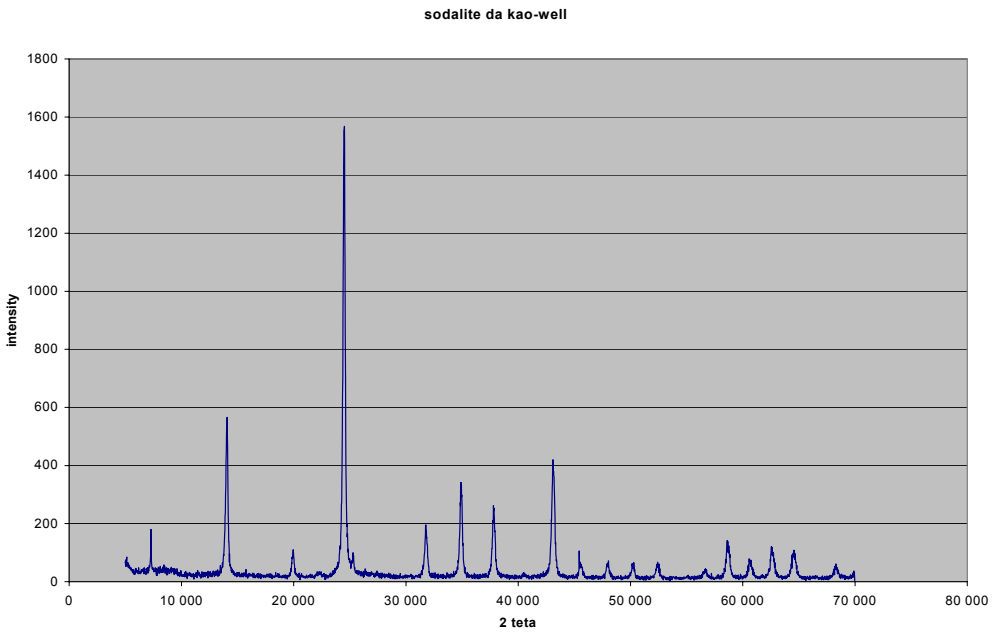

Figure 52. Sodalite from crystallised kaolinite

2.5.1.1 Sodium sodalite exchange reactions with potassium and cesium

We decided to follow the method of ion exchange of the synthesized sodalite with different cations.

KCl has been the first salt selected. The reaction was carried out in an open reactor at 800°C for 4 hours under He gas flow in order to avoid the formation of oxychlorides.

After the reaction the final product was characterized by IR and X-ray spectra. **Table XXVII** shows the IR spectra with the substitution of K for Na.

Also the hot cell X-ray test indicated an average exchange reaction up to 80% of the Na with K.

Table XXVII. IR absorption bands for the synthetic and exchanged sodalite [85], our synthetic sodalite and exchanged sodalite in the range 300–1200 cm^{-1}

Compound	Wavelength						
$Na_8(Al_6Si_6O_{24})Cl_2$	985	736	712	668	466	438	412
$Na_{5.4}K_{2.6}(Al_6Si_6O_{24})Cl_2$	985	725	701	656	456	430	401
$Na_{5.3}K_{2.7}(Al_6Si_6O_{24})Cl_2$	985	725	701	656	457	429	401
$Na_{4.2}K_{3.8}(Al_6Si_6O_{24})Cl_2$	990	720	695	652	452	426	398
$Na_{3.3}K_{4.7}(Al_6Si_6O_{24})Cl_2$	990	717	692	649	449	422	395
$Na_{2.8}K_{5.2}(Al_6Si_6O_{24})Cl_2$	995	714	689	646	446	420	394
$Na_{1.4}K_{6.6}(Al_6Si_6O_{24})Cl_2$	995	707	683	643	443	416	393
$Na_{0.4}K_{7.6}(Al_6Si_6O_{24})Cl_2$	995	703	679	640	440	412	392
Our synthetic sodalite	986	736	712	669	467	438	–
Exchanged sodalite	995	724	697	655	455	429	–

υ_{as} T-O-T (asymmetric stretching mode): 900–1200 cm^{-1}
υ_{s} T-O-T (symmetric stretching mode): 550–850 cm^{-1}
δ O-T-O (bending mode): 400–550 cm^{-1}
δ T-O-T (bending mode): < 300 cm^{-1}

Al the samples were characterized as indicated in **Figure 53**.

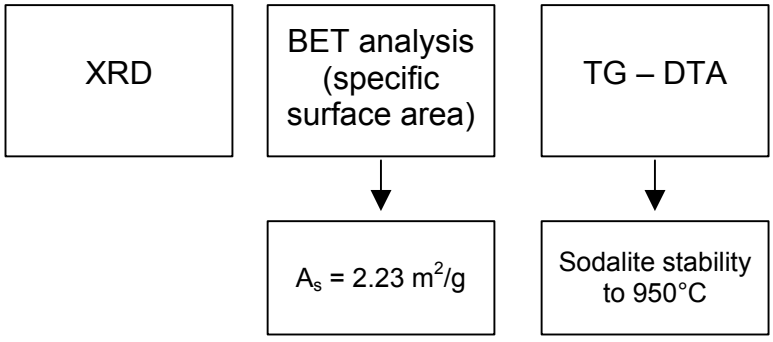

Figure 53. Sample characterization techniques

TGA analysis of the 0.3 g of sodalite and 3 g of CsCl shows total weight loss of the CsCl in the reaction temperature range (**Figure 54**).

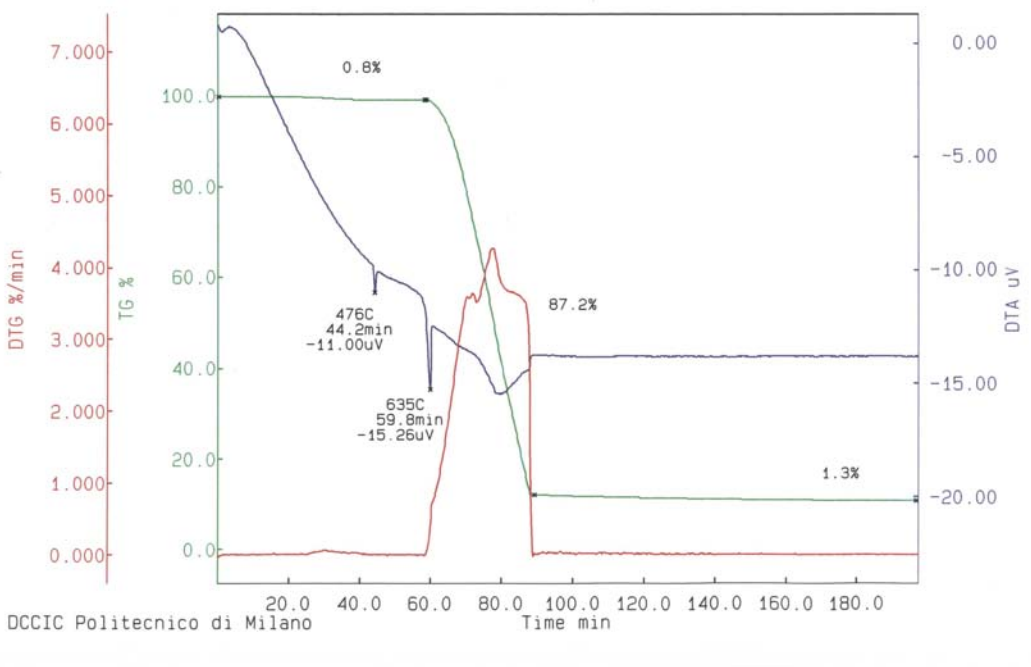

Figure 54. Thermogravimetric analysis results.

2.5.1.2 Exchange Reactions with CsCl

An exchange reaction test was conducted in a closed reactor (**Figure 55**) to prevent any salt loss.

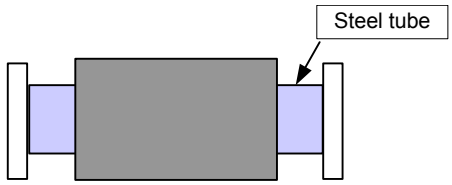

Temp: 800°C
Ramp: 7°C/min
Reaction time: 2 h
Natural cooling

Figure 55. Closed reactor for the solid exchange reactions

IR analysis revealed a clear peak shift. XRD analysis detected the formation of pollucite, an aluminosilicate with the formula $CsSi_2AlO_6$ (**Figure 56**).

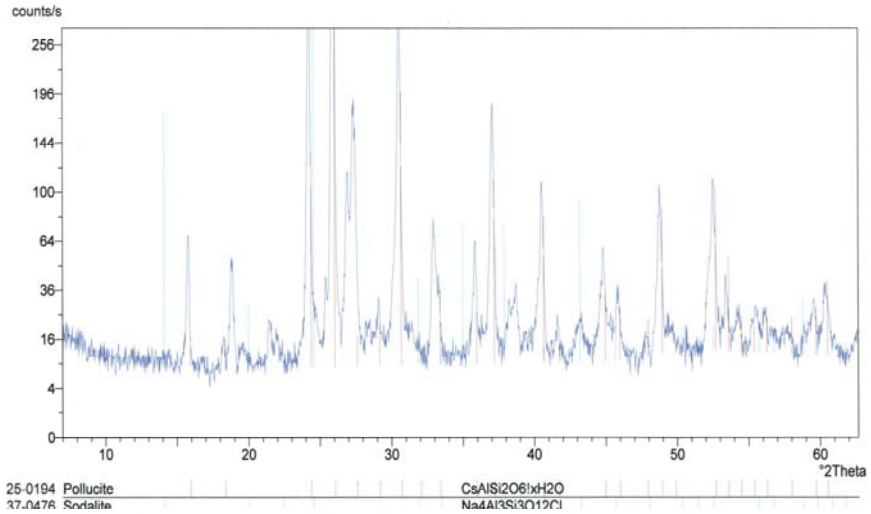

Figure 56. XRD after the reaction in a closed reactor

Pollucite is a selected mineral form of Cs [86]. Consequently in the future it will be important to verify its leaching resistance properties.

2.5.2 Leach testing of sodalite samples

2.5.2.1 Research objectives

The objective of the studies performed in collaboration with Politecnico di Milano is to assess the intrinsic stability of pure (Na) sodalite and then of substituted sodalite. The study of Na substitution addresses the possibility of incorporating other cations (e.g. Li, K, Cs, Sr, etc.) in the sodalite structure. The tests were performed by the CEA to determine the intrinsic chemical durability of the materials fabricated and characterized by Politecnico di Milano.

2.5.2.2 Test description

Several types of complementary tests can be used to assess the chemical durability of a material. Two tests were carried out [87]: a dynamic Soxhlet-mode test during which the sample was in contact with renewed pure water to measure the initial alteration rate, and a static test to measure the material mass losses under saturation conditions.

The test specimens were either powder samples (of controlled particle size to calculate the geometric surface area) or monoliths of known surface area.

Note : Accurate determination of the material surface area in contact with the solution is essential in order to determine the material-surface-area-to-solution-volume (S/V) ratio. The materials must also be characterized prior to leaching.

2.5.2.3 Characterization prior to leach testing

Three samples were supplied by Politecnico di Milano, designated SI1 for Na sodalite, SI2 for the second Na sodalite batch, and SI3 for K-substituted sodalite. In order to ensure the quality of the materials, very fine powder samples (particle size range: 1–10 μm) were characterized by the CEA during the receiving inspection.

Note : XRD and SEM analyses must be combined to determine all the phases present. The difficulty in this case was due to the very small grain size, which made quantitative SEM composition analysis impossible.

➢ SI1

XRD analysis of sample SI1 (**Figure 57**) showed that the reaction was incomplete, with a mixture of sodalite (majority phase) and kaolinite (starting material, minority phase). This sample was not submitted to leach testing, but was used instead for dilatometry tests pending receipt of the remaining samples.

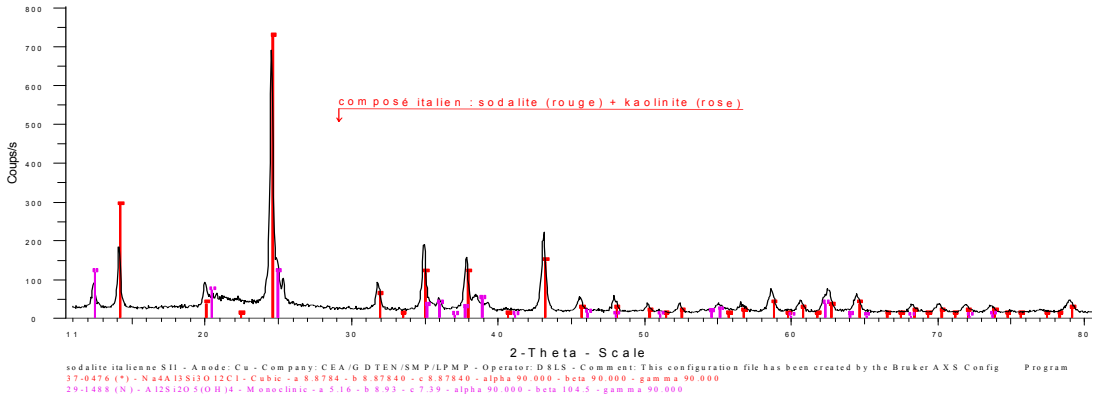

Figure 57. XRD spectrum of sample SI1

➢ SI2

XRD analysis of sample SI2—for which the synthesis time was extended from 48 hours (SI1) to 5 days—showed that the majority phase was sodalite together with quartz, most likely present in the starting materials. SEM analysis of the powder, consisting of relatively heterogeneous aggregates measuring about 60 µm (**Figure 58**) showed that the composition of the light-collared phase (revealed by EDS analysis) resembled $Na_5Al_6Si_6O_{24}Cl_1$. An apparent chlorine deficit in the material could account for a slight shift in the peaks on the XRD spectrum. Impurities were observed (arising from the initial kaolinite) and quantified by semi-quantitative chemical analysis: Ti (1.9 wt%), Fe (0.76 wt%), Ca (0.3 wt%), Sr (0.17 wt%), K (0.1 wt%), Zr (0.1 wt%).

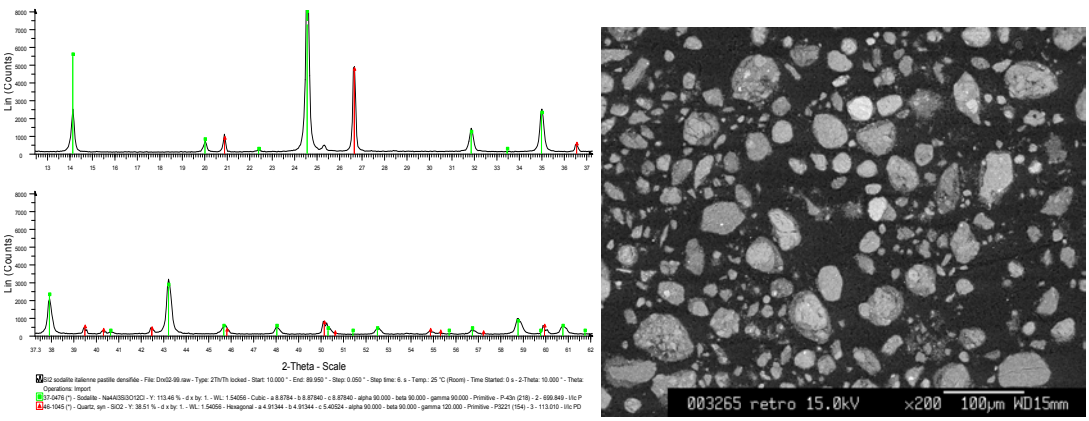

Figure 58. XRD and SEM images of sample SI2

➢ SI3

XRD analysis of sample SI3 revealed a mixture several phases: sodalite (majority phase), SiO_2 and perhaps leucite. Some peaks could not be attributed. (**Figure 59**).

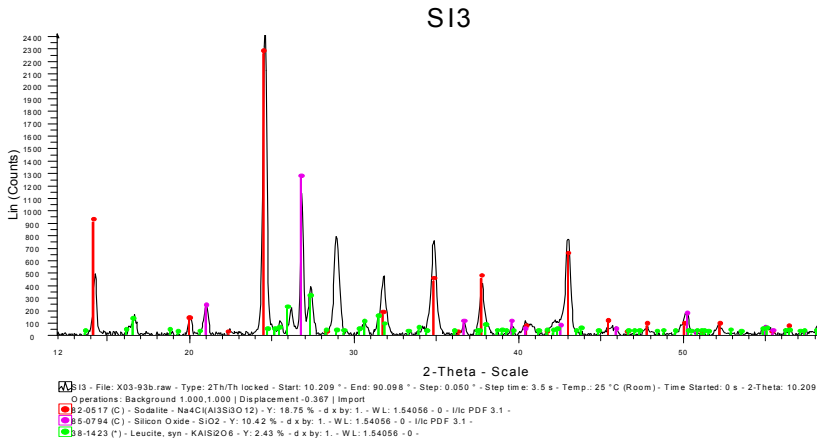

Figure 59. XRD spectrum of sample SI3

2.5.2.4 Sintering problem

Dense pellet fabrication tests were performed to allow dynamic leach testing in Soxhlet mode. The material sintering temperature was determined by thermogravimetric analysis followed by a dilatometry measurement. The tests were carried out first on sample SI1 pending arrival of the other samples, then on SI2.

The test curves revealed two transformation zones, one near 550°C and the other near 915°C, preceding the transformation from sodalite to nepheline between 950 and 1100°C. The preliminary material sintering tests were therefore specified as follows:

- After cold pressing, the pellets were submitted to a heating cycle (2°C/min) with a 5-hour residence time at 550°C; the resulting pellets exhibited poor mechanical integrity.
- The subsequent tests carried out for 5 h at 550°C followed by 5 h at 915°C. The resulting pellets were more solid and could be handled and tested but were still very fragile and very porous.

X-ray diffraction analysis was performed on a pellet sintered according to this protocol to check its composition. Sodalite was still the majority phase; a small quantity of nepheline was also observed.

Note : Published work on the densification of the materials obtained [88] uses hot pressing with high-temperature isostatic presses (HIP). This equipment is unavailable to use for fabricating pellets, but these studies would appear necessary from the standpoint of performing tests.

The K-substituted sodalite sample (SI3) was supplied by Politecnico di Milano in pellet form with roughly the same mechanical strength as obtained by the method described above. These pellets were sintered at 800°C.

2.5.2.5 Leach test results

2.5.2.5.1 Soxhlet tests

Leach testing requires an accurate determination of the sample surface area. Specific surface area measurements by the BET method were carried out on the sintered pellets: the specific surface area of the SI2 pellet was 1200 $cm^2 \cdot g^{-1}$ (measured with a krypton pycnometer), compared with 1300 $cm^2 \cdot g^{-1}$ for the SI3 pellet. These high values confirm that the pellets were very poorly densified, and also reveal the existence of open porosity. The resulting very high uncertainty on the surface area actually in contact with water increases the uncertainty on the rate expressed in $g \cdot m^{-2} d^{-1}$. In the future an effort must be made to obtain sintered pellets providing dense samples (at least 90% of the theoretical density).

- SI2

Sample SI2 was leached for 14 days in Soxhlet mode. The sample analysis results were used to plot the following elemental normalized mass loss curve (**Figure 60**).

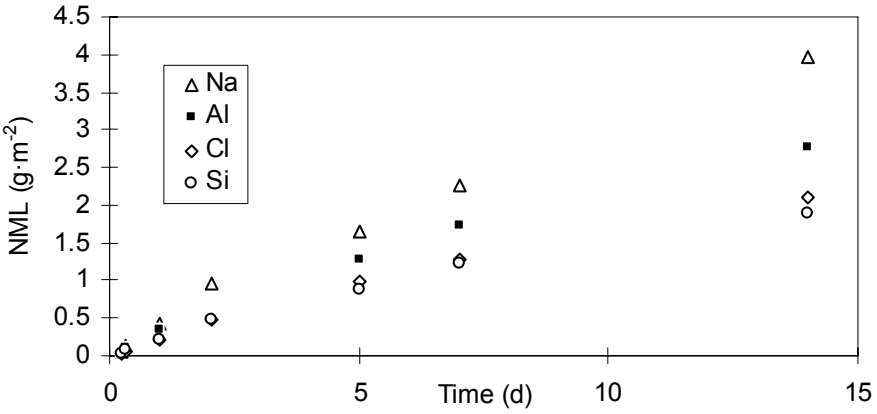

Figure 60. Normalized mass loss for SI2 pellet after 14 days

Based on the overall pellet mass loss the leach rate was about 0.16 $g \cdot m^{-2} d^{-1}$ after 14 days. The rate of release of the elements appeared to be linear. The low rate confirms the low solubility of the material under these conditions (pure water, 100°C), assuming the surface area was correctly estimated.

The leached pellet was observed by XRD. Note that on the surface the sodalite signal is no longer visible: the mineral phase corresponds to nepheline. This could be attributable to sodium and chlorine losses resulting in the stoichiometry of nepheline. When the altered layer was eliminated by polishing, unaltered sodalite was again visible.

- SI3

Sample SI3 was leached for 14 days in Soxhlet mode. The leachate sample analysis results were used to plot the following elemental normalized mass loss curve (**Figure 61**).

Based on the overall pellet mass loss the leach rate was about 0.30 $g \cdot m^{-2} d^{-1}$. Once again, assuming the surface area was exact, the rate was low. Potassium was released more rapidly than the other elements; this could be an artefact if the quantity of potassium actually incorporated in the material was less than assumed (80% of the exchangeable sites [89]).

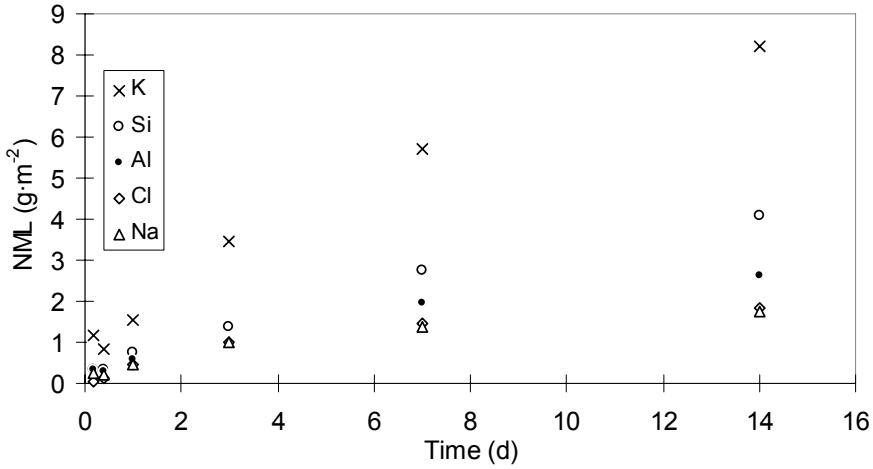

Figure 61. Normalized mass loss for SI3 pellet after 14 days

2.5.2.5.2 Savillex tests

The specific surface area taken into account was once again determined by the BET (Ar) method as 9.9 $m^2 \cdot g^{-1}$. The test conditions thus corresponded to an S/V ratio of about 6400 cm^{-1}.

The normalized mass losses were as follows:

7-day test	Na	Si	Al	Cl	pH	S/V
SI2	0.0012	0.0002	0.0006	0.0016	9.9	6450
SI2	0.0012	0.0003	0.0007	0.0016	10.14	6470

The results indicate preferential release of sodium and chlorine.

NML ($g \cdot m^{-2}$)	Si	Na	Al	K	Cl	S/V
SI3	0.0002	0.0002	0.0001	0.0013	0.0002	5887

Potassium was released at a higher rate (as for the Soxhlet tests).

Sample SI3 exhibited better performance than SI2; the normalized mass losses were lower than those measured on sample SI2 (all the powder samples were washed in the same way before testing).

Here again, with such fine powder the notion of surface area is not obvious; since the measured BET values were comparable, it may be clearer to consider instead the quantities of elements released into solution: for 0.35 g of material in 5 mL of water, the following concentrations were measured in solution after 7 days at 90°C:

mg/L	Na	Si	Al	Cl	K
SI2	147	37	74	75	
SI2	154	27	68	78	
SI3	14	18	11	10	49

These results indicate better performance by the K-substituted sodalite.

2.5.2.6 Conclusions concerning these tests

From the standpoint of the chemical durability of the materials tested, further sintering studies will be necessary to obtain low-porosity pellets and avoid measurement uncertainties regarding the surface area accessible to leaching. With dense materials it will also be possible to obtain powder samples of controlled particle size.

The Soxhlet test results indicate virtually linear release of elements from pure sodalite. The results obtained also show that under saturation conditions the cation bonded to Cl, Na or K in the sodalite structure is preferentially released. The K-substituted sodalite (SI3) exhibited better performance than SI2 for this test, but the rates are difficult to quantify and warrant confirmation. Optimizing the sample densification will be the prerequisite for obtaining data on the intrinsic chemical durability of these materials.

2.6 Conclusions of chloride media studies

- Dissolution of UO_2

An extensive study was undertaken by CIEMAT to determine the stability of the compounds formed and the reaction rates during chlorination of oxides using different chlorinating mixtures. Basic electro- and thermochemical data were used to construct potential acidity (E-pO^{2-}) diagrams for the different elements. By comparing the diagram with the E-pO^{2-} of different chlorination mixtures it was possible to predict the appropriate chlorinating mixture for RE oxides and uranium oxide.

In chlorination experiments with Ln oxychlorides and RE oxides using HCl as the chlorinating gas, the end product was RE(III) chloride and close to 100% efficiency was obtained. It was shown that different chlorination kinetics were obtained for different chlorinating mixtures, the slowest being Cl_2. The reaction rates were also dependent on the sample and surface area and on the RE oxide element.

Chlorination of UO_2 and simfuel were also carried out to investigate the chlorination of oxide fuel materials. Efficiencies higher than 90% were obtained using HCl and Cl_2+C with faster kinetics obtained for carbochlorination. The influence of particle size on direct chlorination of UO_2 is a critical parameter. The lowest particle size fraction or the highest surface area provided the highest efficiencies and dissolution rates. The dissolution behaviour of simfuel was found to be similar to that of UO_2. Dissolution rates and efficiencies are expected to be higher for irradiated materials. This indicates that direct chlorination of decladded and ground irradiated pellets should be possible with promising yields.

- Systematic electrochemical studies

Systematic electrochemical studies of rare earth elements and some actinides (U, Pu, Am) were undertaken by CIEMAT and ITU to provide basic thermochemical and kinetic data to assess electrochemical separation paths in molten chloride media. Stable oxidation states of the investigated elements under the experimental conditions were found to be (III) and (0) for Y, La, Ce, Pr, U and Pu. Oxidation state (II) also exists for Nd and Am, and oxidation state (IV) for U. Standard potentials of the different M(III)/M(0) couples were determined, and the variation of the standard potential with temperature was used to calculate some basic thermodynamic data ($\Delta G_{M(III)}$, $\Delta H_{M(III)}$ and $\Delta S_{M(III)}$ of formation). They were compared to reference state data to obtain the activity coefficient ($\gamma_{M(III)}$). Diffusion coefficients were also calculated and shown to possess temperature-dependence according to the Arrhenius law.

Electrodeposition and separation experiments were carried out in which actinides and lanthanides were deposited onto solid (W, Mo, Ni and Al) and liquid (Cd and Bi) cathodes. It was shown that the choice of cathode material onto which the actinides are deposited during electrolysis is essential. Two characteristics must be taken into account. The metallic deposit must be stable enough to prevent undesired side-reactions and the difference in reduction potentials between MA and Ln must be sufficient to allow selective electrochemical reduction of the actinides. From the basic electrochemical data obtained it could be shown that higher separation factors (actinides from lanthanides) should be obtained in the LiCl-KCl / Bi system than in the LiCl-KCl / Cd system. The selective recovery of actinides on a Bi cathode proved difficult, however, due to the small difference in reduction potentials between actinides and lanthanides. It was found that actinides (Pu and Am) form stable surface alloys with solid Al and that the difference in reduction potential onto Al is also sufficient to allow separation of MA from Ln. This was successfully demonstrated by separating Pu and Am from Nd by electrolysis on Al.

- Electrorefiners

Electrorefiners installed in shielded glove boxes were used by ITU/CRIEPI and AEA-T/BNFL for electrorefining process investigations to obtain basic knowledge of 1) anodic dissolution behaviour of the alloy, 2) recovery of U onto a solid cathode, and 3) recovery and separation of actinides into a liquid cadmium cathode. A number of rate-controlling parameters on electrorefining of An in molten LiCl-KCl eutectic were evaluated. Two main controlling parameters were identified: the concentration of the electrochemically active species in the salt and the rate at which metals enter the liquid Cd cathode. It was found that disturbing the electrode surface by using a pounder was important to prevent solid U metal forming at the liquid metal cathode surface at a greater rate than it could migrate into the bulk metal Cd. The separation factors were found to decrease as the current increased in unmixed systems.

Several electrorefining runs with unirradiated UPuZr alloy with addition of $LnCl_3$ salts or with unirradiated UPuMALn alloy were carried out using liquid Cd cathodes. Separation factors were calculated from the measured concentration of the elements in the salt and Cd phases. Typical separation factors of U, Np, Am, Cm and Ce against Pu were about 2.0, 0.95, 0.6, 0.53 and 0.04, respectively. These experiments showed that An can be effectively collected on a liquid Cd cathode and that separation of An from RE elements should be possible. However, these separation factors will be not sufficient if the objective is to recover 99.9% of the An without excessive Ln. In this case a significant quantity of Ln will be carried away with the An so another separation step upstream or downstream will be necessary to achieve the objective.

- Salt cleanup (AEA-T/BNFL)

  Li/Cd alloy was shown to remove all Ln and An chlorides from the salt. Use of a Cd/Li cathode was only partially successful because of reactions of Li with chlorides competing with anodic oxidation.

- Assessment of sodalite as a containment material for chloride salts

  - Sodalite synthesis (ENEA, POLI Milano)

    Chloride salt waste containing FP may arise from pyroreprocessing of spent fuel. Sodalite ($Na_8[(Al_6Si_6O_{24})]Cl_2$) has been proposed by several teams as a possible conditioning material for such waste. To assess the quality of this material, pure sodalite was prepared by a hydrothermal method, starting with natural kaolinite according to the following reaction:

    $$3[Si_2Al_2O_5(OH)_4] + 6NaOH + 2NaCl \rightarrow Na_8(Al_6Si_6O_{24})Cl_2 + 9H_2O$$

    Electron micrographs confirmed the much greater crystallinity of the resulting sodalite compared with the initial kaolinite.

    Exchange reaction tests were carried out with pellets containing a blend of sodalite and excess KCl or CsCl at 800°C for 2 hours under helium flow. Ion exchange from Na to K was demonstrated by the IR spectra compared with published spectra. The cesium ion exhibits greater difficulty in entering the sodalite lattice by ion exchange.

    A similar exchange experiment was carried out using a pressurized reactor to prevent any salt loss. IR analyses revealed a clear peak shift. XRD analysis detected the formation of pollucite, an aluminosilicate with the formula $CsSi_2AlO_6$.

  - Solid-state synthesis of sodalite

    Koyama's method was used starting from $NaAlO_2$, SiO_2 and LiCl/KCl for 108 hours at a constant temperature of 800°C. Sodalite formation was detected but other phases were present, especially nepheline.

  - Leaching tests on sodalites (CEA)

    Leaching tests on materials prepared by ENEA-PoliMi were carried out at CEA Marcoule. On completion of these tests, some data were obtained on the behavior of pure and K-substituted sodalites. Two different leaching tests were carried out: Soxlhet tests, which measure an initial rate of alteration, showed quasi-linear release of the elements in solution for pure sodalite. The initial alteration rates measured were between 0.16 $g \cdot m^{-2} d^{-1}$ and 21 $g \cdot m^{-2} d^{-1}$ for pure sodalite, according to the surface area considered (BET surface area or very conservative geometrical surface area). The initial alteration rate for the K sodalite was between 0.30 and 32.8 $g \cdot m^{-2} d^{-1}$. The uncertainties concerning the actual surface area in contact with water, which can be very high for pellets with such open porosity, is responsible for these wide ranges of values. This underlines the importance and necessity of further work on pellet densification, to allow accurate measurement of the alteration rate.

3 General studies

3.1 Electrochemical cell modeling

3.1.1 Introduction.

The objective of this task was to elaborate electrochemical models to describe the electrorefining process.

The models initially developed described the electrochemical behaviour of a solid-anode solid-cathode electrorefiner in steady-state conditions, namely over infinite time. We have developed new FEM models describing a liquid-anode solid-cathode electrorefiner in unsteady time-dependent conditions.

Two model have been developed: the first describes constant current working condition and the other the constant cathode-potential working mode.

The models do not take into account stirring effect, so they describe only a diffusive process.

The models were developed using the FASTFLO code, a general-purpose FEM code capable of solving partial differential equations using a programming macro language named Fasttalk.

3.1.2 The Mathematical model

Ion motion in the electrolyte is described by the following equations [29,90]:

$$\frac{\partial n^{\pm}_i}{\partial t} + \vec{\nabla} \cdot \vec{J}^{\pm}_i = 0 \qquad \textbf{(25)}$$

$$\vec{J}^{\pm}_i = D_i \frac{Z_i F}{RT} n_i^{\pm} \vec{E} - D_i \vec{\nabla} n_i^{\pm} \qquad \textbf{(26)}$$

where:

$\vec{\nabla}$ is the "gradient" differential operator;

$n^{\pm}_i$ is the *i*th ionic concentration within the electrolyte (mol·cm^{-3});

$\vec{J}^{\pm}_i$ is the molar flow (mol·cm^{-2}sec^{-1});

D_i is the diffusion coefficient of the ionic species (cm^2·sec^{-1});

$\vec{E}$ is the electrical field within the cell (V·cm^{-1});

F is the Faraday constant (96485 C·mol^{-1});

Z_i is the ionic valence;

T is the absolute temperature (K)

R is the molar gas constant (8.314 J·mol^{-1}K^{-1})

The electric field $\vec{E}$ is calculated by solving the Poisson equation for the potential:

$$\vec{\nabla} \cdot \vec{\nabla} V = 0 \quad \textbf{(27)}$$

These equations suppose the total charge conservation within the electrolyte, namely:

$$\sum_i Z_i n^{\pm}{}_i = 0 \quad \textbf{(28)}$$

The motion of neutral species within the liquid anode is described by the following equations

$$\frac{\partial n_i}{\partial t} + \vec{\nabla} \cdot \vec{J}_i = 0 \quad \textbf{(29)}$$

$$\vec{J}_i = -D_i \vec{\nabla} n_i \quad \textbf{(30)}$$

The relationship between the molar fluxes and the electric current density are given by the equation:

$$\vec{i}_i = Z_i F \vec{J}_i \quad \textbf{(31)}$$

The total electrode current is given by:

$$\int_{S_e} \sum_i \vec{i}_i \cdot \vec{\nu} dS_e \quad \textbf{(32)}$$

where S_e is the electrode surface and $\vec{\nu}$ is the normal to that surface.

3.1.2.1 Boundary conditions.

The boundary conditions of the problem are summarized in the following way:

- Poisson equation (3)

$$V\big|_{S_a} = V_{anode} \text{ and } V\big|_{S_c} = V_{cathode} \quad \textbf{(33)}$$

where S_a and S_c are respectively the anode surface and the cathode surface.

$$\vec{\nu} \cdot \vec{\nabla} V\Big|_{In} = 0 \quad \textbf{(34)}$$

on the nonconducting boundaries ($\vec{\nu}$ is the geometrical normal to those surfaces).

- Diffusion equation within the electrolyte

$$Z_i F \left(D_i \frac{Z_i F}{RT} n_i^{\pm} \vec{\nu} \cdot \vec{E} - D_i \vec{\nu} \cdot \vec{\nabla} n_i^{\pm} \right)\Bigg|_{S_c} = i_{B-V,cath} \quad \textbf{(35)}$$

$$Z_i F \left(D_i \frac{Z_i F}{RT} n_i^{\pm} \vec{\nu} \cdot \vec{E} - D_i \vec{\nu} \cdot \vec{\nabla} n_i^{\pm} \right)\Bigg|_{S_a} = i_{B-V,anod} \quad \textbf{(36)}$$

where S_a and S_c are respectively the anode surface and the cathode surface and i_{B-V} is the Butler-Volmer current given by

$$i_{B-V,cath} = Z_i F k_{cathod,i} \left\{ \gamma_i^+ n_i^+ \exp\left(-\frac{\alpha_{i,cath} Z_i F}{RT} (V_{cathode} - E_{0,i}) \right) - \exp\left(\frac{(1-\alpha_{i,cath}) Z_i F}{RT} (V_{cathode} - E_{0,i}) \right) \right\} \quad \textbf{(37)}$$

$$i_{B-V,anod} = Z_i F k_{anod,i} \left\{ \gamma_i^0 n_i^0 \exp\left(\frac{(1-\alpha_{i,anod}) Z_i F}{RT} (V_{anode} - E_{0,i}) \right) - \gamma_i^+ n_i^+ \exp\left(-\frac{\alpha_{i,anod} Z_i F}{RT} (V_{anode} - E_{0,i}) \right) \right\} \quad \textbf{(38)}$$

where:

γ_i^+ is the activity coefficient of ionic species in the molten salt,

γ_i^0 is the activity coefficient of the neutral species in the liquid anode

$E_{0,i}$ is the standard potential (V)

$\alpha_{i,electrode}$ are the symmetry factors of the redox reactions

$k_{electrode,i}$ are the transfer-rate coefficients of the redox reaction at the electrodes ($cm \cdot s^{-1}$)

The quantities appearing into the previous relationships must be considered calculated at the interfaces. The Butler-Volmer equation can be considered as a difference between two currents: a current of reduction, identified by the minus sign within the argument of the exponentials, and an oxidative current. In the calculations that follow, the reductive contribution of the Butler-Volmer equation at the anode surface has been neglected for simplicity, due to its very low value and to reduce the time of iterative calculations, but it is possible to take into account the global anode expression. Moreover the sign of B-V currents are chosen coherently with the physical meaning, namely the cathodic reduction current and the anodic oxidation current are positives.

- Diffusion equation within the liquid anode

$$Z_i F \left(-D_i \vec{\nu} \cdot \vec{\nabla} n_i^0 \right)\Big|_{S_a} = i_{B-V,anod} \quad \textbf{(39)}$$

on the anode-molten salt interface from anode side, and

$$\left(\vec{\nu} \cdot \vec{\nabla} n_i^0 \right)\Big|_{In} = 0 \quad \textbf{(40)}$$

elsewhere.

3.1.2.2 Time discretisation

Because the Fastflo code is not intrinsically structured for solving eq (**25**) as a function of time, we have discretised that equation in the following way:

$$\frac{n_i(t+\delta t) - n_i(t)}{\delta t} + \vec{\nabla} \cdot \vec{J}_i(t+\delta t) = 0 \quad \textbf{(41)}$$

where δt is the calculus time step.

3.1.2.3 The iterative algorithms

The iterative algorithms used to model the electrorefining process under constant current control and cathodic potential control are indicated in **Figure 62** and **Figure 63**, respectively.

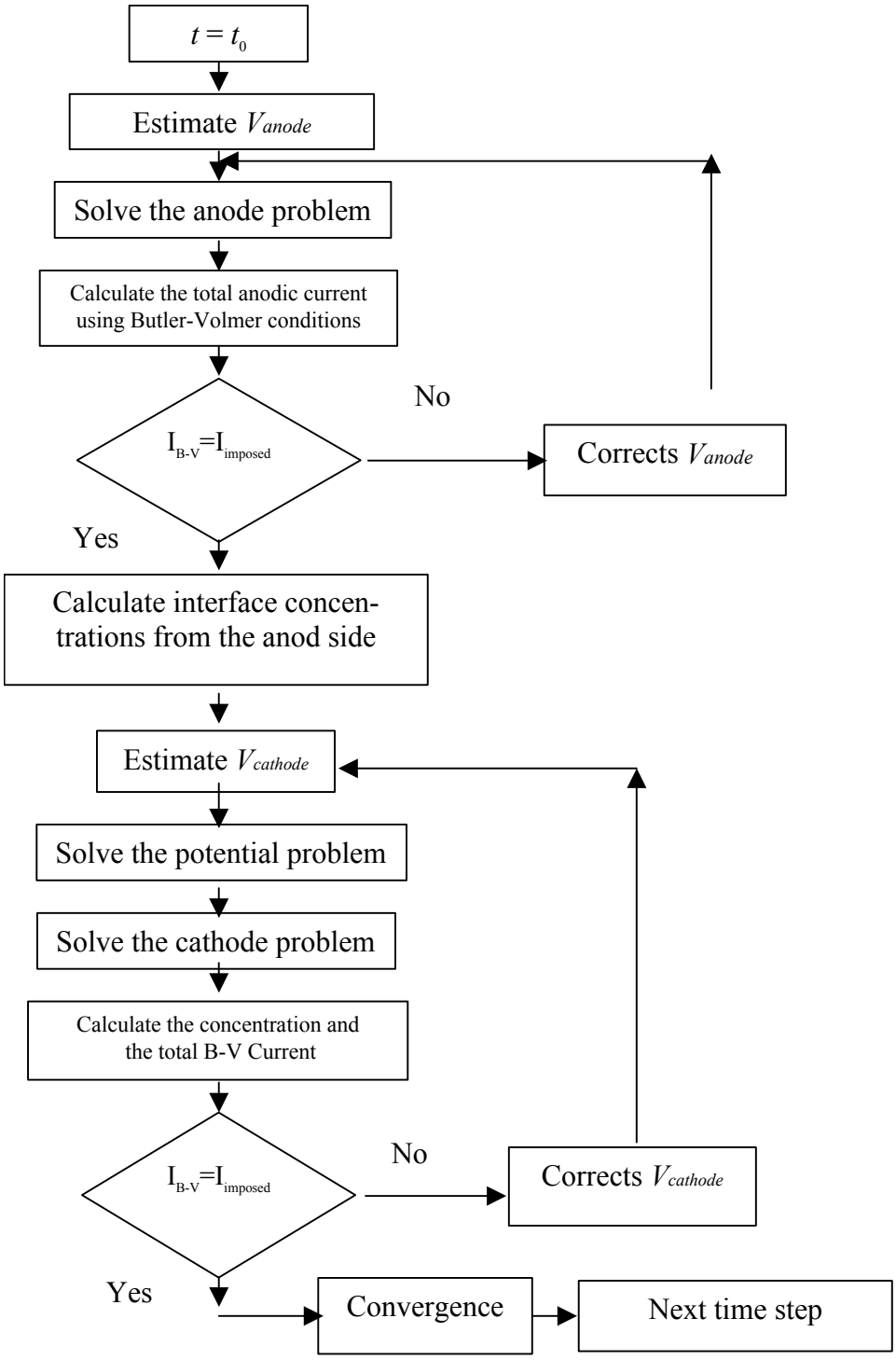

Figure 62. Flow sheet of the controlled current process algorithm

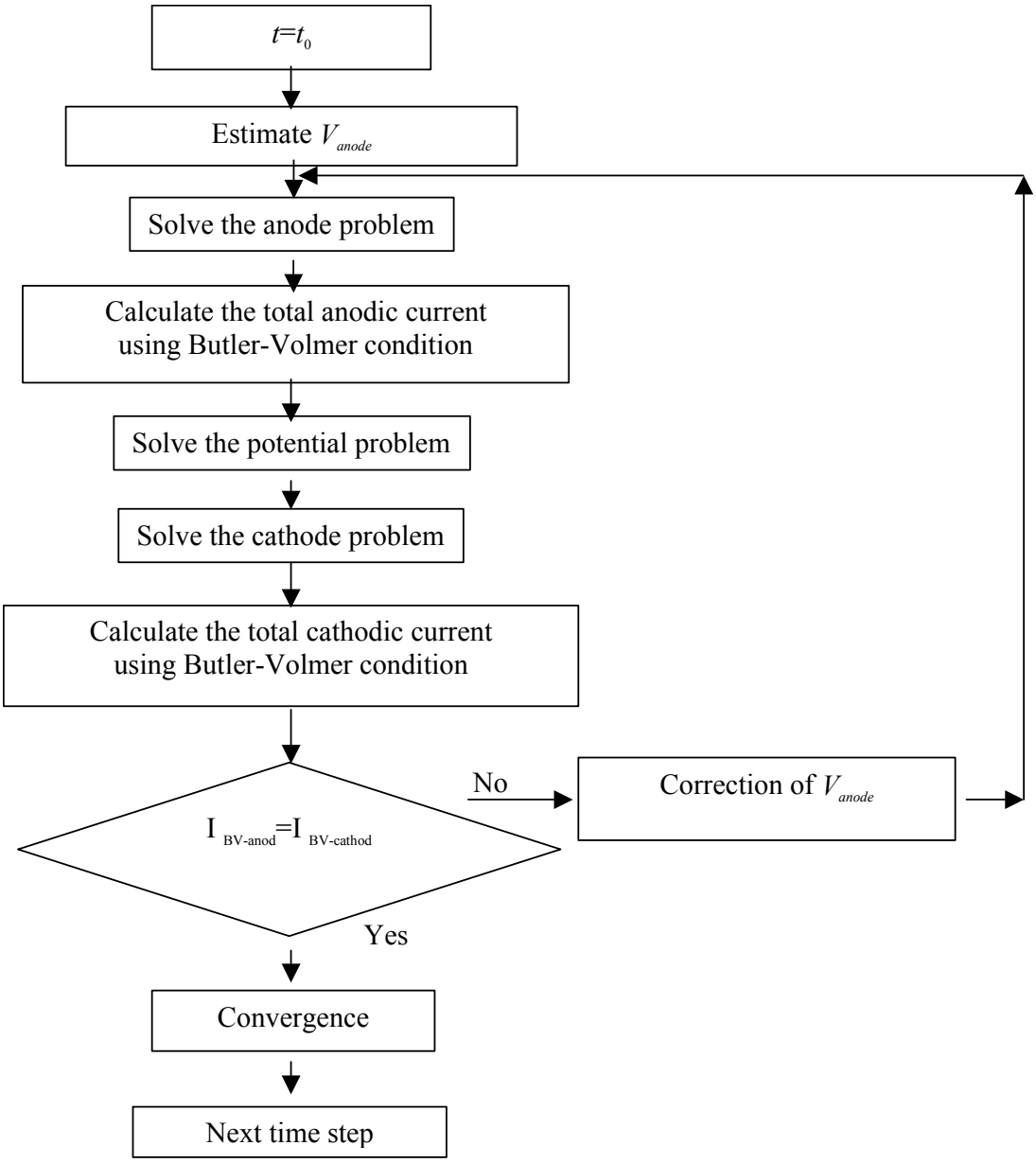

Figure 63. Flow sheet of the cathodic potential control process algorithm

3.1.3 Example of application

We apply the models to the description of an electrorefining process of U, Pu and Am in Li-KCl eutectic with solid cathode and liquid cadmium anode. The geometry of the electrorefiner was chosen from the literature [91] and is shown in **Figure 64**.

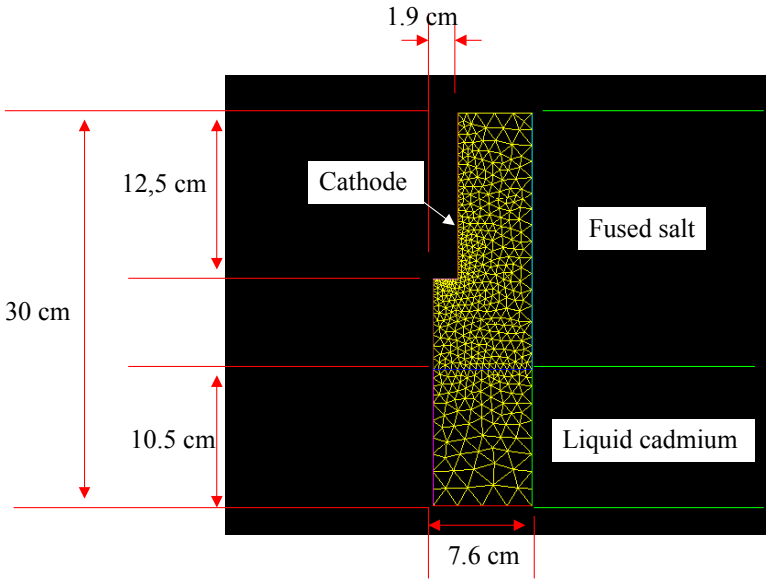

Figure 64. Electrorefiner scheme and integration meshed domain

The applied boundaries condition are shown in **Figure 65** and **Figure 66**.

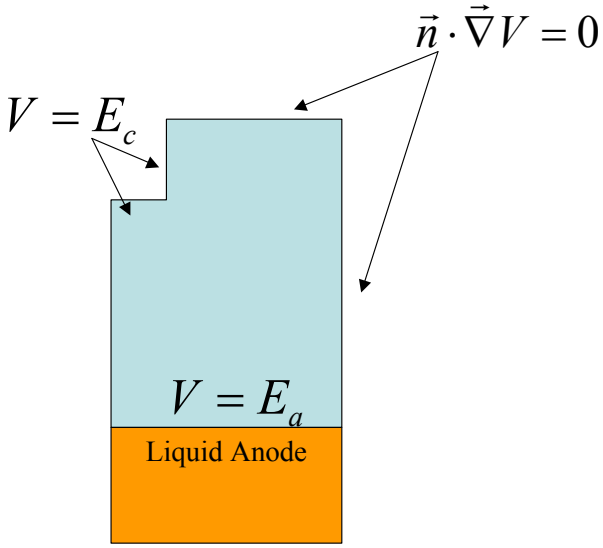

Figure 65. Boundary conditions for the potential equation

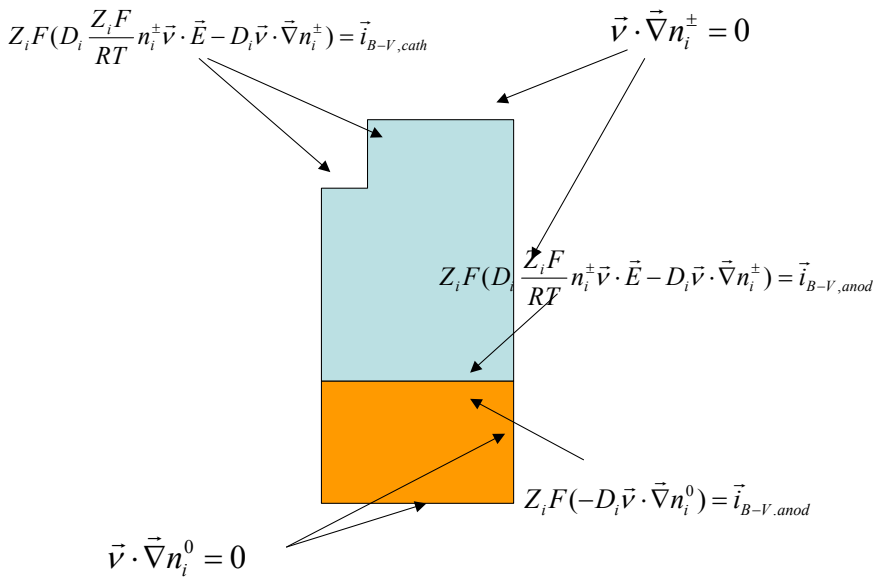

Figure 66. Boundary conditions for ionic and neutral species

The following redox reactions are taken into account:

- Chemical reactions at the anode:
$$\begin{cases} U \rightarrow U^{3+} + 3e \\ Pu \rightarrow Pu^{3+} + 3e \\ Am \rightarrow Am^{2+} + 2e \end{cases}$$
- Chemical reactions at the cathode:
$$\begin{cases} U^{3+} + 3e \rightarrow U \\ Pu^{3+} + 3e \rightarrow Pu \\ Am^{2+} + 2e \rightarrow Am \end{cases}$$

The constant values used in the calculation are given in **Table XXVIII**.

Table XXVIII. Constant values used in the calculations at 450°C

Element	D (cm^2·s^{-1}) × 10^{-5}		γ		K (cm·s^{-1})		Standard potential (V)
	Salt	Cd	Salt	Cd	Cathode	Anode	
U	0.756	1.5	4.55 × 10^{-4}	59	1.0 × 10^{-6}	1.0 × 10^{-8}	-1.233
Pu	1.65	3.0	3.5 × 10^{-3}	1.5 × 10^{-4}	1.0 × 10^{-6}	1.0 × 10^{-8}	-1.5508
Am	1.65	3.0	1.95 × 10^{-3}	1.5 × 10^{-4}	1.0 × 10^{-6}	1.0 × 10^{-8}	-1.592

The diffusion coefficient of uranium and plutonium ion in the fused salt was taken from reference [92]; the activity coefficients were taken from reference [93]. Values of the same quantities in liquid cadmium and standard potential are from reference [94].

3.1.4 Calculation results

The code calculates the concentration profile within the integration domain for each time step. The following figures illustrate concentration profiles within the liquid cadmium and the fused salt.

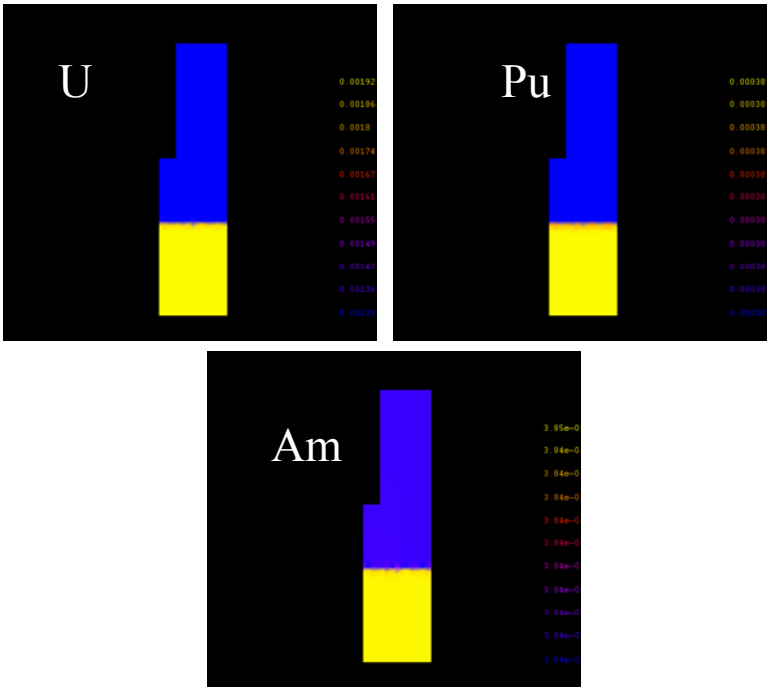

Figure 67. U, Pu and Am concentration within the liquid cadmium after 1 hour. Applied constant current 2 A, initial concentration in Cd: U=2.5 at%, Pu = 0.5 at%, Am=0.005 at%. Initial concentration in fused salt: U=5 at%, Pu=1 at%, Am=0.1 at%.

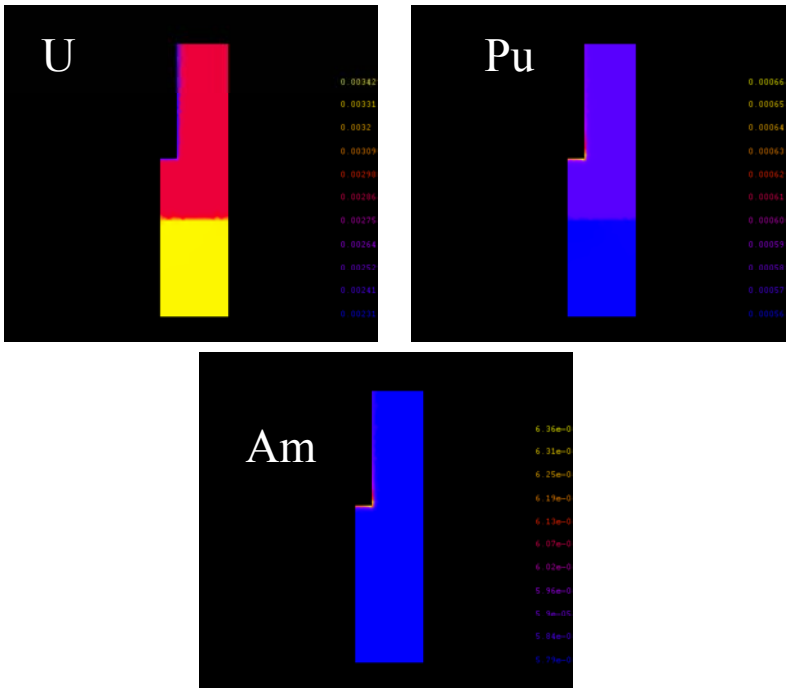

Figure 68. U, Pu and Am concentration within the eutectic after 1 hour. Applied constant current 2 A, initial concentration in Cd: U=2.5 at%, Pu = 0.5 at%, Am=0.005 at%. Initial concentration in fused salt: U=5 at%, Pu=1 at%, Am=0.1 at%.

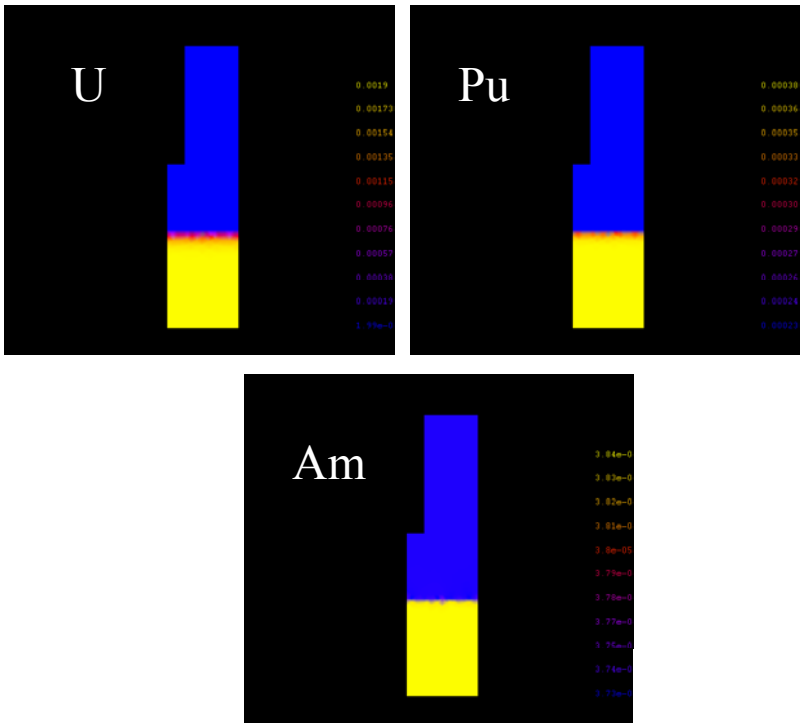

Figure 69. U, Pu and Am concentration within the liquid cadmium after 12 hours. Applied constant current 2 A, initial concentration in Cd: U=2.5 at%, Pu = 0.5 at%, Am=0.005 at%. Initial concentration in fused salt: U:5 at%, Pu=1 at%, Am=0.1 at%.

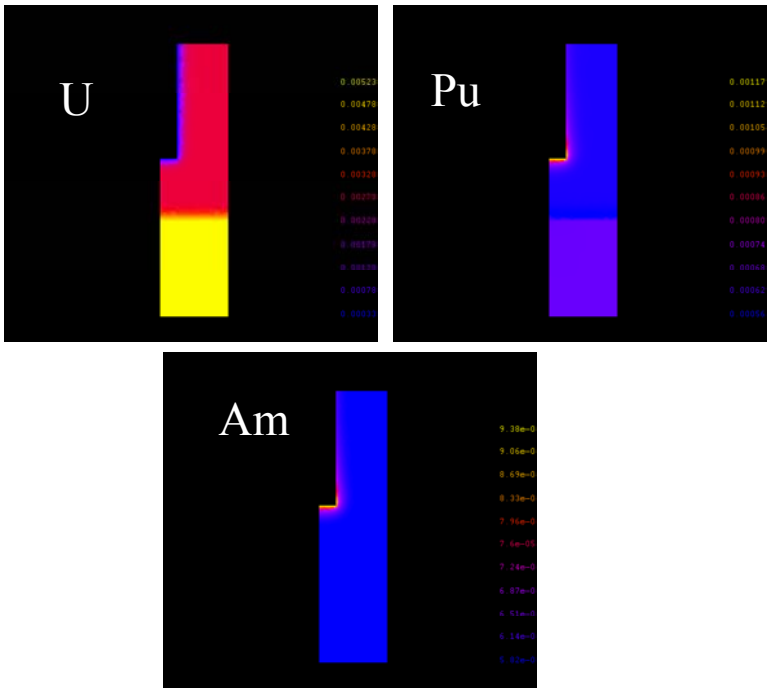

Figure 70. U, Pu and Am concentration within the eutectic after 12 hours. Applied constant current 2 A, initial concentration in Cd: U=2.5 at%, Pu = 0.5 at%, Am=0.005 at%. Initial concentration in fused salt: U=5 at%, Pu=1 at%, Am=0.1 at%.

These figures reveal the depletion of the liquid cadmium over time, the uranium depletion of the near cathode zone due to the deposition and the segregation of plutonium and americium near the cathode due to the presence of the electric field and the near absence of deposition.

The following figures show the evolution of the process parameter over time in the constant current mode and in the constant cathode potential mode.

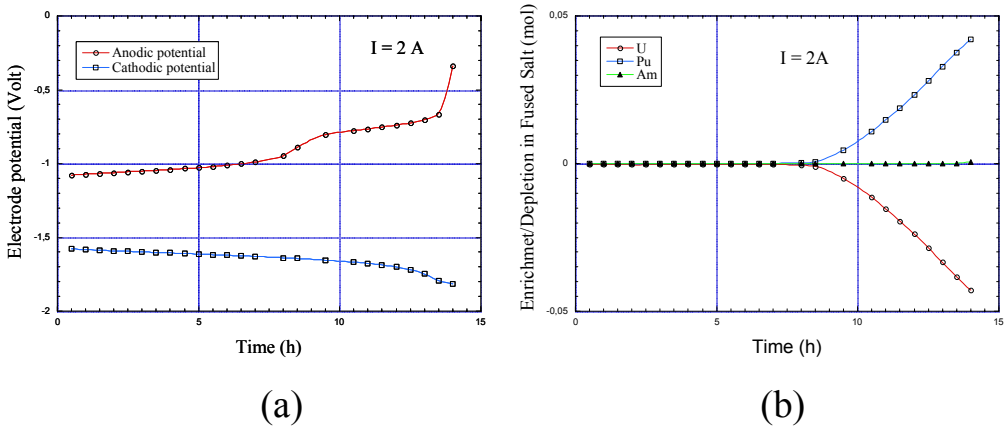

Figure 71. Time evolution of electrode potential (a) and Pu and Am enrichment and U depletion of the fused salt (b) in the constant current mode

Other quantities are calculated by the code: the interface concentrations, the molar flow toward the cathode, the depletion within the liquid cadmium.

The same happens in the constant cathodic potential mode.

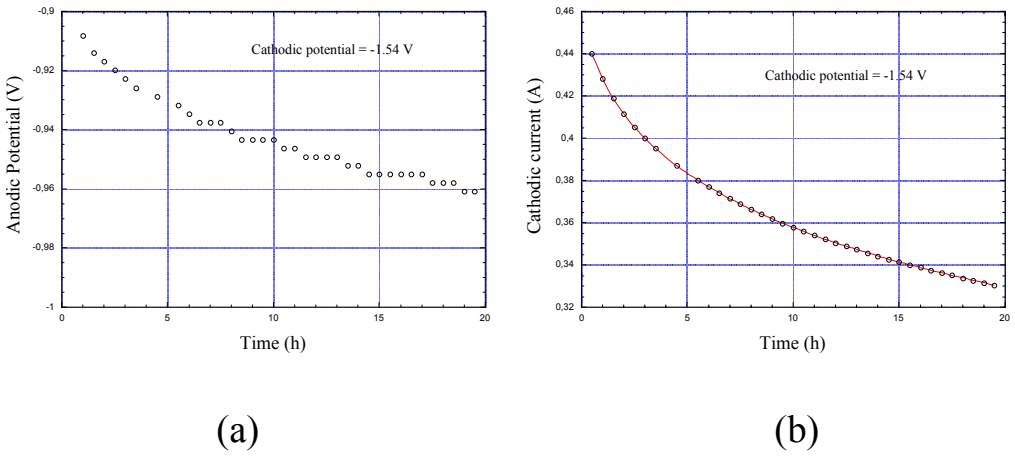

Figure 72. Time evolution of anodic potential (a) and current (b) for a fixed cathodic potential

3.1.5 Conclusion

The developed models describe correctly the phenomenology of the electrorefining diffusive processes. It is possible to model the behaviour of different ionic species as a function of time in different fused salt and liquid anodes. It is possible to study geometrical effects such as the device dimensions or the shape dimensions of the electrodes.

With the same technique it is possible to consider electrorefining processes with liquid cathodes.

The model will be implemented to take into account stirring effect by solving the Navier-Stokes equations and to take into account advective terms in eq (**25**) that were not considered in the present work.

The codes will be validated using data coming from Pyrel apparatus constructed by ENEA.

3.2 System studies

3.2.1 Objectives

The primary objective is to assess and compare what could be the industrial performance of some pyrochemical processes with regard to segregation factors, decontamination factors, final product compositions and characteristics, recycling of reactants, and waste characteristics (gas, liquid and solid flows).

3.2.2 Methodology

The main feature of the selected processes is that they allow group separation of all the actinides (from U to Cm). Three cycles compatible with this feature were initially considered for joint CEA-ENEA scenario studies: homogeneous recycling, double component, and double strata scenarios (**Figure 73**). The results obtained for the third scenario are discussed here in greater detail than for the other scenarios. This is consistent with the decision by the ADOPT committee, in the context of separation studies cofinanced by the European Commission, to favour a double strata scenario with a second stratum consisting of an ADS reactor using oxide fuel.

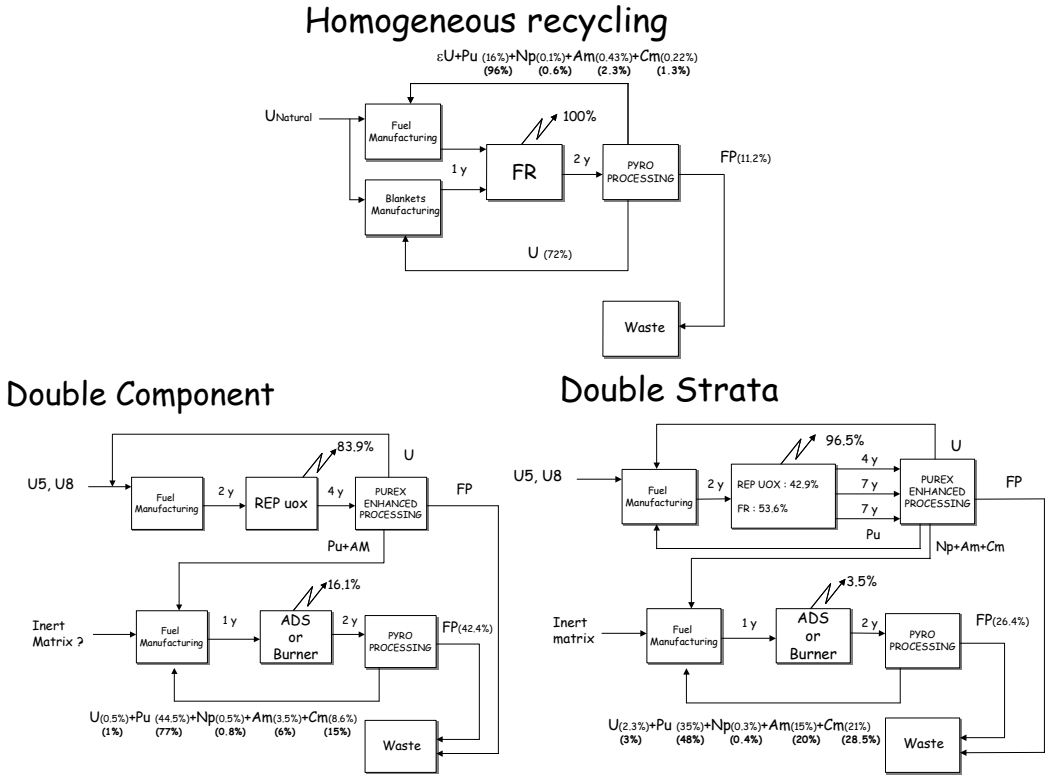

Figure 73. Scenarios

With these scenarios, pyrochemical reprocessing is applicable to a diminishing fraction of the fuel from the installed reactor population. This implies that the material flows passing through the pyrochemical reprocessing facilities will be very different: **Table XXIX** compares the total energy (TWhe), fuel flows and heavy nuclei flows for each scenario.

Table XXIX. Mass flows for each scenario

Scenario	Homogeneous recycling (100%)		Double component (16%)		Double strata (3.5%)	
Total energy (TWh_e) produced by pyrochemically reprocessed fuel	400		64.4		14	
Mass flow in reprocessing plant	kg/year	kg/day	kg/year	kg/day	kg/year	kg/day
U	2.8E+05	1382	6.6E+01	0	1.1E+02	1
Pu	6.2E+04	308	6.1E+03	31	1.8E+03	9
MA	2.9E+03	14	1.7E+03	9	1.8E+03	9
Heavy metal	3.4E+05	1704	7.9E+03	40	3.7E+03	19
FP	4.3E+04	216	5.8E+03	29	1.3E+03	7
Total	3.8E+05	1920	1.4E+04	69	5.1E+03	25

For each process studied the following points will be developed:

- Bloc diagram identifying each elementary process step
- Description of each elementary step
- Flux calculation
- Assessment of releases and waste.
- Assessment of the size of the active part of a facility dedicated to processing. The capacity of this facility would be set to process the fuel either from a 400 TWhe installed reactor base (centralized processing), or from a 20 TWhe group of reactors. Hypothesis of yearly working time for the plant: 24 hours a day, 200 days a year
- Qualitative assessment of the maturity of each process.
- Qualitative assessment of technological implementation difficulties of the whole process.

3.2.3 Salt/metal exchange process: fluoride salt

3.2.3.1 Objective

The objective of this system study is to assess the potential performance in the fuel cycle of a pyrochemical reprocessing process based on reductive salt/metal extraction.

3.2.3.2 Process description

The process flowsheet has not been optimized, but is proposed as an example of a plausible scheme based on the current state of knowledge in 2001-2002. The flowsheet is consistent with studies carried out by the CEA under the PYROREP contract and, together

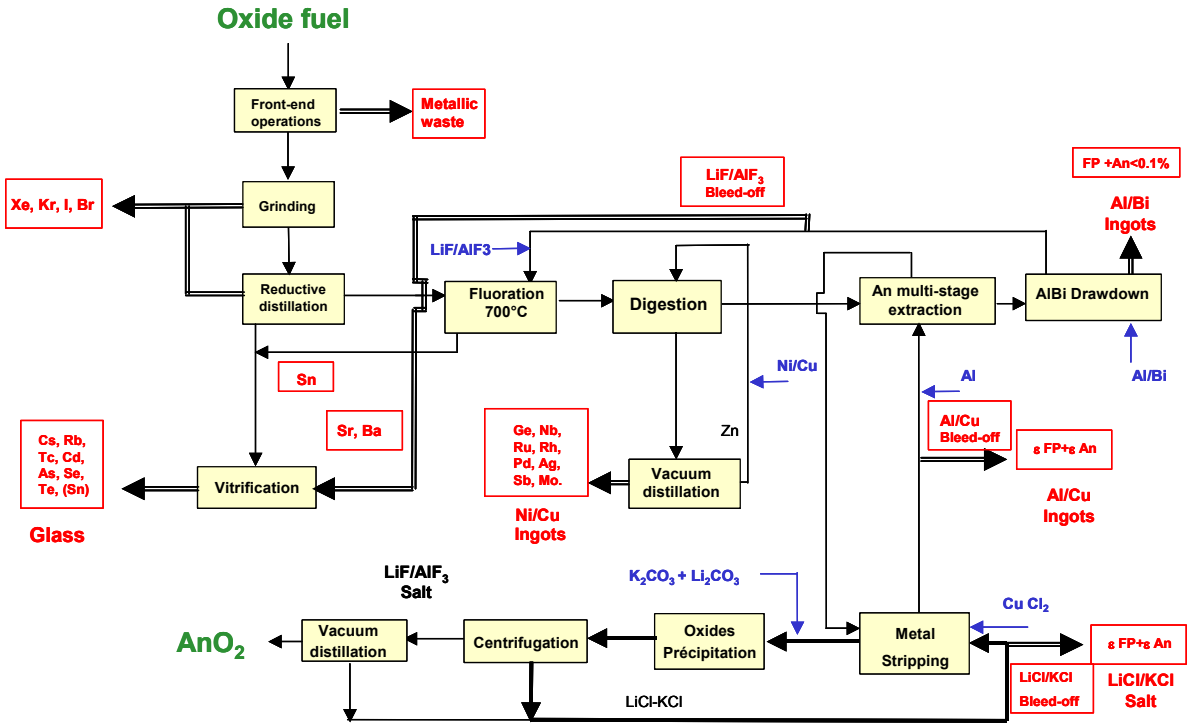

Figure 74. Process block diagram

with the work done in the same area by ENEA and NRI, covers a wide range of different processes.

We have intentionally limited this analysis to oxide fuel. A complete process (**Figure 74**) was devised around a core process ensuring the separation of the actinides from the fission products by reductive extraction. The other steps were either conceived or adapted from prior CEA work, from published reports, or on the basis of thermodynamic considerations.

➢ Mechanical treatment

The process begins with a series of head-end stages during which the fuel assemblies are chopped, decladded and ground to obtain an oxide powder that is fine enough (50-100 µm) for the subsequent reductive distillation and fluorination steps. The main difficulty of this step is to limit material losses entrained with the hulls.

During these operations some or all of the gaseous or volatile fission products (Kr, Xe, I, Br) are released and must be collected, trapped for disposal as an ultimate wasteform.

➢ Heat treatment and fluorination

The resulting powder undergoes the following successive treatments:

- Distillation at high temperature (above 1000°C) in controlled atmosphere (argon with 5% hydrogen); during this treatment all the cesium, rubidium and tellurium are volatilized; the platinum-group metals, molybdenum, nickel and a fraction of the iron (corrosion elements) are reduced to metals; some or all of the Tc, Cd, As, and Se are also volatilized [95,96].
- Fluorination with HF to avoid fluorinating some elements to oxidation state VI, at which their fluorides are volatile.

- Dissolution in a $LiF\text{-}AlF_3$ salt phase

  After the fluorination step the powder is contacted and dissolved at 830°C in a molten salt flow with a composition selected to obtain the required extraction performance (see paragraph 3.2.3.3).

- Digestion of platinum-group metals and noble metals

  The fluorinated powder is placed in contact with a mildly reducing metal phase containing zinc alloyed with copper and nickel. The platinum-group metals and molybdenum are reduced to the metal state and dissolved together with the noble metals (Sb, and possibly Ge and Nb) in the metal phase [95].

  Zinc is then recycled by vacuum evaporation; the extracted elements remain in the Ni/Cu matrix.

- Group extraction of the actinides

  The fluorides are contacted with a metallic Al/Cu phase in which aluminium is used as the reducing metal. During this stage almost all the actinides are extracted, together with a small fraction of the fission products present in the salt (see paragraph 3.2.3.4). A high actinide recovery yield and satisfactory fission product decontamination performance require a multistage extraction system and suitable salt and metal flow settings (see paragraph 3.2.3.6).

- Recovery of the actinides and preparation of finished products

  The extracted actinides and FP dissolved in the metal phase are transferred to a LiCl-KCl salt phase by oxidizing stripping using $CuCl_2$. The actinides are then precipitated as oxides by a lithium carbonate/potassium carbonate mixture; the salt and oxide are separated by filtration or centrifugation followed by low-pressure distillation of the trace quantities of entrained salt.

- Salt and metal flow management

  In order to minimize the waste flows, the salt and metal flows are managed in loops. Loop management requires online adjustments to maintain a constant loop composition and holdup. This generates drainage flows representing sources of actinide leakage and FP discharge.

  An alternative in which the LiF/AlF_3 loop is decontaminated by an Al/Bi metal phase was also considered. In this case, the Al/Bi flow is the main FP discharge vector. The aluminium composition must still be adjusted in the salt loop, however, and this adjustment is the main discharge route for the alkaline-earth elements (Sr-Ba) which are not eliminated from the salt during decontamination by the Al/Bi metal phase.

3.2.3.3 Modeling

The process was simulated on an Excel spreadsheet. At each step in the process a transfer function was assigned to each element in the initial fuel composition. A simplified model of the extraction step was constructed using the Kremser relation.

The performance of the extraction step was measured by two quantities:

- the actinide recovery yield, with a target value of 99.9%;
- the fission product decontamination factor, with the objective of recycling with the actinides less than 5% of the total initial negative reactivity due to the FP in the spent fuel.

In order to estimate the second quantity, each fission product element had to be taken into account at each process step, and the isotopic spectrum of the initial fuel was applied to the inventory accompanying the actinides to calculate the negative reactivity supplied by each FP isotope.

The isotopic composition data were also used to calculate the thermal and radioactive characteristics of all the process flows, and in particular the waste flows.

3.2.3.4 Hypotheses and experimental data

The model required tracking 39 different elements, although data were not available for all of them. We classified them into categories with similar behaviour on the basis of thermodynamic data bases or by analogy (**Table XXX**).

Table XXX. Distribution coefficients used to model the reference process configuration; [AlF3]=15 mol%.

	D_{mol} Extraction	D_{mol} Decontamination
An	400	180
Sm	0.14	57
Zr, In	400	180
Y, La, Ce, Pr, Nd, Pm, Gd, Tb, Dy	0.31	17
Sr, Ba, Eu	0	0

The transfer functions used to model the process (**Table XXXI**) were not all equally reliable, depending on whether they were based on:

- recent and specific experimental measurements, indicated ①,
- data from older and/or less documented studies, indicated ②,
- values extrapolated from experiments carried out for other purposes than obtaining data on the process step, indicated ③,
- thermodynamic considerations or analogous behaviour, indicated ④.

Table XXXI. Degree of reliability of process modelling data

Elementary operation	Elements involved	Source reliability
Head-end operations	I, Xe, Br, Kr	④
Distillation in reducing medium	Cs, Rb, Te As, Se, Mo, Tc, Cd	① ②-③
Fluorination	Sn Zr eliminated by a process variant	④
Digestion	Mo, Ru, Rh, Pd, Ag, Sb Nb	② ④
Zn distillation		④
Salt/metal extraction	Pu, Am, Ce, Sm, In, Eu U, Np, Cm, Zr, La, Pr, Gd, Tb, Dy Nd	① ④ ②
Salt decontamination by Al/Bi	Pu, Am, Ce	①
Actinide stripping	Pu, Am	①
Oxide precipitation	Pu, Am	①

3.2.3.5 Conclusions of process analysis

The analysis yielded the following general results:

- The LiF/AlF_3 salt composition range ([15 mol% <AlF_3 <35 mol%]) meets the performance objectives: 99.9% of the actinides are extracted with less than 5% of the initial negative reactivity of the FP with fewer than three theoretical extraction stages.
- The $LiF\text{-}AlF_3$ salt is suitable for open or closed loop management in which a fraction of the flow is drawn off with or without a decontamination step.
  - Open-loop management of the $LiF\text{-}AlF_3$ salt makes FP decontamination easier, but generates a highly penalizing waste flow.
  - Closed-loop salt management is preferable in terms of waste production, but the resulting higher FP concentration in the salt makes decontamination of the actinides more difficult.
  - Providing an additional step for decontamination of the FP by means of an Al/Bi metal phase limits the increase of the FP concentration in the salt loop without any drawdown exceeding the value necessary to readjust the aluminium content. This minimizes waste salt flow without penalizing the elimination of FP from the actinides However, this generates an additional metallic waste flow that must be taken into account.

➢ Future developments

- It would be advisable to obtain a better assessment of the acceptable loading limits for various salt compositions and for the metal to better evaluate the minimum flows in the facility and to estimate the useful range of the metal/salt flow ratio.
- More information is required concerning the oxidizing stripping step.

- In the LiCl/KCl salt loop, precipitating the oxides by carbonates requires an incompressible salt drawdown flow that creates an additional chloride wasteform that must be minimized. A gaseous precipitation reactant (e.g. O_2) should be considered for this purpose [97,98].

3.2.3.6 Configuration used to estimate the flows for the system study

To avoid multiple calculations and obtain easily interpretable results we selected three process configurations with emphasis on the tolerance of the salt composition for high loading and on minimizing the primary waste mass flow. We chose a basic mixture ($[AlF_{3mol}] = 15\%$) and a conservative permissible salt loading of 15 wt%. To minimize the FP extraction and allow higher FP loading in the salt (and thus to minimize the need for salt drawdown) we diminished the M/S ratio to a maximum salt loading of 20 wt% in the metal.

Configuration A: closed-loop salt management without decontamination, with a low M/S ratio to limit FP extraction by the metal.

Configuration B: same as above but assuming the zirconium fluoride is eliminated prior to extraction and vitrified; the absence of Zr allows a lower salt drawdown and limits the waste salt flow.

Configuration C: closed-loop salt management with salt decontamination by Al/Bi.

3.2.3.7 Estimated mass flows

3.2.3.7.1 Scenario effects

The main process mass flows and waste flows were evaluated separately for each oxide fuel cycle scenario and for each of the three process configuration options described in paragraph 3.2.3.6. It is interesting to note that the results are generally equivalent from one scenario to another if they are normalized not with respect to TWhe but to the separated radionuclide flow, which in fact measures the actual "service" provided by reprocessing. This means that one scenario can be analyzed and the conclusions generalized to the others. In the following discussion the data refer to the "double strata" scenario.

Table XXXII. Waste flows (kg/TWhe) and dimensions of salt and metal loops (double strata scenario).

Process configuration	A	B	C
LiF/AlF_3 salt	2.5E+03	8.6E+02	3.0E+02
Salt loop mass	2.8E+03	3.0E+03	3.0E+03
Final waste: glass	1.3E+04	4.3E+03	1.5E+03
LiCl/KCl salt	6.0E+02	5.7E+02	6.0E+02
Salt loop mass	2.7E+03	2.6E+03	2.7E+03
Al/Cu metal flow to waste	2.5E+02	2.4E+02	2.5E+02
Al/Cu metal loop mass	1.2E+03	1.1E+03	1.1E+03
Ni/Cu metal flow to waste	1.8E+02	1.8E+02	1.8E+02
Al/Bi metal flow to waste	0.0E+00	0.0E+00	1.6E+02

3.2.3.7.2 Type and magnitude of waste flows

We identified eight primary waste flows that can be classified into three categories: the first (structural elements, hulls, and fission gases) are virtually independent of the process; the second (glass containing volatile fission products, Ni/Cu metal, Al/Cu metal, and LiCl/KCl salt flows) are proportional to the flow of radionuclides through the process. The third category includes the LiF/AlF_3 salt drawdown (which then becomes part of the glass flow) and the Al/Bi metal flow used to decontaminate the salt after the extraction step. These two flows are highly dependent on the process configuration. In configuration C the waste salt flow is reduced by roughly a factor of eight from 2500 to 300 kg/TWhe, but this results in a metal flow estimated at 160 kg/TWhe. Although this results in the production of a new wasteform for which a disposition route must be examined, the gain is still significant. The fluoride salt has the advantage of being compatible with glass up to about 20% loading; based on this hypothesis the glass production for configuration C would be 1500 kg/TWhe, or about twice the quantity generated by a hydrometallurgical process.

It would be interesting to consider the disposition of all these primary wasteforms, and especially to examine whether the metal flows could not be subject to integral group management.

3.2.3.7.3 Waste characteristics

If we disregard the gas activity, which is mainly attributable to short-lived isotopes of iodine and xenon, the $\beta\gamma$ activity is distributed mainly between the glass and the Ni/Cu and Al/Bi metal flows. The finished products (AnO_2) contain over 98% of the α activity, with the remaining α activity in the Al/Cu drawdown flow.

Over 70% of the residual power at the moment of reprocessing is due to the actinides, and is thus found in the finished products; the remaining 30% is due to the FP and is distributed about equally among the three waste flows: glass, Ni/Cu and Al/Bi. After 30 years, the FP account for only 2% of the total residual power, which is concentrated in the actinides.

The estimated characteristics in **Table XXXIII** are expressed per unit mass of primary waste. After 300 years the α activity of the glass is less than 3.7×10^6 Bq per metric ton.

Table XXXIII. Double strata scenario, configuration C: specific waste characteristics

Waste	*t* (years)	Glass	Ni/Cu	Al/Bi	Al/Cu	LiCl/KCl	AnO_2
Specific α activity (Bq/kg)	2	4.72E+08	0.00E+00	5.92E+12	5.07E+13	6.82E+11	3.71E+15
	300	3.55E+06	0.00E+00	4.45E+10	3.81E+11	5.13E+09	2.79E+13
Specific $\beta\gamma$ activity (Bq/kg)	2	3.22E+14	5.78E+15	5.80E+15	1.33E+13	1.79E+11	9.74E+14
	300	1.34E+10	1.92E+08	1.59E+11	4.16E+10	5.59E+08	3.04E+12
Radiotoxicity inventory (Sv/kg)	2	1.29E+06	7.77E+06	1.02E+07	1.80E+06	2.42E+04	1.31E+08
	300	1.70E+02	2.79E-02	9.77E+03	8.35E+04	1.12E+03	6.11E+06
Specific residual power (W/kg)	2	3.69E+01	5.13E+02	7.82E+02	5.15E+01	6.93E-01	3.77E+03
	30	3.77E-01	1.42E-03	4.98E-01	4.20E+00	5.65E-02	3.07E+02

3.2.3.8 Industrial implementation

3.2.3.8.1 Maturity of process steps

The process includes thirteen main steps. The industrial maturity of each step can be roughly estimated on the following scale: ① implemented industrially under radioactive conditions, ② implemented at pilot scale under radioactive conditions, ③ implemented at laboratory scale under radioactive conditions, ④ implemented industrially under inactive conditions, ⑤ implemented at laboratory scale under inactive conditions, ⑥ untested.

The results are indicated in **Table XXXIV**.

Table XXXIV. Estimated industrial maturity of process steps

Elementary operation	Remarks	Rating
Head-end operations	Radioactive fuel assemblies have been dismantled at industrial scale (e.g. Phenix FNR subassemblies at Marcoule)	1
Decladding/milling	Active tests at laboratory and pilot scale; recovery yields can be low, however (95%). Improving the efficiency would require a major technology R&D effort and/or an additional recovery step [99].	3
Distillation in reducing medium	Inactive tests have been carried out at laboratory scale by the CEA.	5
Fluorination	Inactive tests have been carried out at laboratory scale by the CEA. Fluorination of PuO_2 is used at industrial scale to prepare Pu metal.	1 to 5
Digestion	Inactive tests have been carried out at laboratory scale by the CEA [95].	5
Zn distillation	Volatilization/condensation of Zn is implemented in some Zn preparation processes [100].	4
Salt/metal extraction	Tested in active conditions under the PYROREP contract.	3
Salt decontamination by Al/Bi	Tested in active conditions under the PYROREP contract.	3
Actinide stripping	Conclusive exploratory tests under active conditions, but this step must still be optimized.	3
Oxide precipitation	Successfully used at laboratory scale in active conditions, but this step must still be optimized [101].	3
Filtration or centrifugation	Routinely used in the aluminium industry (Al_2O_3 or SiC filters); no example of centrifugation of molten salts.	4
Vacuum distillation of a chloride salt	Implemented in active conditions at pilot scale at ORNL West.	2
Vitrification	Implemented at industrial scale in active conditions at Marcoule, La Hague and Sellafield.	1
Overall assessment	Sum of ratings for each step	38–42

3.2.3.9 Size of process facilities

Assuming a single reprocessing facility is used for all the reactors supporting pyrochemical reprocessing (**Table XXXIV**), the daily reprocessing capacity (based on

200 days/year) would be about 2000 kg/d for the homogeneous recycling scenario, 70 kg/d for the double component scenario and 25 kg/d for the double strata scenario.

If it is assumed that reprocessing units are installed on reactor sites generating 20 TWhe, this would require about 20 plants with a capacity of about 100 kg/d for the homogeneous recycling scenario, three 25 kg/d plants for the double component scenario and a single 25 kg/d plant for the double strata scenario.

We considered that the flows in the salt (LiF/AlF_3 & LiCl/KCl) and metal (Al/Cu) loops and the number of elementary steps could be indicative of a general trend (**Table XXXII**).

This analysis showed that for a given scenario there is no significant difference between the flows involved in the three process configurations (see paragraph 3.2.3.6). However, prior zirconium volatilization and/or salt decontamination by Al/Bi imply additional steps that would increase the complexity of the facility.

3.2.3.10 Conclusion

A major R & D effort would be necessary to achieve a process suitable for industrial implementation. Current knowledge of the process core chemistry is not sufficient, the upstream and downstream steps must be examined in detail, and primary waste management must be investigated. Nevertheless, the results obtained to date are encouraging and suggest that no major obstacles will be encountered regarding process chemistry.

Conversely, the technological implementation could be a stumbling block in some areas. Obtaining a 99.9% recovery yield for decladding and milling may not be a realistic objective, although this process front-end step is highly dependent on the type fuel being reprocessed, and it would be premature to devote too many resources to this issue until the fuel specification is better defined. The core process—salt/metal extraction—is relatively independent of the nature and type of fuel reprocessed. The design of the salt/metal contactors for continuous operation is thus a key issue for demonstrating the feasibility of the industrial process and should be the primary focus of the technological R & D effort.

3.2.4 Electrorefining process in LiCl/KCl salt

3.2.4.1 Pyroprocessing flow-sheet definition

- General features

The pyrometallurgical process, mainly with electrorefining of metal and molten salt-liquid metal extraction, has been developed to apply for nuclear fuel reprocessing, for separation of the actinides from the fission products present in spent fuel.

As a part of the process, a pyrochemical reduction of spent oxide fuel to metal is being developed to introduce it into the electrorefiner. The technology employs lithium (Li) metal as a reductant and lithium chloride (LiCl) as a solvent.

The main features of the pyrometallurgical partitioning process are the following.

1) Chopped spent oxide fuel is contacted with molten LiCl at 650°C
2) Actinide oxides are reduced to metals by addition of Li metal
3) Reduced metals are washed with fresh LiCl to remove Li_2O, separated and then introduced into the electrorefining step of pyrometallurgical reprocessing

4) Li metal is recovered from the LiCl bath used in the reduction step by electrowinning at 650°C and Li/LiCl recovered are recycled to the reduction step 2).

5) Metals are electrorefined at 500°C in presence of molten chloride salts (LiCl and KCl) and of molten Cd, in order to separate selectively U from TRU (Pu, Am, Np, Cm).

6) Cd is recovered and recycled to the electrorefiner by Cd distillation at 750°C. TRU and U (traces) are separated and extracted too.

7) The alkali and alkaline-earth fission products (FPs) (converted to chlorides) and RE (or rare earth FPs as oxides), contained in the molten chloride salts, coming from the salt recovery step 4), are finally adsorbed on a suitable conditioning material (such as zeolite, sodalite).

Several problems remain at this time, notably concerning the reduction kinetics: the process time is still too long, but could be shortened by increasing the specific surface area (by milling spent fuel as a powder), by the use of high-speed contactors, or by the use of new materials.

➢ Detailed analysis of the reduction step

In the reduction step, Li dissolves in LiCl up to its solubility limit. The dissolved Li reduces actinide oxides by the following reaction:

$$AnO_2 + 4Li \rightarrow An(metal) + 2Li_2O$$

The Li_2O generated by the reduction is removed by dissolving in LiCl. This enhances the reaction. The reacted Li is made up by dissolution of floating Li, which has not reacted or dissolved. In the reduction step, alkali and alkaline-earth fission products (FPs) would be converted to chlorides, whereas rare earth FPs would remain as oxides including complex oxides, oxychlorides, etc. Eu and Sm may form divalent chlorides.

The Li reduction technology has significant advantages over other technologies which employ other reductants, such as calcium or magnesium, because:

- it does not require a ceramic melter,
- it is compatible with a lower temperature process,
- recycle of the reductant would be simpler than in the other processes.

The main parameters to study and evaluate for the reduction process are the following:

- the solubility of Li_2O in LiCl,
- the reduction behaviour of granular UO_2,
- whether complete reduction of PuO_2 by lithium is achievable,
- the upper limit of Li_2O concentration in LiCl, below which PuO_2 can be reduced to metal by Li,
- the behaviour of Americium contained in PuO_2.

➢ Detailed analysis of the electrorefining step

Industrial processes similar to nuclear spent fuel pyroprocessing, which is an electro-refining method used to separate the actinides from the fission products present in spent fuel are well known in the mining industry: an impure metal present at the anode is purified by means of an electrorefining process to a cathode, where the same metal can be

collected as pure material. Although the pyrometallurgical partitioning process was developed for metal alloy fuels, the method is also applicable to mixed oxide fuels as much as the possibility of reducing the oxides to metals has already been demonstrated.

Fuel with high Pu content is not a problem for pyroprocessing: the plutonium is dissolved and deposited continuously, but the Pu chloride concentration in the salt bath is controlled by the electrorefining process and cannot exceed the imposed concentration limits.

In the spent nuclear fuel pyroprocessing, during electrorefining, the impure actinides present in the anode spent fuel are successively electrotransported and collected on two different cathodes: a solid cathode collecting pure uranium (first step: **Figure 75**), and a liquid cadmium cathode collecting uranium, plutonium and minor actinides, together with some rare earth elements (second step).

The cathode deposits are recovered and purified by melting; the volatile materials and the cadmium are recovered by vaporisation. The metals obtained by cathode processing are free of impurities. The following step in the IFR fuel cycle consists in blending the uranium, plutonium and minor actinides for fresh fuel fabrication; new Pu material from LWRs or dismantled nuclear weapons may be added at this stage.

The free energies of formation are the key to separating the process streams in spent fuel pyroprocessing. The elements with a low chloride stability during the pyroprocess are present as metals, and remain in the anode basket or in the electrorefiner where they can be recovered by filtration. The elements with a high free energy of formation include alkali metals, alkaline-earth metals and rare earths, and halogens such as iodine. They remain stable and are dissolved in the molten salt matrix. Between these groups are the elements that can be electrotransported: only uranium can be collected on the solid cathode, while the other actinides are collected by the liquid cathode; this behaviour is due to the formation of an intermetallic (plutonium-cadmium) compound with a lower stability than Pu chloride.

Since the uranium forms no intermetallic compounds with Cd, this behaviour is used to separate uranium from the actinides and rare earths.

The fission product and actinide concentrations increase in the molten salt electrolyte after processing many batches of spent fuel, and the thermal power accumulation in the electrorefiner becomes unacceptable. Under these conditions the electrolyte must be discharged and processed as follows:

The salt from the electrorefiner is submitted to zeolite ion exchange to extract the fission product chlorides; the zeolite is then mixed with salt-free zeolite and glass before densification by hot pressing to produce a dense, stable ceramic wasteform with a FP loading of about 5 wt%.

The process parameters to study and evaluate during electrorefining, in order to define the total process time, are the following:

- the maximum allowable current density ($A \cdot m^{-2}$)
- U transport to the solid cathode
- Pu deposition on the liquid cadmium cathode

➢ Solid waste management analysis

Moreover, the pyroprocess produces zeolite-based ceramic wastes from the molten salt purification and recycling steps; these wastes do not contain significant quantities of actinides. The fission product concentration and thermal power are lower than for PUREX waste glass.

Although the *zeolite* ion exchange process allows recycling of the molten salt to the electrorefiner, it is nevertheless considered as an output waste difficult to handle because of its high water solubility.

Sodalite is a naturally occurring mineral that stably contains halide salts in its cage structure and can be synthesised at 700°C (see below):

$$6NaOH + 3Al_2O_3 + 2NaCl + 6SiO_2 \rightarrow Na_8\{(AlO_2)_6(SiO_2)_6\}Cl_2 + 3H_2O$$

The leaching resistance of sodalite at high temperature seems to be quite good, better than for zeolite

- Case 1: Zeolite

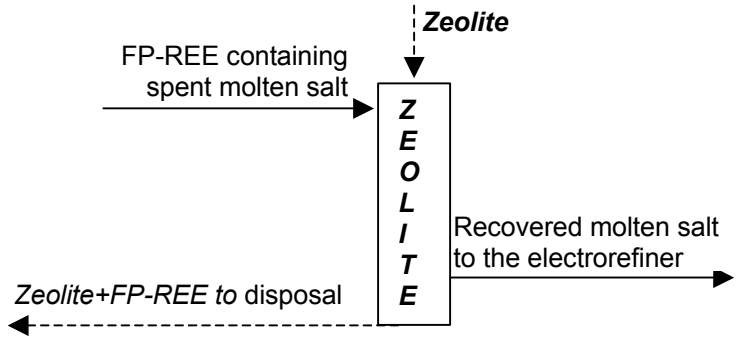

FP+REE adsorbed on zeolite are about 5 wt% together with about 15 wt% of waste salt.

- Case 2: Sodalite

$$2[\text{Waste molten salt+FP+RE}]Cl + 6\ NaAlO_2 + 6\ SiO_2 \rightarrow \textbf{Sodalite}\ \text{(for disposal)}$$

A small amount of heavy metals (about 0.1%) is lost in the fission products during the treatment.

3.2.4.2 Global process performance assessment

To evaluate the feasibility of the pyrometallurgical process applied to oxide based fuels the investigation must focus on the problems of estimating the separation factors and recovery yields in relation to the fuel composition, the liquid salt/liquid metal distribution and other parameters. The principal results include the following.

1) The weight ratio of U and TRU elements separated at the solid and liquid cathodes has to be considered dependent on the initial spent fuel compositions [102] (i.e. burnup).
2) Both the solid and liquid cathode collect a negligible quantity of REE, which remain in the molten salt bulk [103].
3) The Pu and MA elements separated by the electrorefining process comprise more than 99.9% of the total TRU.

Note : The electrolytic step alone cannot provide sufficient TRU/FP decontamination performance. The required separation is obtained by combining two elementary steps: (i) lithium reduction and electrolysis in the case of oxide fuel processing, or (ii) electrowinning and Cd+Li reductive extraction in the case of metal fuel processing.

This 99.9% yield is the overall efficiency resulting both from the electrorefining operation (90-95% efficiency) and the TRU extraction step prior to decontamination of the fission products from the salt using zeolite. The TRU extraction step is based on the distribution of a metal (typically Pu) between the cadmium phase (in metallic form) and LiKCl (in chloride form). The differences in the separation factors for the REE and TRU are considerable (e.g. 1.88 for Pu versus 210 for Gd), so that strong separation of the TRU and RE is possible. However, the separation factors for Pu, U and the minor actinides are very similar, making this method impracticable for separating these elements.

In the first phase, Cd + 1% Li can be used to extract 95-99% of the minor actinides; the remainder can be separated by countercurrent extraction of Cd-U/molten salt to reach. the overall 99.9% efficiency [104,105]. This is a very important point that warrants experimental verification.

The following points have been verified.

- The molten salt based wastes are capable of accumulating significant quantities of Pu and TRU, limited by the heat emission. This implies several batches, depending on the FP content. The molten salt is purified.
- Purification is performed with a double extraction/reduction treatment with a molten Cd-Li mixture. The TRU content in the residual salt may fall to an order of magnitude very low the initial value. It is then thought that the quantity fixed within the final ceramic wastes should be very small.

The TRU and REE content in the saline wastes before purification must be better evaluated, as well as the probable equilibrium with respect to the cathode.

A theoretical continuous material balance flowsheet is shown below for oxide (**Figure 75**) and metal (**Figure 76**) spent fuels for the “Double Component” scenario. The data are given for 6.2 electrical terawatt-hour (TWhe).

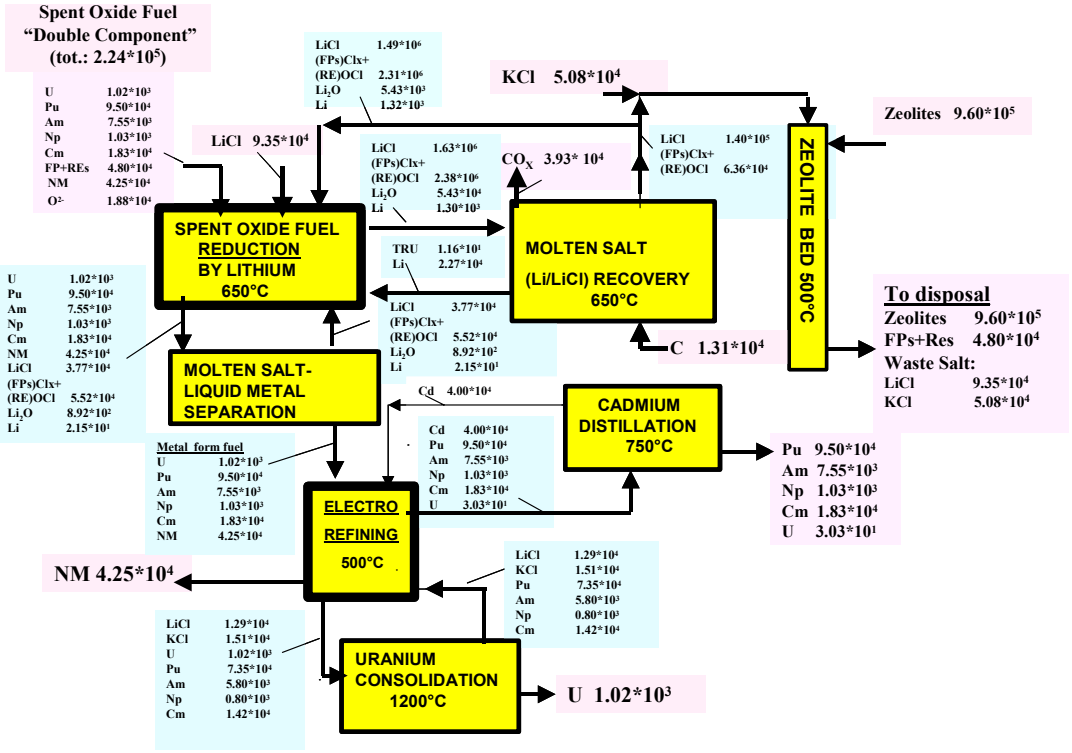

Figure 75. Material balance flowsheet of spent oxide fuel pyroprocessing (normalized to 1 TWhe; all masses are in grams)

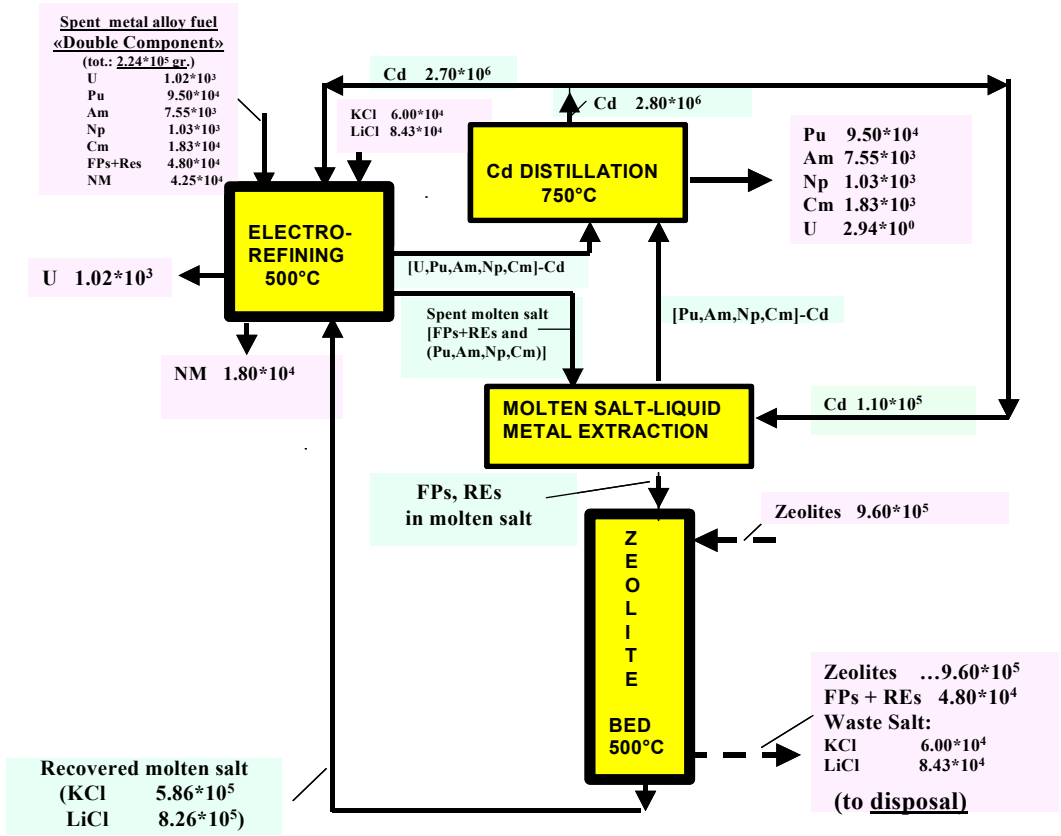

Figure 76. Material balance flowsheet of spent metal fuel pyroprocessing (for 6.2TWhe; all masses are in grams)

3.2.4.3 Preliminary technical and economic assessment

The pyrometallurgical process is designed for industrial application; increasing amounts of fission products and minor actinides are liable to accumulate in the molten salt phase as new batches are processed. The molten salt bulk composition is thus likely to be affected by the U, TRU and FP concentrations in the spent fuel and by the number of batches processed.

The limit considered for continuous processing is the accumulation of fission products in the molten salt phase until the temperature approaches a physical limit that cannot be exceeded. Most of the heat generated is attributable to the rare earth elements and minor actinides. This limit depends on the amount of fission products in the spent fuel, and therefore on the burn-up characteristics of the fuel.

Two reference throughputs for commercial pyrometallurgical plants can be assessed, considering to process the fuel either from a 400 TWhe installed reactor base (centralized processing), or from a 20 TWhe group of reactors. Hypothesis of yearly working time for the plant: 24 hours a day, 200 days a year.

Therefore the processing capacity of the facility must take into account these two different processing conditions.

Obviously, in the first case of centralized processing, spent fuel transportation is necessary, but we have to take into account that it is easier to transfer the conventional industrial technology to a large plant than to a bench scale one as the cases of 20 TWhe.

The problems due to transportation of irradiated fuel are the following:

- increasing frequency and length of shipments increase the risk of losses;
- heat release by ^{238}Pu (0.5 $W \cdot g^{-1}$) and ^{244}Cm (2.5 $W \cdot g^{-1}$) will call for increased monitoring of containers during storage and transportation.

The main technological problems to face in the pyrometallurgical process are the following:

- electrorefining processing time reduction
- materials
- process control instrumentation (as for cell current)
- safety
- materials feeding and separation systems
- process optimisation
- heat developed from FP decay
- criticality.

3.2.4.3.1 Flow balance

The reference plant throughputs are the following:

➢ "Homogeneous Recycling" scenario

- 19.04 tons/year of spent metal alloy fuel, i.e. 95.2 kg/day, for a reprocessing plant located near the nuclear reactor;

- 380.8 tons/year of spent metal alloy fuel, i.e. 1.9 ton/day, for centralized reprocessing.

➢ "Double Component" scenario:

- 687 kg/year of spent metal alloy fuel, i.e. 3.41 kg/day, for a reprocessing plant located near the nuclear reactor;
- 13.7 tons/year of spent metal alloy fuel, i.e. 68 kg/day, for centralized reprocessing.

➢ "Double Strata" scenario:

- 254 kg/year of spent metal alloy fuel, i.e. 1.27 kg/day, for a reprocessing plant located near the nuclear reactor;
- 5.08 tons/year of spent metal alloy fuel, i.e. 25.4 kg/day, for centralized reprocessing.

3.2.4.3.2 Preliminary calculations of the active part of a processing facility

The electrochemical equivalent including the faradic efficiency (65% for an average molar weight of 240 g with 3 electrons exchanged) is about 50 g/F or 5.18×10^{-4} g·C^{-1} (1F = 96 500 C).

Assuming a deposition rate of between 22 g·s^{-1} (homogeneous recycling) and 0.3 g·s^{-1} (double stratum) and assuming from laboratory experience a permissible cathode current density of 0.15 A·cm^{-2}, the total required electrode surface area of the electroseparation facility would range from 28.3 m^2 to 0.38 m^2.

These figures can be used to estimate the dimensions of the active plant in a partitioning facility. In the case of a large centralized facility comprising 18 cells electrically connected in series and supplied in parallel with metal fuel, each cell would have an electrode surface area of 1.6 m^2. This dimension would be considerably reduced in double strata scenarios, in which a single 0.75 m^3 cell with an electrode surface area of 0.38 m^2 would be sufficient.

After about 12 hours of operation, the cathode (with U) is lifted and extracted and the fresh liquid Cd cathode is added and inserted into the cell, connected to a current-carrier (-) in order to proceed to step 2 of **Figure 75**.

It is useful to provide the agitation of the molten electrolyte (i.e. by inert gas sparging). This is necessary for avoiding the concentration polarizations.

The cell height must be sufficient to accept level excursions, caused by the fresh Cd addition, which can later be extracted by a siphon.

The following materials can be chosen for industrial or commercial purposes: iron for the solid cathode and graphite for the anode basket. At present the only known alternative material that has been successfully tested is the high expensive TiB_2.

3.2.4.3.3 Waste flow assessment

Processing of the fuel from a 64.4 TWhe double component reactor population (centralized processing), according to the "Double Component" scenario.

➢ FP and RE adsorption on Zeolites

From **Figure 76** ("Double Component" flowsheet):

- Zeolites = $64.4 \times 0.96 \times 10^6$ g = 61.8×10^6 g $\rightarrow$ 61.8 tons (with 5 wt% captured FP)

  - Zeolite bulk density = 0.47 kg·dm^{-3}
  - Zeolite volume = 131 m^3
- Waste salt = 64.4 × (9.35+5.08) × 10^4 g = 9.29 × 10^6 g → 9.29 tons (corresponding to 13 wt% zeolite + waste salt mixture, as indicated in the US mass balance [106].
  - Waste salt density = 2 kg·dm^{-3}
  - Waste salt volume = 4.6 m^3
- **Total Volume = 136 m^3**

This means, for example, that about 14 adsorption columns with a 10 m^3 unit volume (2000 mm dia. × 3300 mm high) would be necessary.

Regarding disposal, we must take into account that the density of zeolites becomes at least 5 times higher, that is about 2 kg·dm^{-3}, after hot pressing and sintering. The final disposal volume is thus 31 m^3.

3.2.4.3.4 Pyrometallurgical process technology applied to conventional industrial sectors

Pyroprocesses are widely implemented in the chemical industry, mainly in metallurgical field. These industries have developed very efficient technological solutions to deal with high temperatures, corrosive reactants and sometimes toxic products. In the nuclear field there is no industrial experience, and very few pilot scale facilities have been operated. Today our efforts focus on basic data acquisition and laboratory scale experiments. These studies are only aimed at demonstrating the feasibility of pyroprocesses from a scientific point of view. This work will not provide a large amount of data about industrial implementation of these processes because laboratory scale technology is not easily transposable to industrial scale (the scale and purposes are different). However, even if industrial implementation seems far away, it must be kept in mind during this phase of the studies and we probably have much to learn from classic industry. It is likely that at least some of the pyrochemical techniques developed for non-nuclear applications could be adapted for the nuclear field.

Molten salt electrolysis, i.e. the electrolytic decomposition of a compound dissolved in an ionic melt, is a proven technology for the extraction of metals, as well as in a wide variety of industrial applications.

- Molten salt electrolysis is used extensively in the primary extraction of metals (electrowinning), including copper, magnesium, aluminium, lithium and the lanthanides.
- Molten salts are used as fluxes in casting a variety of reactive metals including aluminium and magnesium.
- Molten salts are by-products of reaction in a wide variety of processes ranging from metal purification (e.g. chlorination of light metals) to metal extraction by metallo-thermic reduction (e.g. titanium and tantalum).
- Molten salts are used as fluxes for electroslag welding of titanium and other reactive metals.
- Molten salts are important in certain embodiments of fuel cell technology, as for example in the molten carbonate fuel cell.
- Molten salts are used as fluxes in brazing aluminium and other reactive metals.

- Beyond this, molten salts have unexplored potential as media for environmentally sound new processes for metal production and for treatment of waste from the metallurgical and the chemical process industries.

➢ Conventional technologies review

Most of the primary copper in the world comes from low-grade or poor sulfide ores, which are usually treated by pyrometallurgical methods.

In the direct electrowinning of titanium metal, it is desirable to use titanium oxide as the solute and to obtain the titanium melt on the cathode.

Lead bullion produced by the blast furnace during smelting contains numerous dissolved impurities. Both pyrometallurgical and electrolytic refining are used; the latter is generally reserved for high levels of impurity.

The prime example of molten salt electrolysis can be found in the production of aluminium. Alumina (Al_2O_3) derived from mineral bauxite is dissolved in an ionic melt comprising a multicomponent solution of cryolite (Na_3AlF_6), aluminium fluoride (AlF_3), and calcium fluoride (CaF_2). The products of electrolysis are molten aluminium and carbon dioxide, the latter due to the attendant consumption of the carbon anode.

Almost all conventional molten salt electrolytic technologies use halide electrolytes and carbon anodes. There are attendant environmental consequences associated with each.

➢ Technical and economic analysis of the nuclear pyrometallurgical partitioning process

Regarding the economics of nuclear power, the choice of spent fuel management strategy has a modest but nevertheless significant impact on overall generation costs.

Considering the process simplifications and compactness, that the pyroprocessing technology seems to offer, the order of magnitude of the unit costs might be justified and considered significant as trend values.

It has been evidenced that the electrometallurgical (EM) process has not been operated at the required scale, and extensive further development is needed to achieve analogous uranium product purity targets. Moreover the advantages of decentralized compact facilities should allow the elimination of the fresh fuel transportation.

It would be misleading to enter here into a debate on the merit of costs relevant to aqueous versus pyrometallurgical processes. The emphasis should rather be placed on the ability of these processes to meet industrial requirements.

3.2.5 Application of selected pyrochemical technologies within the Molten Salt Transmutation Reactor fuel cycle

Pyrochemical and pyrometallurgical method could play important role within the fuel cycles of several transmutation systems. In addition to their application within the double strata concept and ADS fuel cycle, unsubstitutable role of pyrometallurgical methods is considered within the fuel cycle of Molten-Salt Reactors (MSR). MSRs can work under several fuel cycle options, e.g. under the $^{232}Th - ^{233}U$ fuel cycle breeders or as Pu burners and minor actinides transmuters with continuous recycling [107]. One of the main advantages of this reactor type comes out from the possibility, that this reactor type could be directly connected with the “on-line” reprocessing of circulating liquid fuel. This fuel cleaning is necessary during a long run to keep the reactor in operation. As a matter of principle, it permits to clear away typical reactor poisons like xenon, krypton, lanthanides etc. and also the products of burned plutonium and transmuted minor actinides.

The pyrochemical and pyrometallurgical separation methods could be situated both in the "Front-end" and in the "Back-end" of Molten-Salt Transmutation Reactors (MSTR) fuel cycle. There is also one fundamental difference between the "Front-end" and Back-end" of the MSTR. Whereas the "Front-end" reprocessing technology could be placed separately from the MSR site, the "Back-end" processes should be directly connected with the reactor primary fuel circuit.

However, the final part of MSTR fuel processing technology should be also placed in the reactor site and tightly attached to the "on-line" reprocessing, because the refilling of the fresh fuel into the reactor has to be carried out in connection with the removal of the burned out fuel and fission products from the primary fuel circuit.

Because the MSR/MSTR carrier fuel salt is a mixture of fluorides, the main pyrochemical-pyrometallurgical separation processes in the focus of interest should be based predominantly on fluoride separation technologies.

During the MSRE and MSBR programs, which were under way in the 1960s and 1970s in ORNL in US, some fundamental R&D work, concerning the MSR fuel clean-up was done [108,109]. Mainly two pyrochemical/pyrometallurgical separation methods were under development in ORNL. The removal of uranium from the fuel salt was based on the fluoride volatilization principles, the clean-up of the fuel salt from protactinium and rare-earth elements (lanthanides) was proposed by use of selective Molten-salt / Liquid metal reductive extraction into liquid bismuth in multistage countercurrent extraction system.

At present, the transmutation systems based on the use of MSTR represents the main P&T strategy in the Czech Republic, represented by MSTR-SPHINX project [110]. The application of some experimental results achieved within the PYROREP project are in good agreement with the work done within the Czech domestic projects.

The following conceptual flowsheet, containing pyrochemical and pyrometallurgical technologies, was proposed for MSTR fuel cycle working as the TRU burner with multiple recycling.

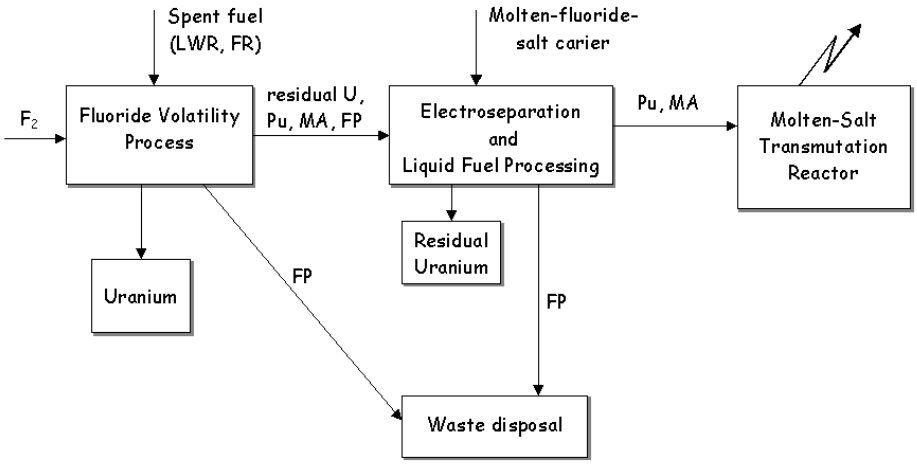

Figure 77. Conceptual flowsheet of the MSTR fuel cycle "Front-end"

The "Front-end" of the MSTR fuel cycle, shown in **Figure 77**, is based mainly on the use of "Fluoride Volatility Method" (FVM). The method, which was not the issue of R&D within the PYROREP project, can play similar role as the PUREX process. The main mission of the FVM is to remove uranium from the spent fuel and to separate plutonium

from minor actinides and fission products. The attractiveness of FVM for the use inside the MSTR fuel cycle is also based on simultaneous conversion of spent oxide fuel into the fluorides.

The main principles of FVM are based on direct fluorination of spent fuel by fluorine gas in a flame or fluidized bed fluorination reactor, where the resultant volatile fluorides (e.g. UF_6, partially NpF_6) are separated from the non-volatile ones (e.g. PuF_4, AmF_3, CmF_3, fluorides of majority of fission products), and on the subsequent purification of volatile components by using technological operations of condensation, rectification and sorption. The stream of solid fluorides outgoing the FVM can be then dissolved in fluoride carrier salt suitable for subsequent partitioning by electroseparation or molten-salt / liquid extraction processes. The fluoride volatility method was under development mainly in the US, France, the Soviet Union, Czechoslovakia and Japan. After several years of interruption, renewed work in this area has been undertaken in the Czech Republic and Japan in co-operation with Russia [111-114].

The expected FVM separation efficiencies are shown in **Table XXXV**.

Table XXXV. Theoretical FVM separation efficiency

Chemical elements	Achieved separation efficiency (%)
U	95–99.5
Pu	~98–99.5
Np	~60–70
Nb, Ru	~95–99
Am, Cm	individually inseparable (in nonvolatile fluoride stream)
FP forming solid fluorides	individually inseparable (in nonvolatile fluoride stream)

The partitioning process following the FVM should be based on similar methods and principles as the electroseparation processes within the "on-line" reprocessing of MSTR circulating fuel. The conceptual flow-sheet of "on-line" continuous reprocessing is shown in **Figure 78**.

In addition to the noble gases removal, which has to be realized inside the primary fuel circuit, actual reprocessing technology is proposed to be based on Molten salt / Liquid metal reductive extraction method and Electrochemical separation methods.

In the Molten salt / Liquid metal reductive extraction step, actinides presented in the carrier melt are removed together with fission products due to their thermodynamic properties, which do not allow their prior reduction. The processed fuel is contacted with molten metal with addition of lithium, which serves as reducing agent. All compounds except carrier melt constituents are during several extraction steps transported in reduced form into molten metal, while purified salt is next processed in fuel preparation step.

Liquid metal containing dissolved actinides and fission products is moved to the electroseparation step, where it is processed by anodic dissolution method. Liquid metal is then connected up as an anode and individual groups of elements are selectively dissolved and transported to exchangeable cathodes by step-by-step increasing potential. Fluoride melt with more advantageous thermodynamic properties (e.g. $LiF\text{-}CaF_2$) than melt used as

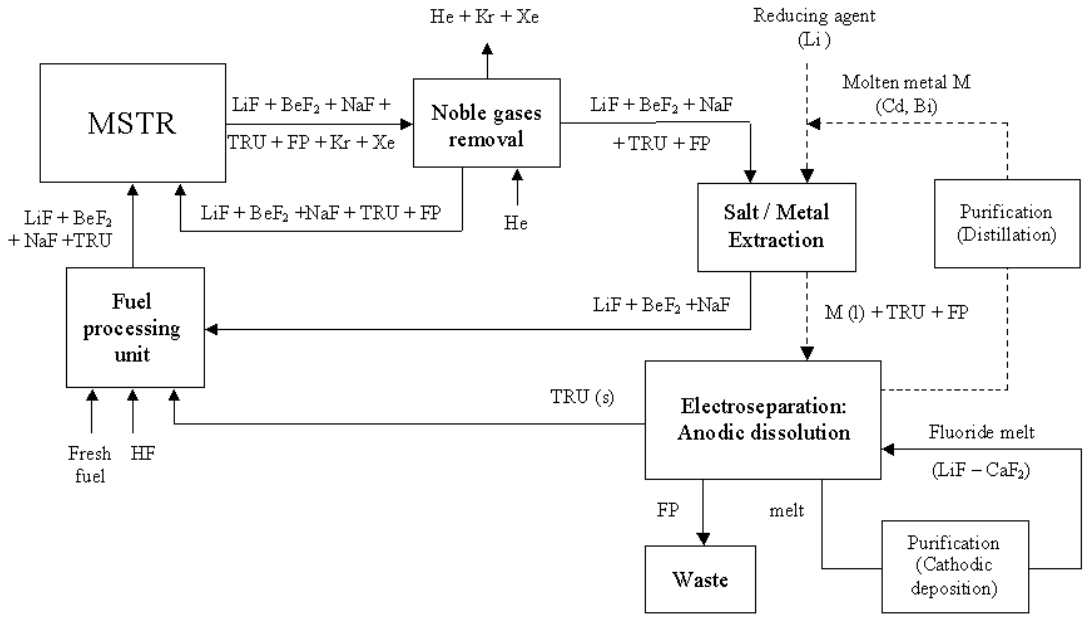

Figure 78. Conceptual flow-sheet of on-line reprocessing proposed for MSTR-SPHINX project (TRU burner without fertile material, multiple recycling)

a carrier in the reactor ($LiF\text{-}BeF_2$) is applied in this step to provide the procedure without its own decomposition. Resulting outputs are groups of elements in metallic form, which are consequently dissolved by HF and used for fuel preparation (group of actinides) or led to waste stream (group of fission products).

Purification of the carrier melt by electrochemical method dealing with cathodic deposition can be used for removal of dissolved ions, which are less stable than used carrier melt. The process resides in gradually decreasing potential of working electrode and reducing of presented ions, while the lesser the potential is, the more stable compounds are reduced.

3.3 Conclusion of general studies

- Modelling

Electrochemical cell models have been developed by ENEA to describe the electrochemical behaviour of a solid-anode solid-cathode electrorefiner in steady-state and in unsteady time-dependent conditions. Two model have been developed: the first describes constant current working condition and the second the constant cathode-potential working mode.

The models do not take stirring effects into account, so they describe only a diffusive process. The developed models correctly describe the phenomenology of the diffusive electrorefining processes. It is possible to model the behaviour of different ionic species as a function of time in different fused salt and liquid anodes. It is possible to study geometrical effects such as the device dimensions or the shape and dimensions of the electrodes. With the same technique it is possible to consider electrorefining processes with liquid cathodes. Future development could take the stirring effect into account and these codes will be validated using data coming from Pyrel device constructed by ENEA.

- System studies

System studies for a global assessment of performance and waste generation have been carried out on three different processes based on separation principle studied under this contract: reductive salt/metal extraction (CEA), electrowinning/electrolysis (ENEA), and the Molten Salt Transmutation Reactor (NRI).

None of the elementary separation steps studied will be able to recover 99.9% of the actinides with less than 5% of the total FP negative reactivity in one step. Additional steps will be necessary to achieve this objective.

Separating the actinides from the fission products through reductive extraction by aluminium in a LiF/AlF_3 medium is very promising. The LiF/AlF_3 salt composition range ([15 mol% < AlF_3 < 35 mol%]) meets the performance objectives: 99.9% of the actinides are extracted with less than 5% of the initial negative reactivity of the FP in less than three theoretical extraction stages, although this efficacy is possible only if upstream steps are implemented to eliminate some volatile alkaline FP and the noble metal FP.

Further work is necessary on the downstream process steps (aluminium stripping and recovery of actinide oxides), which have not been optimised in this conceptual system study. Special consideration will have to be given to waste management.

The analysis of electrolytic processes shows that in the case of metallic fuel electrowinning on solid and liquid cathodes can recover most of the An without entraining excessive amounts of Ln, but the recovery of the remaining An to reach 99.9% will require the implementation of two selective reductive salt/metal extraction steps using Cd+Li and Cd+U couples.

In the case of oxide fuel processing, an upstream reduction step with Li is implemented to transform the oxides to metal. This step will contribute to eliminating a significant fraction of Ln that will improve performance during the following electrolytic separation.

For these processes implementing chloride salts, the spent salt management will have to be carefully studied either to develop a suitable containment matrix or to imagine a process capable of eliminating the chloride by transforming the chloride salt stream to oxides that could be vitrified.

A conceptual global processing scheme has been proposed for a MSTR based scenario. This flowsheet implements many of the dry process principles used in fluoride media including fluoride volatility, noble gas removal, reductive salt/metal extraction, and electroseparation.

Section 3:
General conclusion and recommendations

Within the scope of the PYROREP contract, substantial progress was made by the project working teams. Many basic data values concerning the behaviour of fission products and actinides (U, Pu and Am) in molten salts and metals were measured for first time or confirmed in both fluoride and chloride media. This work will continue and will be extended notably to the acquisition of basic data first on curium and subsequently, if technically feasible, on the transcurium nuclides. These elements are not found in substantial quantities in spent fuel today, but the their presence will tend to increase appreciably as the actinides become subject to multiple recycling in MOX fuel or in double-component or double-strata burner systems.

The main R&D focus of the PYROREP contract was on the separation step, which represents the core of the future pyrochemical separation process(es). In fluoride media, the investigation of reductive salt/metal extraction yielded very promising results for both An recovery and FP decontamination yields. For electrolytic processes in chloride media it has been shown that, from the strict standpoint of actinide/lanthanide separation, an aluminium cathode would provide better results than a cadmium cathode, although the latter could be used if it is not indispensable to recover and separate the actinides from the lanthanides with very high efficiency. Conversely, recovering the separated actinides from an aluminium cathode appears to be more difficult than for a liquid cadmium cathode which can easily be evaporated. Development work should be carried out on the use of an aluminium cathode to take advantage of these potentially interesting results.

The data acquired to date are sufficient to begin designing and quantifying preliminary schemes for reprocessing processes. From the standpoint of a fuel cycle policy based on Partitioning and Transmutation (P&T), effective implementation will require not only a very high actinide recovery factor (typically 99.9%) but also sufficient FP decontamination to recycle less than 5% of the initial negative reactivity of the FP with the actinides. This criterion should also confirmed and/or qualified by taking into account not only the neutronic criterion but also the FP content recycled in the burner system and the risk of creating a holdup loop for some FP in the cycle. The system studies clearly show that the required performance cannot be obtained by a single separation stage. In each case at least two and perhaps three separation stages based on different separation principles must be implemented (electrorefining plus reductive salt/metal extraction in one case, or volatilization of some FP in a reducing medium followed by digestion of noble metals by a metal phase and reductive extraction in the second case). It is still necessary to demonstrate experimentally by combining all these process steps that the announced performance can be achieved.

An/FP separation, which constitutes the core of the process, will probably be applied to a variety of different fuels (oxide, metal, nitride, carbide, or molten fluoride) and should therefore logically be the primary focus of attention. However, An/FP separation must be preceded and followed by equally important steps designed to dissolve the elements in the molten salt upstream, and to recover the finished products downstream. These steps depend to a greater extent on the nature and type of the fuel, and must be investigated in greater detail in the future when the fuel specifications will be better defined.

Pyrochemical processes generate metal and salt waste flows of a substantially different nature than the waste currently produced by aqueous processes. A major effort will be necessary in the future to optimize the management routes for this waste—particularly for chlorinated salt waste, which is incompatible with the glass matrices used today—either by dechlorination or by developing dedicated containment matrices such as sodalites.

Unlike enhanced aqueous reprocessing processes that can be implemented with technology comparable to that used in today's reprocessing plants, the deployment of pyrochemical processes would require considerable technological R&D that must be undertaken as soon as the fuel specification for the future systems is sufficiently defined. Today the effort could focus on developing the continuous salt/metal contactors that will be necessary regardless of the type of fuel and the separation technique finally adopted.

It is also clear that pyrochemistry R&D efforts should be better coordinated in each European country to make the best use of the available human and material resources. The PYROREP contract has made an initial contribution toward this objective by pooling the research teams and creating a community of researchers who—even if their strategic objectives differ—have acquired together and now share a common wealth of knowledge in this area. From this standpoint it will be essential in the future to facilitate and encourage contacts and exchanges between teams of researchers. Independently of the very large quantity of scientific results obtained during the three-year work program, an important additional benefit of this contract has been for different research groups to interact and exchange their experience. The project has been a vehicle for interaction among the persons involved and has led to increased knowledge and skills in handling molten salts and radioactive materials.

We hope that this fruitful collaboration will continue and be further developed under the next EUROPART 6th framework project.

Section 4: References

1. Ferris, L.M., Mailen, J.C. *et al*., *J. Inorg. Nucl. Chem*., **33**, 1325 (1971)
2. Moriyama, H. *et al*., *J. Nucl. Sci. Tech.*, **21(12)**, 949 (1984)
3. Lemort, F., thèse de doctorat de l'INP Grenoble (France), soutenue le 27 janvier 1997
4. Rault, L. *et al*., *Nucl. Tech.*, **139**, 167 (2002)
5. Zachariasen, W.H., *Acta. Cryst*., **1**, 265 (1948)
6. Knacke, O., Kubaschewski, O. and Hesselman, K., *Thermodynamical Properties of Inorganic Substances, 2nd ed.*, Springer-verlag, Berlin, (1991)
7. Ruzinov, L.P., Guljanickij, B.S., *Ravnovesnye prevrasoenija metallurgiceskin reaktseij*, Moskva, 416, (1975)
8. Barin, I., *Thermodynamical Data of Pure Substances*, VCH Verlag Gesellschaft, Weinheim, (1993)
9. Barin, I., *Thermodynamical Data of Pure Substances*, VCH Verlag Gesellschaft, Weinheim, (1989)
10. Dewing, E.W., *J. Electrochem. Soc*, **123(9)**, 1289 (1976)
11. Dewing, E.W., Met. Trans. B, **21B**, 861 (1990)
12. Lebedev, V.A., *"Selectivity of liquid metal electrodes in molten halides" (title translated)*, ISBN 5-229-00962-4, (1993), (in Russian)
13. Janz, G.J., Allen, C.B., Downey, J.R. Jr., and Tomkins, R.P.T., *Physical Properties Data Compilations Relevant to Energy Storage. I. Molten Salts: Eutectic Data*, Nat. Stand. Ref. Data Ser., Nat. Bur. Stand. (US), 61, Part I, (1978)
14. Bronstein, H.R. and Manning, D.L., "Lanthanum Trifluoride as a Membrane in a Reference Electrode for Use in Certain Molten Fluorides", *J. Electrochem. Soc*.: Electrochemical Science and Technology, Vol. 119, No. 2, 125 – 128, February 1972
15. Shiguan, C., Xiaoyong, Y., Zhogxing, Yu., Qingtao, Lu., *Rare Metals* 13 (1994), 46, 1994
16. Stefanidaki, E., Hasiotis, C., Kontoyannis, C., *Electrochimica Acta* 46 (2001), 2665 – 2670, 2001
17. Clayton, F.R., Mamantov, G., Manning, D.L., "Electrochemical Studies of Uranium and Thorium in Molten LiF-NaF-KF at 500°C", *J. Electrochem. Soc* 121, 1, 86 – 90, January 1974
    Davis, J.H., Ewart, F.T., *J. Nuclear Materials*, 41, 143-145, 1971
18. Davis, J.H., Ewart, F.T., *J. Nuclear Materials*, 41, 143-145, 1971
19. Novozhilov, A.L., Devyatkin, V.N. and Pchlina, E.I., *Russ. J. Phys. Chem*., 48, 31, 1974.
20. Minh, N.Q. and Welch, B.J., *Aust. J. Chem*., 28, 965. 1975.
21. Barin, I., Knacke, O., *Thermochemical Properties of Inorganic Substances*, Springer-Verlag, Berlin 1973, supplement 1977.
22. Seon, F., Doctoral Thesis Paris, 1981
23. Scheming-King, J., Doctoral Thesis, Paris, 1994
24. Forsyth, R., SKB Technical Report 95-23, 1995
25. Castrillejo, Y., Bermejo, M.R., Pardo, R. and Martínez, A.M., *J. Electroanal. Chem*. 522, 124,2002.
26. Castrillejo, Y., Bermejo, M.R., Barrado, E., Martínez, A.M. and Díaz Arocas, P., *J. Electroanal. Chem*. 545, 141 2003
27. Bermejo M.R. Doctoral Thesis, Valladolid, 2003.
28. Y. Castrillejo, MR Bermejo, AM Martínez and P. Díaz Arocas *J.of Mining and Metallurgy* **39** (1-2) B 109-135, 2003

29. Bard, A.J. and Faulkner, L.R., *Electrochemical Methods: Fundamentals and Applications*, J. Wiley and Sons., New York (1980).
30. Galus, Z., *Fundamental of Electrochemical Analysis,* second (revised) edition, Ellis Horwood Chichester and Polish Scientific Publishers, PWN, Warsaw, 1994.
31. Noel, M., Vasu, K.I., *Cyclic voltammetry and the frontiers of electrochemistry*, Oxford &IBH Publishing Co. Pvt. Ltd. New Delhi, 1990
32. Scharifker, B. and Hills, G., *Electrochim. Acta* **28** (1983) 879.
33. Castrillejo, Y., Martínez, A.M., Vega, M., Barrado, E. and Picard, G., *J. Electroanal. Chem*., **397** (1995) 139.
34. Mohamedi, M., Doctoral Thesis Grenoble 1995.
35. Kurata, M., Sakamura, Y., Matsui, T., *J. Alloys Comp*. **234** (1996) 83-92
36. Iizuka, M., Inoue, T., Shirai, O., Iwai, T. and Arai, Y., *J. Nucl. Mater.* **297** (2001) 43-51
37. Shirai, O., Iizuka, M., Iwai, T., Suzuki, Y. and Arai, Y., *J. Electroanal. Chem*. **490** (2000) 31-36
38. Sakamura, Y., Inoue, T., Storvick, T.S. and Grantham, L.F., *et al*., *Proc. 26th Symp. on Molten Salt Chemistry*, Sapporo 1994
39. Lebedev, V.A., Babikov, L.G., Vavilov, S.K., Nichikov, I.F., Raspopin, S.P. and Skiba, O.V., *At. Energiya* **27(1)** (1969) 59
40. Serp, J. (ITU) private communication.
41. Roy, J.J., Grantham, L.F., Grimmet, J.J., Fusselman, S.P., Krueger, C.L., Storvick, T.S., Inoue, I, and Sakamura, Y., *J. Electrochem. Soc***. 143 (8)** 2487-2492, 1996
42. Johnson I and Yonco R. M. *Metall. Trans.* **1** (1970) 905-910
43. Picard, G.S., Mottot, Y.E. and Trémillon, B.L., *Proc. Fourth Int. Symp. on Molten Salts*, The Electrochem. Soc., **84** (2)) 585-602, 1984.
44. Konishi, H., Nishikiori, T., Nohira, T. and Ito, Y., *Electrochim. Acta*, **48** 1403-1408 (2003).
45. Taxil, P. and Mahenc, J., *J. Appl. Electrochem*., **17** 261-269 (1987).
46. Landresse, G., Duyckaerts, G.. *Anal. Chim. Acta*, 57,214, 1971.
47. Uchida, I., Nikimura, J., *et al*., *J. Electroanal. Chem*., 124, 165,1981.
48. Caligara, F., Martinot, L., Duyckaerts, G.., *Bull. Soc. Chim. Belges*, 76, 15, 211, 1967
49. Martinot, L.. *I. Nucl. Chem*., 37, 2525, 1975.
50. Carron, V., Ph.D. thesis, Grenoble 2000.
51. Flengas, S.N.. *Can. J. Chem*., 39, 773, 1961.
52. Kinoshita, K., Kurata, M., Inoue, T., *J. of Nucear Science and Technology*, **37**, 1, 75, 2000.
53. Yamana, H., Sheng, J., Kawamoto, K. and Moriyama, H., *J. Nucl. Mater*. **294** (2001) 53-58
54. Yamana, H. and Moriyama, H., *J. Alloy. Compound*. **275-277** (1998) 898-902
55. Johnson I, Anderson, K.E. and Blomsquist, R.A., *Trans ASM* **59** (1966) 352-355
56. Schweitser, D.G. and Weeks, J.R., *Trans ASM* **54** (1961) 185-200
57. Johnson, Chasanov, M.G. and Yonco, R.M., *Trans. Metall. Soc. AIME*, **233** (1965) 1408
58. Nishimura, T., Koyama, T., Iizuka, M. and Tanaka, H., "Development of an Environmentally Benign Reprocessing Technology—Pyrometallurgical Reprocessing Technology", *Prog. Nucl. Energy*, 1998, **32**(3/4), 381.
59. Sakamura, Y. *et al*., "Measurement of Standard Potentials of Actinides (U,Np,Pu,Am) in LiCl-KCl Eutectic Salt and Separation of Actinides from Rare Earths by Electrorefining", *J. Alloys Compd.*, 1998, **271-273**, 592.
60. Fusselman, S.P. *et al*., "Thermodynamic Properties for Rare Earths and Americium in Pyropartitioning Process solvents", *J. Electrochem. Soc.*, 1999, **146**(7), 2573.
61. Konings, R.J.M., Malmbeck, R. and Serp, J. "Evaluation of Thermochemical and Electrochemical Data for the Pyrochemical Process", *J. Nucl. Sci. Technol.*, 2002, Supplement 3, 906.

62. Castrillejo, Y. *et al*., "Solubilization of Rare Earth Oxides in the Eutectic LiCl-KCl Mixture at 450 C and in the Equimolar $CaCl_2$-Nacl Melt at 550 C", *Journal of Electroanalytical Chemistry*, 2003, **545**, 141.
63. Abousahl, S., van Belle, P., Ottmar, H. and Mayer, K., "Radiometric Assay Techniques for the Control of Minor Actinides in Advanced Nuclear Fuel Cycles", in *24th ESARDA Annual Meeting, Workshop on Safeguards and Nuclear Material Management,* 2002, Luxembourg.
64. Abousahl, S. *et al*., "Radiometric Analytical Methods for the Pyrochemical Partitioning Process", in *43th INMM Annual Meeting*, 2002, Orlando, Florida 23-27 June.
65. Iizuka, M. *et al*., "Behaviour of Plutonium and Americium at Liquid Cadmium Cathode in Molten LiCl-KCl Electrolyte", *J. Nucl. Mater.*, 2001, **299**, 32.
66. Shirai, O., *et al*., "Electrochemical Behaviour of Actinide Ions in LiCl-KCl Eutectic Melts", *J. Alloys Compd.*, 1998, **271-273**, 685.
67. Nicholson, R.S. and Shain, I., *Anal. Chem.*, 1964, **36**, 706
68. Delahay, P., *New Instrumental Methods in Electrochemistry*, 1954, New York: Interscience publishers.
69. Imbeaux, J.C. and Saveant, J.M. "Convolutive Potential Sweep Voltammetry", *Electroanalytical Chemistry and Interfacial Electrochemistry*, 1973, **44**, 169.
70. Goto, M. and Oldham, K.B., *Anal. Chem.*, 1973, **45**(12), 2043.
71. Martinez, A.M. *et al*., "Chemical and Electrochemical Behaviour of Chromium in Molten Chlorides", *J. Electroanal. Chem.*, 2000, **493**, 1.
72. Chamelot, P., Ph.D. thesis, 1994, Universite Paul Sabatier.
73. Koyama, T., Izuka, M., Shoji, Y., Fujita, R., Tanaka, H., Kobayashi, T. and Tokiwai, M., *J. Nucl. Sci.* and Tech., 384, 34, 1997.
74. Ackerman, J.P. and Settle, J.L., *J. Alloys and Compounds*, 77, 199, 1993.
75. Koyama, T., Johnson, T.R. and Fischer, D.F., *J. Alloys and Compounds*, 37, 189, 1992.
76. Ackerman, J.P. and Settle, J.L., "Distribution of Plutonium, Americium, and Several Rare Earth Fission Product Elements Between Liquid Cadmium and LiCl-KCl Eutectic", *J. Alloys Compd.*, 1993, **199**, 77.
77. Koyama, T. Johnson, T.R. and Fischer, D.F., "Distribution of Actinides in Molten Chloride Salt/Cadmium Metal Systems", *J. Alloys Compd.*, 1992, **189**, 37.
78. Kurata, M., Sakamura, Y., Hijikata, T. and Kinoshita, K., "Distribution Behaviour of Uranium, Neptunium, Rare-Earth Elements (Y, La, Ce, Nd, Sm, Eu, Gd) and Alkaline-Earth Metals (Sr, Ba) between Molten LiCl-KCl Eutectic Salt and Liquid Cadmium or Bismuth", *J. Nucl. Mater.*, 1995, **227**, 110.
79. Ackerman, J.P. and Settle, J.L., "Partition of lanthanum and neodymium metals and chloride salts between molten cadmium and molten LiCl-KCl", *Journal of Alloys and Compounds*, 177 (1991) 129-141
80. Lewis, M.A. and Johnson, T.R., "A study of the thermodynamic and reducing properties of Lithium in Cadmium at 773 K", *J. Electrochem. Soc*., Vol. 137, No. 5, May 1990, 1414-1418
81. Koyama, T., Matsubara, C., Sawa, T., Tanaka, H., "Waste form development for immobilization of radioactive halide salt generated from pyrometallurgical reprocessing".
82. Koyama, T., Seto, C., Yoshida, T., Kawamura, F., Tanaka, H., "Immobilization of halide salt waste from pyrochemical reprocessing by forming natural occurring mineral sodalite".
83. Barrer, Cole, Sticher, "Chemistry of soil minerals: part V", *Chem. Soc*. (A), p. 2475, (1968)
84. Bellotto, Gualtieri, Artioli, Clark, "Kinetic study of the Kaolinite-Mullite reaction sequence. Part I: Kaolinite dehydroxylation", *Physics and Chemistry of Minerals*, vol. 22, pp. 207-214 (1995).
85. Taylor, Henderson, "Infrared spectra of anhydrous members of the sodalite family", *Spectrochimica Acta*, vol. 33 A, pp. 283-290 (1977)

86. Pascal, P., *Nouveau traité de chimie minérale*, vol. III (Rubidium, Césium, Francium) p. 100, "Compléments" vol. 1, pp. 53-54.
87. Rabiller H., Compte rendu de réunion du 28/01/2002, LEBM/CR/2002-02
88. Hash, M.C., Pereira, C., *Ceramic Transactions* Vol 72, Environmental Issues and Waste Management technologies in the ceramic and Nuclear industries II, p 135-143, 1996
89. Boussier H., Compte rendu de réunion du 23/05/2003, SCPS/LPP/2003-014
90. J.O.M. Bockris, A.K.N. Reddy, *Modern Electrochemistry*, vol. I and II, Plenum Press, New York (1977).
91. Tomczuk, Z., Ackerman, J.P., Wolson, R.D., Miller, W.E., "Uranium transport to solid electrode in Pyrochemical reprocessing of Nuclear Fuel", *J. Electrochem. Soc*. 139 (1992), 3523-3528.
92. Boussier, H., Malmbeck, R., Marucci, G., "The European Pyrometallurgical Processing Research Program PYROREP: Main Issues" (to be published).
93. Koyama, T., Iizuka, M., Shoji, Y., Fujita, R., Tanaka, H., Kobayashi, T., Tokiwai, M. "An experimental study of molten salt electrorefining using solid iron cathode and liquid cadmium cathode for development of pyrometallurgical reprocessing" *J. of Nucl. Sci. & Tech*. 34 (1997), 384-393.
94. Kurata, M., Sakamura, Y., Matsui, T., "Thermodynamic quantities of actinides and rare earth elements in liquid cadmium and bismuth", *J. of Alloys and Compounds*, 234 (1966) 83-92.
95. Jouault, C., "Séparation pyrochimique d'éléments facilement réductibles contenus dans des déchets nucléaires", Thesis INPG (2000).
96. Horie, M., Miyake, C., "Study of processing HLLW by super high temperature method, *Recod'94* (1994).
97. Osipenko, A.G. *et al*., "Conversion of weapon-grade plutonium into nuclear Mox fuel by pyrochemical methods" 5th International Symposium on molten salt chemistry and technology, Dresde, Germany (1997).
98. Lacquement, J., Adnet, J.M., Brossard, P., Osipenko, A.G., Bychkov, A.V., Skiba, O.V., "Pyrochemical conversion of weapon-grade plutonium into plutonium oxide" *Atalante 2000* (2000)
99. Bond, W., Mailen, J.C., and Michaels, G.E. "Evaluation of methods for decladding LWR fuel for a pyroprocessing-based reprocessing plant" ONRL/TM-12104 (1992).
100. Lambert, A., "Étude bibliographique: Application des procédé pyrochimiques dans l'industrie classique de production des métaux" Rapport de stage Mai (2002).
101. Bermejo, R., *Adquisicion de datos basicos en cloruros fundidos de la tierras raras (La, Ce, Pr, Nd e Y) presentes en un combustible nuclear simulado (simfuel)*, Ph.D. thesis, Universidad de Valladolid (2003).
102. Koyama, T. *et al*., Int. Conf. on Nucl. Engineering, vol. 4 (1996).
103. Laidler, J.J., "Development of Pyroprocessing Technology", *Progress in Nuclear Energy*, 131 (1997).
104. Chow, L.S. *et al*., "Continuous Extraction of Molten Chloride Salts with Liquid Cadmium Alloys", *Proceedings*, Global 1993.
105. Mariani, R.D., Benedict, R.W., Simulated First Operating Campaign for the IFR Fuel Cycle Demonstration", *Proceedings*, Global 1993.
106. Ackerman, J.P. *et al*., "Treatment of Wastes in the IFR Fuel Cycle", *Progress in Nuclear Energy*, 141-154 (1997).
107. *A Technology Roadmap for Generation IV Nuclear Energy Systems*, US DOE, GIF-002-00, December 2002
108. Haubenreich, P.N., "Molten-Salt Reactor Experiments", ORNL-4396, 1970
109. Rosenthal, M.W.,*et al*., "Recent progress in molten-salt reactor development", *Atomic Energy Review*, Vol. 9, No. 3

110. Uhlir, J., Hron, M., Priman, V., Valvoda, Z., "Current status of Czech R&D program in partitioning and transmutation", OECD/NEA 7th Information Exchange Meeting on Actinide and Fission Product Partitioning & Transmutation, Jeju, Republic of Korea, October 14-16, 2002

111. Schmets, J.J., "Reprocessing of spent nuclear fuels by fluoride volatility processes", *Atomic Energy Review* (1970), Vol. 8, No. 1

112. Bourgeois, M., "Installations pour l'étude du traitement par volatilisation des fluorures des combustibles irradies", *Bulletin d'Informations Scientifiques et Techniques* 1974, 188, 7-16

113. Demjanowich, M.A. *et al*., "Fluorination of irradiated uranium-plutonium oxide fuel in flame reactor" (in Russian), RIAR report No. 50(565), Dimitrovgrad, 1982

114. Marecek, M., Novy, P. and Uhlir, J., "Technological verification of fluoride volatility method for front-end of molten salt transmutation reactor fuel cycle", *Proc. of GLOBAL 2001*, Paris, September 9-13, 2000